Site U1357[1]

Expedition 318 Scientists[2]

Chapter contents

Site summary

The primary objective at Integrated Ocean Drilling Program Site U1357 (proposed Site ADEL-01B) was to recover a continuous ~200 m Holocene sedimentary section from the Adélie Basin located on the Antarctic continental shelf off the Wilkes Land margin. The Adélie Basin is a 1000 m deep glacially scoured trough separated from the Adélie Depression (70 km eastward) by the 200 m deep Adélie Bank (Figs. F1, F2). Previous piston and kasten coring of the upper sediment column shows that sediments in the Adélie Basin are deposited as annual to near-annual layers averaging 2 cm in thickness. The thickness of the Holocene sedimentary section above the last glacial diamict (190 m; Fig. F3) is consistent with this high rate of sedimentation being maintained for the past 10,000 y.

The ultrahigh resolution Adélie Basin Holocene section will be used to attempt to produce the first annually resolved time series of oceanographic and climatic variability derived from a Southern Ocean marine sediment core. These data can be directly compared to annual ice-core records from Antarctica's coastal ice domes as well as other marine sediment cores from the Antarctic Peninsula and other parts of the East Antarctic margin. The site is sensitive to drainage winds from Antarctica as well as the polar easterly winds, sea ice extent, the Southern Annual Mode, and the position of the southern boundary of the Antarctic Polar Frontal Zone in the Indian and Pacific oceans. Little is known about past variability in these systems from marine records, and none have annual or near-annual resolution. The Adélie Basin site lies directly downwind and downcurrent from the Mertz Glacier polynya (Massom et al., 2001, 2003) and therefore collects biogenic materials produced in one of Antarctica's major coastal polynyas. The Mertz Glacier polynya and underlying Adélie Depression may produce as much as 25% of all Antarctic Bottom Water (AABW) (Rintoul, 1998; Marsland et al., 2004; Williams et al., 2008). Given the known presence of benthic foraminifers in the Adélie Basin and the substantial bottom water temperature anomaly associated with local high-salinity shelf water, Site U1357 has the potential to yield information on AABW production through time. Understanding Holocene climate variability at this East Antarctic site will aid in determining the range and characteristics of natural climate variability during a period of relatively constant atmospheric carbon dioxide levels. This record will also aid in the assessment of different forcing factors (solar, ocean-atmosphere

[1] Expedition 318 Scientists, 2011. Site U1357. *In* Escutia, C., Brinkhuis, H., Klaus, A., and the Expedition 318 Scientists, *Proc. IODP,* 318: Tokyo (Integrated Ocean Drilling Program Management International, Inc.). doi:10.2204/iodp.proc.318.105.2011
[2] Expedition 318 Scientists' addresses.

doi:10.2204/iodp.proc.318.105.2011

interaction, and volcanic) responsible for climate change over the past 10,000 y.

Sediments accumulate in the 1000 m deep Adélie Basin (Figs. F1, F2) as a thick drape overlying a high-amplitude reflector with no underlying penetration (Fig. F3). The strong reflector is interpreted as a glacial diamict from the Last Glacial Maximum. The East Antarctic Ice Sheet expanded to the shelf edge during the Last Glacial Maximum (Domack, 1982; Barnes, 1987; Eittreim et al., 1995), and the Adélie Basin was filled with ice. Ice lift-off and southward retreat from other deep shelf basins of East Antarctica occurred between 10,000 and 11,000 y ago (Siegert et al., 2008; Leventer et al., 2006). This is the expected age range of the lowermost sediments recovered from Site U1357. The seismic line shows 190 m of continuous, horizontal, parallel reflectors at the site, consistent with a drape of Holocene sediment undisturbed by sea level change or glacial erosion.

Three holes were cored at Site U1357. In Hole U1357A, Cores 318-U1357A-1H through 21X penetrated to 186.6 meters below seafloor (mbsf), recovered 183.87 m (99%) of diatomaceous ooze, and penetrated the underlying last glacial diamict. After offsetting the ship 50 m east of Hole U1357A, we cored Hole U1357B. Cores 318-U1357B-1H through 19H penetrated to 170.7 mbsf and recovered 172.44 m (101%) of sediment. Hole U1357C, offset 25 m west of Hole U1357A, produced Cores 318-U1357C-1H through 11H, penetrated to 103.8 mbsf, and recovered 110.7 m (107%) of sediment. Cores from Hole U1357A were split and described during the expedition. Cores from Holes U1357B and U1357C were preserved as whole-round sections for postcruise splitting, describing, and sampling. All cores from this site contained sediments that vigorously degassed methane and hydrogen sulfide upon decompression to 1 atmosphere (see **"Geochemistry and microbiology"**). Gas pressure caused expansion of the sediment section, which resulted in the loss of some sediment from core breaks as well as section breaks, particularly above 40 mbsf. This was minimized by drilling small holes in the core liners at regular intervals.

The sediments in Hole U1357A consist of three lithologic units (see **"Lithostratigraphy"**). The uppermost Unit I is 170 m of laminated Holocene diatom ooze. Unit I overlies a 15 m transitional unit of sand and silt-bearing diatom ooze (Unit II), which in turn sits on a hard, carbonate-cemented, and poorly sorted gravelly siltstone (Unit III, a diamict). Units I and II exhibit regular laminations defined by color (alternating dark olive-brown to light greenish brown layers) and textural variability. Individual laminations range in thickness from 1 to 3 cm and extend throughout the entire 186 m thick section lying on top of the diamict.

Based on analysis of multiple samples from core breaks and section breaks, Site U1357 sediments contain a well-preserved Holocene Southern Ocean diatom flora with varying contributions from cool open-ocean and sea ice–associated taxa (Armand et al., 2005; Crosta et al., 2005a). Radiolarians, silicoflagellates, and sponge spicules are common and well preserved. Organic-walled dinoflagellate cysts are present as well as motile dinoflagellate stages, abundant tintinnid loricae, and copepod remains.

Light and dark laminations were sampled throughout the Holocene section. Based on trends in diatom assemblage succession within paired laminations as well as previous work from the Adélie Basin region (Denis et al., 2006) and other laminated diatom sections from the east Antarctic margin (e.g., Stickley et al., 2005; Maddison et al., 2006), each light–dark lamination couplet is provisionally interpreted as a single season of biogenic production and accumulation. It is assumed that diatomaceous sediments begin to accumulate during spring sea ice retreat following the development of early season phytoplankton blooms in the Mertz Glacier polynya. Blooms persist through summer open-water conditions and conclude with the autumn regrowth of sea ice and destabilization of the water column. The unusually high accumulation rates (averaging 2 cm/y) are likely the result of syndepositional focusing processes that sweep biogenic debris from the shallow Adélie and Mertz banks into the deep shelf troughs of the Adélie Basin and Adélie Depression.

A low-diversity assemblage of calcareous planktonic (*Neogloboquadrina pachyderma* and *Globigerina bulliodes*) and benthic foraminifers (*Globocassidulina subglobosa* and *Triloculina frigida*) occurs in Site U1357 Holocene sediments. Planktonic foraminifers were observed throughout the sedimentary section, and benthic foraminifers were observed in several core-break samples that were sieved. The occurrence of well-preserved calcareous foraminifers is unusual in Antarctic shelf basins, as shelf bottom waters are highly undersaturated with respect to calcite. High sedimentation rates likely contribute to foraminifer preservation in the Adélie Basin sediments.

In addition to abundant diatoms and foraminifers, sediments in Hole U1357A contain large quantities of fish debris, including at least 44 layers of concentrated fish vertebrae. With abundant phosphatic, calcareous, opaline, and organic biogenic detritus, Site U1357 sediments offer an unusually diverse array of assemblage-based and geochemical environmental tracers for shore-based studies.

Site U1357 sediments posed a significant challenge for the analysis of physical properties (see **"Physical properties"**). The sediments are so diatomaceous

that they exhibit extremely low to negative magnetic susceptibility. Whole-round core analysis of all three holes using a Bartington loop sensor and split-core analysis using a point source magnetic susceptibility sensor in Hole U1357A did not yield useful data for hole to hole correlation. The production of millimeter-scale pockmarks from degassing of methane and hydrogen sulfide throughout the sediment column makes bulk density determination difficult using discrete sample analysis (moisture and density) or with the gamma ray attenuation (GRA) densitometer. Natural gamma ray (NGR) levels are minimal because of the low concentration of terrigenous material in lithostratigraphic Unit I. Nevertheless, with sufficient background count correction NGR track scans yielded useful data for the correlation of cores from Holes U1357B and U1357C and a portion of cores from Hole U1357A.

Additional information for attempting hole to hole correlation was provided by magnetic susceptibility determination of >1800 discrete samples that had been taken from Hole U1357A at 10 cm intervals for postcruise foraminifer analysis. Each dried sample was weighed and analyzed with the Kappabridge KLY magnetic susceptibility detector. The Kappabridge has roughly 2 orders of magnitude greater sensitivity than the whole-core loop or split-core point source sensors. The resulting data set suggests that magnetic susceptibility measurements of discrete samples might be of use in developing a robust hole to hole correlation.

Site U1357A is located close to the south magnetic pole, and we observed the expected high inclinations in the paleomagnetic signature of split-core sections (see **"Paleomagnetism"**). After processing and matching paleomagnetic declinations across core breaks, Hole U1357A yielded a paleomagnetic secular variability profile that appears to match a geomagnetic secular variation model spanning the last 7000 y (CALS7k.2 of Korte and Constable, 2005) for 66°S, 144°E. The age-depth relationship predicted by application of this model to the secular variation signal obtained from Hole U1357A is consistent with that expected for this site based on radiocarbon dating of the upper 50 m of the sediment column (Costa et al., 2007) and the overall sediment sequence thickness.

Geochemical analysis of 96 sediment samples from Hole U1357A (see **"Geochemistry and microbiology"**) yielded $CaCO_3$ contents ranging from 1 to 3 wt% for most of the hole, with one distinct carbonate-rich layer ($CaCO_3$ > 9 wt%) at 126.34 mbsf. Organic C content is uniformly high (for Antarctic shelf sediments), between 1 and 2 wt%. C/N ratios between 7 and 12 are consistent with relatively well preserved and labile marine organic matter. SiO_2 concentrations are high (76–91 wt%) and are accompanied by low concentrations of TiO_2 (<0.3 wt%) and Al_2O_3 (<5.6 wt%), as expected for a nearly pure diatom ooze with little terrigenous input. The authigenic phosphate mineral struvite ($NH_4MgPO_4{\cdot}6H_2O$), which forms through bacterial biomineralization in anoxic sediments in the presence of ammonium, was observed at several depths.

Headspace methane concentrations varied by more than an order of magnitude downcore, increasing from 5,000 to 43,000 ppm from 0 to 20 mbsf and then declining to highly variable concentrations at greater depths, mostly between 5,000 and 18,000 ppm. Significant concentrations of H_2S were detected as well, consistent with anoxic diagenesis of organic-rich sediments. An extensive microbiology program, focusing on phospholipid analyses and molecular 16S ribosomal ribonucleic acid (rRNA) sequencing, was completed in the upper 20 m of Hole U1357C. Pore water samples collected from adjacent whole-round core samples show no detectable SO_4^{2-} except in core top samples suspected of contamination with seawater. Ammonium increases almost linearly from near-surface values of 900 to 4500 µM at 18 mbsf. Total dissolved inorganic carbon and alkalinity increase to 18 mbsf as well, to values of 79.6 and 88 mM, respectively, whereas pH drops to 7.5 at 20 mbsf. These profiles are consistent with bacterially mediated diagenesis within anoxic pore waters. Methane is derived from CO_2 reduction following the removal of SO_4^{2-}. Pore waters were not analyzed deeper than 20 mbsf in the core, but samples for 16S rRNA sequencing were taken from core ends to the maximum depth of penetration in Hole U1357C (103.8 mbsf).

Operations

Transit to Site U1357

Site U1357 was the southernmost of the shelf sites, all of which are prone to ice coverage. Shortly after departing Site U1356 at 0615 h on 2 February 2010, we began to encounter floating ice. The vessel speed was frequently adjusted to match visibility and ice conditions as we proceeded on a southeast heading toward the site. We were able to negotiate through large concentrations of icebergs and growlers with the benefit of a clear and sunny day providing excellent visibility. The 218 nmi transit to Site U1357 took 25.7 h at an average speed of 8.5 kt. We were positioned over Site U1357 at 0800 h on 3 February. After a short wait to evaluate the movement of proximal ice, we began assembling the advanced piston

coring (APC)/extended core barrel (XCB) drilling assembly. All times in this section are given in local ship time, which was Universal Time Coordinated + 11 h.

Site U1357

Hole U1357A

Coring in Hole U1357A began at 1445 h on 3 February, and the first core established the seafloor depth at 1025.9 meters below rig floor (mbrf) (1014.8 meters below sea level [mbsl]). However, the extremely diffuse boundary between bottom water and seafloor sediment precludes accurate definition of water depth using a standard shipboard sonar system; most coring systems (including the APC) typically do not recover this boundary. Cores 318-U1357A-1H through 21X penetrated to 186.6 m and recovered 183.87 m (99%) (Table T1). All APC cores at this site were obtained with nonmagnetic core barrels unless otherwise noted. The last APC core (Core 318-U1357A-20H) was an incomplete stroke. We then took a single XCB core from 185.6 to 186.6 mbsf, and it bottomed out in diamict. Coring was interrupted for 4 h when an iceberg approached close to the ship. Prior to pulling out, the hole was filled with 79 bbl of 10.5 ppg mud. The bit cleared the seafloor at 1120 h on 4 February.

Hole U1357B

After offsetting the ship 50 m to the east, we started coring in Hole U1357B at 1345 h on 4 February. The seafloor was at 1028.0 mbrf (1017.0 mbsl). APC Cores 318-U1357B-1H through 19H penetrated to 170.7 mbsf and recovered 172.44 m (101%) (Table T1). Prior to pulling out, the hole was displaced with 72 bbl of 10.5 ppg mud. The bit cleared the seafloor at 0340 h on 5 February.

Hole U1357C

Hole U1357C, offset 25 m west of Hole U1357A, was started with the APC at 0645 h on 5 February. APC Cores 318-U1357C-1H through 11H penetrated to 103.8 mbsf and recovered 110.7 m (107%) (Table T1). Once again, coring had to be suspended because of the proximity of several icebergs. This time, however, the ice passed close enough that we had to abandon the hole so we could offset the ship 2.8 km to the southeast to allow the ice to pass through the drilling area. The bit cleared the seafloor at 1358 h on 5 February and we had to wait until the next morning to retrieve the beacon.

At this time, the weather deteriorated to gale force winds with gusts measured up to 58 kt, and the combined sea and swell reached 30 ft. During heavy snow squalls the visibility dropped to 0.5 nmi. To ensure the safety of the vessel, lookouts were posted to observe for growlers and icebergs as the vessel adopted a controlled drift back toward location. As the storm faded, the sea quickly flattened enough for the beacon to be recovered at 0815 h on 5 February.

The plan was to reoccupy Site U1357 to finish coring the lowermost ~80 m of the section a third time to help provide a more complete composite section and to obtain downhole logs. The weather forecast, however, predicted winds gradually increasing to 45–50 kt by the evening of 7 February, with occasional gusts in excess of 60 kt and poor visibility in heavy snow squalls. Because of the high concentration of icebergs of all sizes in the Site U1357 area, safety concerns dictated that the most prudent course of action was to depart the region. We departed Site U1357 at 0900 h on 6 February. The total time at Site U1357 was 63.4 h (2.6 days) of which 24.25 h (38% of total) were due to delays caused by ice.

Lithostratigraphy

Three holes were cored at Site U1357. In Hole U1357A, Cores 318-U1357A-1H through 21X penetrated to 186.6 mbsf, recovered 183.87 m of diatomaceous ooze, and penetrated the underlying last glacial diamict. The "official" recovery in Hole U1357A was calculated as 99%; however, expansion of the sediment section was significant as a result of gas evolution, mostly H_2S and CH_4, throughout the core. In Cores 318-U1357A-1H and 2H, tens of centimeters of sediment were lost before sections could be cut and capped. Minor amounts of additional material were lost from individual sections when several end caps blew off while cores sat on the rack in the laboratory. We reduced sediment loss by drilling holes in the core liner as soon as it arrived on the catwalk, but some material was typically lost from the ends of the core and was delivered to the micropaleontology laboratory. Several cores from Hole U1357A ruptured in the middle from gas pressure while sitting on the cutting rack on the catwalk. Sections that were disturbed by this process are identifiable by the presence of an outer liner and the shattered condition of the original liner. Care was taken to retain as complete a section as possible, but the interval from ~60 to 80 mbsf in Holes U1357A and U1357C will be examined carefully for disturbance. Cores from Hole U1357B did not rupture. The strategy of triple coring with a different starting depth for each hole will help in the production of a composite section for this site. The last APC core in Hole U1357A (Core 318-U1357A-20H) was an incomplete stroke, resulting in less than the attempted 9.5 m. We collected a single XCB core (318-U1357A-

21X) from 185.6 to 186.6 mbsf. This core bottomed out in diamict, recovering ~11 cm of highly lithified carbonate-cemented gravelly mudstone. Above the diamict, the lowermost 15 m in Hole U1357A contains increasing amounts of terrigenous debris, mostly silt, toward the base, with some sand and gravel near the base of the hole.

After offsetting the ship 50 m east of Hole U1357A, we cored Hole U1357B. Cores 318-U1357B-1H through 19H penetrated to 170.7 mbsf and recovered 172.44 m (101%) of sediment. The loss of sediment because of gas evolution and section expansion was minimized throughout this core by drilling small gas release holes at regular intervals along the core liner, as was done for Hole U1357A below Core 318-U1357A-3H. The section recovered from Hole U1357B appears to provide an intact Holocene sedimentary sequence with the small apparent excess recovery (1%) representing gas expansion. We did not attempt to core into the diamict in Hole U1357B.

Hole U1357C, offset 25 m west of Hole U1357A, produced Cores 318-U1357C-1H through 11H, penetrated to 103.8 mbsf, and recovered 110.7 m (107%) of sediment. Again the excess recovery appears to be due to gas expansion, even with gas release holes drilled into the liners of every core. A portion of Core 318-U1357C-8H ruptured on the catwalk, similar to that observed for the core at this depth from Hole U1357A. Coring operations for Hole U1357C were terminated before reaching the underlying diamict because of weather and ice conditions. Hole U1357C was not logged, again because of time and weather constraints.

All cores from Hole U1357A were split and described after running them through the Whole-Round Multisensor Logger (WRMSL). As part of the description processed, the archive half of each section was photographed using the high-resolution Section Half Imaging Logger. The archive halves were also analyzed using the color reflectance and point source magnetic susceptibility scanner on the Section Half Multisensor Logger at 1 cm intervals for Sections 318-U1357A-1H-1 through 9H-1 and at 2 cm intervals for the remainder of the hole (Sections 318-U1357A-9H-2 through 20H-CC). Normal shipboard sampling of the working halves of Hole U1357A core included small amounts of material taken for physical property measurements, carbonate and organic carbon content, and diatom analysis. The working halves of all Hole U1357A cores were sampled at 10 cm intervals for foraminifer analysis and preliminary age-dating. All other sampling was deferred until after the expedition. Foraminifer samples were taken shipboard to ensure good preservation, as dissolution of calcareous microfossils during core storage and transport is a known phenomenon in highly organic reducing sediments from the Antarctic margin. After sampling and describing, working- and archive-half cores were double wrapped, flushed twice with nitrogen gas, sealed in heat-shrink tubing with oxygen absorber packs, and curated in D-tubes in cold storage.

The sedimentology and lithostratigraphy sections of this site report are based solely upon information from Hole U1357A. Cores from Hole U1357B were not split but rather were sealed as whole-round cores in shrink wrap with oxygen absorbers after running the sections through the WRMSL. Cores 318-U1357C-1H and 2H were mostly sampled shipboard as a series of contiguous whole-round cores dedicated to microbiology, interstitial water analysis, optically stimulated luminescent age-dating, and ^{32}Si age-dating. The remainder of Hole U1357C cores were not split and were curated as for the Hole U1357B cores after running the sections through the WRMSL. Splitting, description, and sampling of these cores will occur after the expedition.

Based on visual core descriptions and smear slide analyses, Hole U1357A is divided into three lithostratigraphic units (from top to bottom): 170 m of laminated Holocene diatom ooze, a 15 m thick transitional unit of sand and silt-bearing diatom ooze, and a subglacial diamict.

Unit descriptions

Unit I

Interval: 318-U1357A-1H-1, 0 cm, through 19H-1, 115 cm
Depth: 0–170.25 mbsf
Age: Holocene, probably spanning the last 10,000 y

Unit I consists of dark olive-brown to light greenish brown diatom ooze. The entire unit exhibits centimeter-scale laminations defined by color changes between lighter greenish brown versus darker brown intervals (Fig. **F4**), which are occasionally bowed downward toward the edge of the core liner. These laminations are often not clearly visible on a freshly split core surface. In fact, most freshly split sections from cores that have not yet been exposed to air are initially a uniform dark brown color (Fig. **F5,** left panel). Initially, some laminations are visible on the basis of millimeter-scale textural features consisting of alternating "cotton candy" fibrous versus smoother surfaces or through differences in the size and shape of gas expansion microcracks along bedding surfaces. After exposure to air, faint color differentiation becomes apparent. The colors develop more fully over a period of hours. This color development upon surficial oxidation is illustrated in Figure **F5.** The figure

shows images of Section 318-U1357A-6H-4 taken after 10 min, 1 h, and 3 h of exposure of the freshly split core to air at room temperature. The general lightening of the sediment surface and emergence of laminations defined by light–dark color variability can be seen in the three panels from left to right. Laminations are visible throughout Unit I and range from <1 cm thick to as thick as 4 cm. Laminations from Section 318-U1357A-18H-7, typical of the base of Unit I, are shown in Figure F6. The time available for description and layer counting did not allow for uniform exposure times to air, so real-time counting was not done on a section by section basis.

The entire core exhibits slight to moderate disturbance related to the release of hydrogen sulfide and methane. Gas release produces small pockets and fractures (Fig. F7) that reduce the utility of the shipboard track scanning systems as well as the reliability of shipboard physical property measurements. The maximum amount of gas release appeared to occur in Core 318-U1357A-8H.

Forty-four smear slides were described from Unit I (see Site U1357 smear slides in "Core descriptions"). The diatom ooze is unusually pure, with diatom contents estimated from smear slide description as ranging from 80% to 99% and a mean of 91% (Fig. F8). Rare intervals with minor clay or fine silt grains account for up to 10%–20% of the smear slide grains. Other rare (<3%) microscopic biogenic grains observed in smear slides from Unit I include silicoflagellates, sponge spicules, radiolarians, and foraminifers. Other rare (<5%) identifiable mineral grains observed in some smear slides from Unit I include quartz, feldspar, and pyrite.

The largest particles observed in Hole U1357A were fish remains, predominantly millimeter-size vertebrae, but also fish teeth. Fish fragments are found throughout Unit I and appear well preserved (Fig. F9). Intervals of concentrated vertebrae, similar in appearance, are listed in Table T2 as a guide to the most abundant macrofossil observed at Site U1357. Fish bones generally consist of 60%–70% hydroxyapatite crystals embedded in a fibrous collagen matrix (Newesely, 1989; Schenau and De Lange, 2000). The abundance of fish vertebrae throughout the core suggests they may be used for accelerator mass spectrometry age-dating of the embedded proteinaceous carbon.

A possible bivalve shell was observed at interval 318-U1357A-3H-3, 117 cm. Rare bryozoan grains were reported at several depths. Foraminifers were visible at the split core surface throughout Unit I and include *Neogloboquadrina pachyderma*, *Globigerina bulloides*, and the benthic foraminifer *Globocassidulina subglobosa*.

Siliceous microfossils are unusually well preserved throughout Unit I. Shipboard micropaleontologists report the absence of reworked older diatoms as well as a diverse array of Holocene species. Radiolarians (Fig. F10), sponge spicules, and silicoflagellates are also well preserved. Organic-walled dinoflagellates cysts are present, as well as motile stages, tintinnid loricae, copepod remains, and pollen.

A translucent 1 mm thick tabular mineral layer was observed at interval 318-U1357A-8H-8, 54–55 cm, as well as at several deeper levels in Hole U1357A. The mineral contains inclusions of the surrounding sediment and appears to be authigenic. It was first thought to be gypsum on the basis of hardness and texture, but X-ray diffraction (XRD) analysis shows it to be the mineral struvite (see "Geochemistry and microbiology"). Struvite was subsequently observed at multiple locations below Core 318-U1357A-8H. It likely occurs at higher levels as well; core describers initially thought the fragments were bits of plastic core liner. The struvite fragments are most evident when they occur in tabular layers 1–2 mm thick and aligned with laminations. The crystals can be several centimeters across (Fig. F11). Struvite is $NH_4MgPO_4 \cdot 6H_2O$ and is thought to form by bacterial biomineralization processes in anoxic sediments with abundant amounts of ammonium.

Interpretation

We interpret Unit I as a Holocene sequence of laminated diatom ooze representing the product of annual biogenic sedimentation focusing within the 1000 m deep Adélie Basin. This part of the Wilkes Land coastal zone exhibits a large and recurrent polynya (a region of open water surrounded by sea ice) within which intense diatom blooms form during the austral spring and summer. This material is deposited during the austral autumn on the Wilkes Land continental shelf, where it is remobilized and transported until it reaches the protected deep-basin setting of the Adélie site depositional basin. Slightly less biogenic, organic-rich material falls during the austral winter. The alternating high-productivity deposition during summer and less organic-rich sedimentation during winter produces the observed centimeter-scale laminations (e.g., Stickley et al., 2005; Maddison et al., 2006; Denis et al., 2006). The observation of hydrogen sulfide gas at very shallow depth (uppermost meter) in all holes and the presence of persistent laminations throughout the sequence indicate anoxic conditions that prevent larger benthic organisms from disrupting the laminations. The observation of benthic foraminifers, however, suggests that bottom waters contain sufficient amounts of oxygen to sustain small organisms living at the sediment/water interface.

Unit II

Interval: 318-U1357A-19H-1, 115 cm, through 20H-CC, 85 cm
Depths: 170.25–185.60 mbsf
Age: earliest Holocene

Unit II consists of clay-bearing to clay-rich olive-green diatom ooze with distinct laminations (Fig. F12) as well as layers of structureless diatom-rich sand and sandy silt. The boundary between Units I and II is marked by an abrupt downward increase in clay, silt, and sand content. Sand layers and pockets, gravel, and faceted pebbles occur in the lower part of Core 318-U1357A-19H. Core 20H is similar in appearance to the lowermost portion of Core 19H but exhibits signs of drilling disturbance. This core likely hit the diamict during the APC process, did not fully stroke-out, and possibly sucked in additional sediment. Vertical flow-in features are observed in all of Section 318-U1357A-20H-2 and in interval 318-U1357A-20H-3, 0–130 cm. Sections 318-U1357A-20H-4 through the base of 20H-CC show well-defined centimeter-scale color banding ranging from reddish brown to greenish gray to yellowish gray (Fig. F13). These bands are more strongly bowed near the margins of the core liner than those from Cores 19H and above. The frequency of silt-bearing layers (Fig. F14) and abundance of sand and gravel increases toward the base of Core 318-U1357A-20H. Nevertheless, well-preserved diatoms are continuously observed to the base of Unit II (Fig. F15).

Interpretation

We interpret this unit as forming immediately after ice retreat from the Adélie Basin during deglaciation at the end of the last glacial interval. Meltwater from the rapidly receding ice margin, some of it likely introduced subglacially to the calving margin, carried in larger amounts of terrigenous debris. This unit contains diatoms, and the thickness of the layering, relatively high degree of compaction, and high biosiliceous content suggests an extremely high productivity environment. The multicolored layered interval observed in Core 318-U1357A-20H is similar in appearance to the siliceous mud oozes defined by Leventer et al. (2006) as representative of the initial sediments accumulated in shelf basins of the East Antarctic margin during and immediately following initial ice margin retreat. The model of a calving bay reentrant proposed by Domack et al. (2006) and Leventer et al. (2006) may well be applicable for explaining the production and preservation of laminated (possibly varved) and rapidly deposited deglacial biogenic sediments at the Adélie site. In this model, as the Antarctic ice sheet melts and sea level rises, grounded ice on the continental shelf lifts off first from deep basins and troughs while remaining pinned at banks and ridges. Differential ice sheet flow and calving then creates embayments in the retreating ice margin that manifest as ice-walled fjords. The 1000 m deep Adélie Basin cored at Site U1357 is surrounded by relatively shallow banks, so ice liftoff and breakout to form an ice-walled fjord seems likely during the initial phases of sea level rise and ice sheet melting. Only after the embayment is removed by continued ice-margin retreat to the south does normal pelagic, polynya-fueled sedimentation resume. The centimeter-scale brightly colored layers in this unit are similar to those described as early ice-retreat biogenic facies by Stickley et al. (2005) and Maddison et al. (2006).

Unit III

Interval: 318-U1357A-21X-CC, 0–14 cm
Depths: 185.60–185.71 mbsf
Age: latest glacial to earliest Holocene

Unit III consists entirely of a highly lithified, carbonate-cemented, gravelly mudstone recovered from the core catcher of Core 318-U1357A-21X (Figs. F16, F17). The mudstone contains clasts of different lithologies including rock fragments of diorite, metasediment, quartzite, and volcanic debris. Larger grains are supported by a matrix composed of silt and clay minerals with subordinate carbonate. Carbonate cements are present as both vein fill and grain coatings.

Interpretation

Unit III is interpreted as a portion of the uppermost last glacial diamict. It is not known exactly how much of Unit II is missing from the section recovered above the diamict, but we estimate <1 m based on the downhole core barrel positions.

Biostratigraphy

Systematic core catcher paleontology samples were not taken from the millimeter- to centimeter-scale laminated diatom oozes recovered at Site U1357 in order to preserve a more complete stratigraphy for postcruise investigations. Instead, whole-round samples were collected at section breaks only when core expansion pushed material out of the core liner, and selected samples from Hole U1357A were examined for siliceous microfossils, foraminifers, and palynomorphs. Additional targeted toothpick samples within the split core from Hole U1357A were taken at an average frequency of two samples per core through Core 318-U1357A-19H. Section break samples were collected from Cores 318-U1357A-1H through 9H (0–84.64 mbsf), 318-U1357B-2H

through 6H (2.5–50.43 mbsf), and 318-U1357C-3H through 7H (18.30–66.41 mbsf).

All section-break samples yield diverse assemblages of well-preserved diatoms, common to abundant radiolarians, and rare to few silicoflagellates and sponge spicules. Ebridians, actiniscidians, and chrysophyte cysts were not recorded. Sieved sample splits contain benthic foraminifers and abundant, well-preserved planktonic foraminifers as well as fish skeletal debris. All samples processed for palynology yield rich, highly diverse palynomorph associations with very good preservation; palynomorph associations are dominated by dinoflagellate cysts and zooplankton remains. Noteworthy are thecate (motile) dinoflagellates, tintinnid loricae, copepod eggs, and other copepod remains. The fossil assemblages examined from Site U1357 sediments do not contain reworked constituents.

Available biostratigraphic datums do not provide age control within the Holocene (see **"Biostratigraphy"** in the "Methods" chapter). Therefore, shipboard micropaleontologic efforts were focused on (1) identifying foraminifer-bearing intervals for immediate sampling to prevent foraminifer dissolution (see **"Lithostratigraphy"**) and (2) characterizing microfossil assemblages to guide postcruise sampling.

Siliceous microfossils

Cores 318-U1357A-1H through 18H (0–170.25 mbsf) contain well-preserved and abundant biogenic silica (opal-A) dominated by diatoms with variable abundances of radiolarians, silicoflagellates, and sponge spicules. Filamentous diatoms and *Chaetoceros* spp. setae, sponge spicules, and radiolarian needles all contribute to a fibrous sediment texture. In Cores 318-U1357A-19H and 20H (170.25–185.45 mbsf), laminations comprising abundant, well-preserved biogenic silica (Fig. **F18A–F18C**) are interspersed with more siliciclastic laminations in which the biogenic constituents are common to abundant and moderately fragmented (Fig. **F18D, F18E**). Siliceous microfossils were not identified in the diamict (see **"Lithostratigraphy"**) below 185.45 mbsf.

Diatoms are the most diverse microfossil group examined at Site U1357, and the assemblages include many species for which modern environmental preferences have been characterized (Armand et al., 2005; Crosta et al., 2005b), making Site U1357 well suited for paleoenvironmental reconstruction.

Diatoms

A characteristic Holocene Southern Ocean diatom flora with varying contributions from the sea ice–associated and cool open-ocean taxa of Armand et al. (2005) and Crosta et al. (2005b) was identified in all samples analyzed through the biosiliceous sedimentary sequence (the upper 185.45 mbsf) of Hole U1357A (Table **T3**). In most samples diatoms are abundant with no evidence of dissolution and good to moderate preservation (Table **T4**). In samples taken from discrete siliciclastic laminations between 170.25 and 185.45 mbsf, diatoms are few to common with moderate to poor preservation caused by fragmentation, whereas samples taken from adjacent biosiliceous-rich laminations contain abundant well-preserved diatoms, sometimes as near-monospecific assemblages (e.g., the *Thalassiothrix antarctica* + *Trichotoxon reinboldii*–rich assemblage depicted in Figure **F18C,** which forms a white lamination).

More than 40 taxa were identified from section-break samples in Hole U1357A (see the **"Appendix"**); however, these samples were disturbed to such a degree that laminations could not be visually differentiated. Therefore, toothpick samples for diatom assemblage characterization were collected from pairs of discrete laminations in Cores 318-U1357A-1H through 9H (0–84.64 mbsf) and 13H through 19H (112.10–179.29 mbsf). Toothpick sampling is imprecise in comparison to the nondestructive backscattered electron imagery methodologies recently employed in detailed diatom lamination work on coeval sediments from the East Antarctic margin (e.g., Stickley et al., 2005; Denis et al., 2006; Maddison et al., 2006). Even so, distinctions between light and dark laminations are evident in our qualitative assessment (Table **T4**). Within light–dark lamination couplets (Fig. **F6**), the dark laminations generally contain a more diverse assemblage that is often more fragmented. In Cores 318-U1357A-18H through 20H (159.6–184.6 mbsf), centimeter- to millimeter-scale laminations that can easily be distinguished from the light–dark couplets by their unusual color and/or fibrous texture often comprise low-diversity assemblages with excellent preservation, suggesting that these represent single bloom events followed by rapid flux directly to the seafloor. For example, toothpick samples from intervals 318-U1357A-19H-2, 19 and 80 cm (thin white laminations), preserve assemblages dominated by of the open water oceanic needle-shaped pennate diatoms *T. antarctica* and *T. reinboldii* (Fig. **F18C**). Such fine-scale variability highlights the need for further detailed investigation to define the nature and temporal significance of the laminations at Site U1357.

Diatom assemblages characteristic of light and dark laminations vary from couplet to couplet, but with some consistent trends. When present, vegetative *Chaetoceros dichaeta,* vegetative *Eucampia antarctica, Porosira glacialis, Proboscia alata, Proboscia inermis,*

Rhizosolenia antennata var. *semispina,* and *T. antarctica* are always more abundant within the light laminations. *Fragilariopsis kerguelensis* is often more abundant in the light lamina (Fig. **F19A**), although this distinction is one of many that is masked by the coarseness of the relative abundance scheme applied to Expedition 318 diatom micropaleontology (see **"Biostratigraphy"** in the "Methods" chapter), in which a species is categorized as "few" if 11–109 specimens are identified in two 22 mm traverses and "common" if 110–1099 specimens are identified. *Chaetoceros* spp. resting spores dominate the assemblage in all light laminations observed below 144 mbsf (Sample 318-U1357A-16H-3, 59 cm). *Actinocyclus actinochilus,* the cryophilic *Fragilariopsis* species of Armand et al. (2005), and *Thalassiosira antarctica* are generally, but not always, more abundant in dark laminations (Fig. **F19B**). In lamination couplet pairs at ~13, ~24.5, and ~120 mbsf, assemblages within light and dark laminations are similar.

Based on trends in assemblage successions in paired lamination couplets at Site U1357 and on previous work from the nearby Dumont d'Urville Trough (Denis et al., 2006) and other laminated diatom sections from the East Antarctic margin (e.g., Stickley et al., 2005; Maddison et al., 2006), we provisionally interpret each light–dark lamination couplet pair to reflect a single year of biogenic production and accumulation. In this scenario, production initiated during the spring sea ice retreat and persisted through summer in open water, concluding with regrowth of sea ice in autumn. The preservation of a seasonal diatom assemblage succession across the majority of lamination couplets investigated at Site U1357 requires that syndepositional rather than multiannual sediment focusing mechanisms dominate within the Adélie depositional basin. Given this seasonal accumulation model, it is likely that some of the differences in characteristic assemblages from couplet to couplet arise from sampling variability at a subseasonal scale, whereas other differences may be attributed to changing Holocene climate conditions.

Radiolarians

Radiolarians are common to abundant and well preserved in samples examined throughout Holes U1357A, U1357B, and U1357C. The assemblages consist of typical Antarctic radiolarians dominated by *Antarctissa denticulata, Antarctissa strelkovi,* and *Spongotrochus glacialis*. Some Phaeodarian radiolarians that comprise several species of the Family Challengeriidae and some species of *Auloceros, Aulographis,* and *Aulospathis* (Family Aulacanthidae) are preserved. *Auloceros* and *Aulographis* are known to have numerous thin and hollow needles up to 100 µm in length (Fig. **F20**). Along with diatom setae and spines and sponge spicules, these radiolarian needles create the fibrous, papery texture of the sediments.

Silicoflagellates and sponge spicules

The silicoflagellate *Distephanus speculum speculum* (Fig. **F18B**) occurs in common to trace abundance throughout Site U1357. Although additional silicoflagellate taxa were not identified during shipboard examination, postcruise investigation of the silicoflagellate assemblage may contribute valuable information for paleoenvironmental interpretation. Sponge spicules occur in few to trace abundance. Both groups exhibit good preservation.

Palynology

Three samples (318-U1357A-3H-1, 0–20 cm [17.20 mbsf]; 10H-CC [91.80 mbsf]; and 20H-CC [184.45 mbsf]) were processed to evaluate the potential for postcruise investigations. To obtain residues encompassing a particularly wide range of palynofacies, the residues were sieved through a 10 µm mesh, as opposed to the 15 µm mesh routinely used for the samples from the other Expedition 318 drill sites.

All processed samples yield abundant, well-preserved dinocysts and even motile stages of representatives of the heterotrophic genus *Protoperidinium*. In all samples, other organic microfossil remains were encountered, such as worm jaws, copepod eggs, other copepod remains, foraminifer test linings, tintinnid loricae, algal cysts other than those of dinoflagellates, chlorophytes, and ciliate remains. Terrestrial palynomorphs (pollen and spores) were not found. Amorphous organic matter is abundant in all samples.

Foraminifers

Reconnaissance shipboard examination of selected section break samples identified planktonic foraminifers to 79.99 mbsf (Sample 318-U1357A-9H-5, 0 cm) and benthic foraminifers to 37.02 mbsf (base of Core 318-U1357A-4H). A single planktonic foraminifer was also found in a strewn slide from a diatom-bearing terrigenous lamina at 177.04 mbsf (Sample 318-U1357A-19H-6, 45 cm), indicating that foraminifers are preserved at least to this depth. Constant carbonate content (see **"Geochemistry and microbiology"**) and visual identification in split-core halves (see **"Lithostratigraphy"**) provide further evidence that foraminifers are present to the base of the biosiliceous interval. These initial investigations indicate that foraminifers may be present throughout Hole U1357A. Therefore, >1800 samples were subsequently taken to preserve specimens for potential postcruise foraminifer, isotopic, and Mg/Ca ratio studies.

Planktonic foraminifers

Planktonic foraminifers are well preserved and present in relatively high abundances in low-diversity assemblages consisting of two species: *Neogloboquadrina pachyderma* and *Globigerina bulloides*. The former typically accounts for <70% of planktonic foraminifers in Hole U1357A. Such low diversity is typical for Antarctic waters (Berggren, 1992). Their high abundance and good preservation highlights the potential for high-resolution isotopic and Mg/Ca ratio analyses that will be performed postcruise.

Benthic foraminifers

Well-preserved specimens of the calcareous benthic foraminifer species *Globocassidulina subglobosa* and *Triloculina frigida* were found in reconnaissance checks of sieved samples from Core 318-U1357A-4H. These species are typical of bathyal to abyssal environments (van Morkhoven et al., 1986).

Fish skeletal debris

A pocket of fish skeletal debris was identified in a section-break sample from the top of Section 318-U1357A-8H-5 (68.79 mbsf) (Fig. **F19A**) and in samples sieved at 63 µm from 35.60, 54.53, and 68.79 mbsf. Additional intervals of concentrated fish remains identified in the split core are listed in Table **T2.**

Paleoenvironmental interpretation

Diverse phytoplankton assemblages were identified in the laminated diatom oozes recovered from Site U1357. In addition, abundant zooplankton, including protoperidinioid (i.e., heterotrophic) dinoflagellate taxa, zoobenthos, and nekton, provide evidence of a dynamic Holocene trophic structure within the Adélie depositional basin. Dinoflagellate assemblages comprise exclusively protoperidinioid (heterotrophic) taxa. The abundance of heterotrophic, diatom-consuming dinoflagellate taxa, in combination with fish remains, indicates seasonally high productivity in higher trophic levels.

Diatom assemblages from paired laminations include varying contributions from many of the sea ice–associated and open-ocean diatom taxa (Table **T3**) identified in the companion biogeographic surveys of Armand et al. (2005) and Crosta et al. (2005b), providing a framework for initial paleoenvironmental interpretation. Further paleoenvironmental studies, which will integrate data from other microfossil groups such as dinoflagellates, silicoflagellates, and radiolarians as well as from geochemistry, are planned for follow-up shore-based research.

Vegetative valves and resting spores of *Chaetoceros,* one of the most abundant diatom genera in the Southern Ocean, are present in the majority of samples examined in Hole U1357A. In samples between ~144 and 160 mbsf, *Chaetoceros* resting spores dominate the light lamination assemblage in abundances of <100 valves per field of view. In the review of sea ice biogeography by Armand et al. (2005), *Chaetoceros* resting spores are found in maximum abundance in conjunction with minimum annual sea ice duration of 7 months and February sea-surface temperatures (SSTs) between –0.5° and 1.5°C. *Chaetoceros* resting spores also dominate the biogenic flux to the sediments following massive monospecific bloom events in stratified water columns associated with spring sea ice melt (Leventer et al., 1993; Leventer et al., 1996). *Porosira glacialis* (minimum 7.5 months annual sea ice cover; maximum abundance with February SSTs from –1.3° to 2°C; Armand et al., 2005) commonly occurs in combination with maximum *Chaetoceros* resting spore abundance in these deepest couplets. The cold, stratified spring surface conditions inferred from these and other members of the assemblage have previously been recognized in quantitative diatom paleoenvironmental reconstructions from the Dumont d'Urville Trough (Crosta et al., 2008).

Rhizosolenia antennata var. *semispina* and *R. antennata* var. *antennata* (the *Rhizosolenia* pointed group of Crosta et al., 2005b) generally co-vary with *F. kerguelensis* in light laminations. Whereas both groups are included within the open ocean–related assemblage of Crosta et al. (2005b), the two *Rhizosolenia* species are categorized as cool open-ocean taxa (optimal SSTs = 1°–2°C; unconsolidated sea ice during winter, open-ocean conditions during summer; Crosta et al., 2005b) and *F. kerguelensis* is characterized as a pelagic open-ocean species (February SSTs = 1°–8°C; ice free in the summer with as much as 8 months annual sea ice cover; Crosta et al., 2005b). The alternating contributions of these diatoms, in concert with variable abundances of *Thalassiothrix* spp. (February SSTs = 2°–6°C; encountered north of the modern winter sea ice limit; Crosta et al., 2005b), may reflect fluctuations in polynya development and the sea ice regime throughout the middle and late Holocene. It is likely, however, that a component of this variability is an artifact of imprecise shipboard sampling methodology.

Despite the uncertainties inherent in the qualitative initial data set presented in this report, it is clear that the diverse diatom assemblage recovered from Site U1357 provides an excellent foundation for the development of robust, quantitative paleoenvironmental reconstructions from the East Antarctic margin on subseasonal to annual timescales. Future work will link these preliminary interpretations to other lines of evidence from other microfossil groups (notably dinocysts) as well as from geochemical data.

Paleomagnetism

Time permitting, selected archive-half cores from Hole U1357A were measured on the 2G Enterprises cryogenic magnetometer and demagnetized at 5, 10, 15, and 20 mT, but most were demagnetized at only 20 mT after measurement of natural remanent magnetization (NRM). No oriented discrete samples were taken, but 662 unoriented samples taken for other purposes were analyzed for bulk magnetic susceptibility. The isothermal remanence (IRM) and anhysteretic remanence (ARM) were also measured on 585 of these samples.

Results

Natural remanent magnetization

All measurements of NRM and at the 20 mT step from archive halves from Hole U1357A are shown in Figure **F22A** and **F22B,** respectively. The entire archive section was measured at 5 cm intervals, although intervals may contain disturbed sediment, may have no material at all because of extensive whole-round sampling, or may have expanded because of gas. These portions, identified in core photographs, have been deleted in Figure **F22B**.

The declinations for succeeding cores should be randomly oriented and the inclinations should be near –80° on average at this site. We show core top directions from the NRM and after demagnetization to 20 mT in equal area projections in Figure **F23A** and **F23B,** respectively. The NRM data have shallow negative inclinations and even a few positive ones, displaying the distinct characteristics of overprinting by the drill string. The declinations are biased toward the direction of the sample *x*-direction (see Fig. **F9** in the "Methods" chapter for description of sample coordinate system). After demagnetization to 20 mT, the directions are much steeper, with no positive inclinations, but the bias in declinations remains. In fact, the declinations are random around an axis tilted in the direction of the sample *x*.

A bias in declinations has been attributed to a "radial overprint" stemming from distortion of beds during coring (e.g., Acton et al., 2002) or to measurement of split halves that are not centered with respect to the superconducting quantum interference device coordinate system (e.g., Parker, 2000; Parker and Gee, 2002). In the case of Site U1357, the expected geomagnetic-field direction is nearly vertically up. Coring disturbance generally bends layers downward along the side of the core liner, resulting in the net deflections of the magnetization shown in Figure **F24.** The average magnetization in such a case would show a bias away from the double lines in the archive half (the *x*-direction) and not toward them as observed in Figure **F23.** Parker (2000) states:

"Sometimes cores are split in half along their axes, resulting in hemicylindrical samples. These are normally passed through the magnetometer with the cleaved surface horizontal and centered on the axis. Thus the centre of mass of the sample lies below the magnetometer axis, which spoils the symmetry of the simple approximation: we expect effects such as *z* magnetization to appear as signal on the *x* coils."

It seems quite likely that it is the effect of measuring archive halves off-center in the magnetometer that leads to the bias in directions toward the *x*-axis. The only way to compensate for this effect is to do a full deconvolution of the remanence, a procedure that is beyond the capability of the shipboard instrument as currently designed. Ideally, one would measure U-channel or discrete samples centered in the measurement region of an instrument.

Rock magnetic measurements

The susceptibility records from the whole-round and split-section logger tracks were very close to the noise level in complicating hole to hole correlations. The Kappabridge instrument is two orders of magnitude more sensitive than the logger tracks and can produce well-constrained data even on these very weak samples. Moreover, bulk remanence measurements like ARM and IRM are well above the noise level of the instruments and potentially offer another means of hole to hole correlation. We therefore measured these rock magnetic properties on selected samples that had been taken for micropaleontological studies. These augment the relatively noisy track data and also allow us to assess the sediments for the possibility of normalizing the intensity data for relative paleointensity estimates.

Unoriented samples were taken every 10 cm starting at Core 318-U1357A-2H and were air, oven, or freeze dried to prevent the foraminifers from dissolving. We measured 662 samples from Core 2H through 8H on the Kappabridge. ARM and IRM was also measured on samples from Cores 4H through 7H.

Samples were initially measured 10 times to assess reproducibility. A quick study of approximately three measurements each was performed for the middle sections of Core 2H. After analyzing the results, we adopted a protocol of five repeat measurements for each sample, starting just before Section 318-U1357A-2H-6. Samples were measured using the SUFAM program.

ARMs were imparted in the samples using a direct-current bias field of 50 µT in an alternating-current peak field of 100 mT. Step-wise IRMs were given to 14 samples in fields up to 1 T. The saturating field

was ~200 mT, consistent with a magnetite mineralogy. All samples were given a saturation IRM (sIRM) in 500 mT fields. Bulk remanences were all measured in the cryogenic magnetometer.

The total sample mass was determined on all samples using the Mettler-Toledo balance systems in either the Chemistry or Physical Properties laboratories. Sample bag plus label masses were measured on five randomly selected sample bags and measured five times each. The average "bag mass" was then subtracted from all samples to give the sample mass used in normalizing all susceptibility and rock magnetic data.

Discussion

Paleomagnetism

There are large shifts in declination trends in the data shown in Figure **F22B,** many of which span core boundaries. Because core orientation was impossible at this site (virtually at the south magnetic pole), core to core declination is uncorrelated. To examine the long term trends, we assumed that not much secular variation occurred during the missing intervals at coring gaps and we shifted the declination of each succeeding core top to match the last declination of the preceding core. We also shifted the initial declination to 45° to avoid the awkward jump from 360° to 0°. Data after processing are shown in Figure **F25A** and **F24C.**

There is a geomagnetic secular variation model spanning the last 7000 y (CALS7k.2 of Korte and Constable, 2005). This model, similar to the international geomagnetic reference field model, although lower in resolution and accuracy, allows us to predict the geomagnetic field vector anywhere on Earth at 100 y intervals. The declinations and inclinations that are predicted for 66°S/144°E by the CALS7k.2 model of Korte and Constable (2005) are shown in Figure **F25B** and **F25D,** respectively.

A radiocarbon date at 48.72 mbsf from a nearby piston core gives an age of ~2340 y BP (Costa et al., 2007). This provides a loose age constraint in Hole U1357A. At 50 mbsf, there is a long trend in the declination curve (Fig. **F25A**) from a (relative) declination value of 200° at ~70 mbsf decreasing to ~50° at ~37 mbsf. At about the 2000 y mark in the predicted curve (point labeled "3" in Fig. **F25B**), positive values of ~5° decrease to negative values of around –15° (equal to 345° in the modular 360° scale). These trends in declination are both westward, although of different amplitudes. Assuming that these two westward declination trends are the same and that there are no large changes in sediment accumulation rate or hiatuses in the record, we can tie hairpins in the observed declination curve to those in the predicted curve. We label the most easily recognized tie points from 1 to 8 in Figure **F25A.** These tie points are listed in Table **T5,** and we plot the inferred age-depth relationships in Figure **F26.** Note that Core 318-U1357-8H has virtually no recovery because of the sediment "blowing up," resulting in an interval that is difficult to tie to the predicted secular variation curve with confidence.

Several points should be considered when using the age-depth information listed in Table **T5.** First, there is the problem of bias in the magnetic vector estimations inherent in half-core measurements discussed above. Second, the magnitude of the declination trends observed is far larger than those predicted. However, the CALS7k.2 model is heavily smoothed and frequently underestimates the extent of the secular variation at a particular site. We expect this to be especially true for southerly latitudes for which there are scant data available to constrain the details of the model. Third, the trends in inclination are unimpressive. It is likely that the drill string overprint, which compromises the inclination more than the declination, has obscured features that very well may be recoverable in discrete samples with full demagnetization. These caveats aside, the age model in Table **T5** constitutes a testable prediction. If it can be verified at a few horizons, then the rest of the predictions may provide a high-resolution timescale to ~6000 ka for Site U1357.

Rock magnetism

We show a comparison of the sIRM versus susceptibility in Figure **F27A** and versus ARM in Figure **F27B.** The former is quite scattered, probably because susceptibility responds to all electronic spins and orbits in the sample (including the diamagnetic effect of silica), whereas sIRM reflects only the remanence carrying magnetic minerals, here apparently exclusively magnetite. The IRM versus ARM plot, however, is quite linear, suggesting that the magnetic mineralogy is very consistent in grain size. The dominant control of the variability is from changes in concentration of the magnetic phases on a decimeter scale. These data bode well for the potential to normalize intensity data for relative paleointensity studies on discrete samples.

In Figure **F28** we show a comparison of the NGR data (normalized by density; see also **"Stratigraphic correlation and composite section"**), the bulk susceptibility data, and the sIRM data versus meters below seafloor. Whereas some features appear in both the susceptibility and the NGR data (e.g., a marked drop at ~65 mbsf), little correlation in detail is apparent. Moreover, because of the more scattered susceptibility

data with respect to the IRM, good correlation between the susceptibility and sIRM downcore is not apparent. It is possible that large features like those in the susceptibility data at ~43 mbsf could be correlated from hole to hole, but we have no way to insure that this is the case at this point. The sediments are inhomogeneous at a decimeter scale but quite homogeneous on larger scales, making the prospects for relative paleointensity data bright but hole to hole correlation difficult.

Geochemistry and microbiology

Organic geochemistry

Gas analysis was performed typically once per core from Hole U1357A using the methods described in "Geochemistry and microbiology" in the "Methods" chapter.

Methane concentrations varied by four orders of magnitude downhole, from undetected to ~45,000 ppmv (Fig. F29). Levels increase from 5,000 ppmv to a maximum of 43,000 ppmv between 0 and 20 mbsf, decrease to 10,000 ppmv at 50 mbsf, and mostly vary between 5,000 and <20,000 ppmv downhole. Ethane concentrations were negligible (<1 ppmv).

Inorganic geochemistry

Bulk sediments

Ninety-six sediment samples from Hole U1357A were taken for analyses of weight percent carbonate, carbon, nitrogen, and sulfur content, as well as major and trace element analyses (silicon, titanium, aluminum, iron, manganese, calcium, magnesium, sodium, potassium, phosphorus, strontium, barium, vanadium, scandium, and cobalt) (Table T6). Samples were collected in close collaboration with the sedimentology group to sample the main lithologies represented. Sampling density was approximately one sample every other section (0.43–185.7 mbsf).

$CaCO_3$ (in weight percent) was determined on all sediment samples by coulometric methods (see "Geochemistry and microbiology" in the "Methods" chapter). $CaCO_3$ contents vary between 1 and 3 wt% for most of the core (Fig. F30). A distinct carbonate-rich layer with $CaCO_3$ > 9 wt% was found at 126.34 mbsf. $CaCO_3$ content increases slightly below ~177 mbsf and reaches a maximum of 25 wt% in the bottom diamict sample (318-U1357A-21X-CC, 7–9 cm).

Carbon, nitrogen, and sulfur contents were measured on 19 samples (Fig. F31). For most of the core (0.2–152 mbsf), nitrogen and sulfur concentrations are very low (0.20–0.26 and 0.4–0.7 wt%, respectively). Carbon concentrations vary between 1.4 and 2.6 wt%, yielding total organic carbon (TOC) contents of 1 to 2 wt% and C/N ratios of 7–12. Below ~152 mbsf, nitrogen, carbon, and sulfur contents decrease even further. Only the lowermost sample (185.67 mbsf; diamict) stands out, with carbon contents of 3.5 wt%, equivalent to ~0.5 wt% TOC. No obvious differences of carbon, nitrogen, and sulfur concentrations between light and dark laminations were found.

The concentrations of silicon, titanium, aluminum, calcium, magnesium, sodium, potassium, phosphorus, strontium, barium, vanadium, scandium, and cobalt were obtained for 41 bulk sediment samples by inductively coupled plasma–atomic emission spectrophotometry. Representative results are shown in Figure F32 and data are reported in Table T6. Three distinct geochemical intervals can be distinguished: (1) an upper interval (0 to ~175.5 mbsf), (2) a lower interval (~175.5–184.2 mbsf), and (3) the lowest sample analyzed (~185.67 mbsf). These geochemical intervals broadly correlate with lithostratigraphic Units I (laminated "pure" diatom ooze; 0–170.25 mbsf), II (clay-bearing to clay-rich olive-green diatom ooze with distinct laminations; 170.25–185.65 mbsf), and III (highly lithified carbonate-cemented gravelly mudstone (diamict); 186.46–186.6 mbsf) (see "Lithostratigraphy").

The majority of the diatom ooze samples analyzed between 0 and 175.5 mbsf show relatively narrow ranges of elemental concentrations. Silicon dioxide values are high (76–91 wt%) and accompanied by low-concentration levels of TiO_2 (<0.3 wt%), Al_2O_3 (<5.6 wt%), K_2O (<1.5 wt%), CaO (<2.5 wt%), and V (<34 ppm), indicating very low terrigenous contributions to the bulk sediment assemblage. Outliers to this uniform geochemical interval are the carbonate-enriched layer described above (126.34–126.37 mbsf) and the topmost sample (no salt correction was done).

In contrast to the uniform values described for most of the recovered cores from Hole U1357A, the lowermost 10 m show very different geochemical characteristics, pointing to a higher and more variable abundance of terrigenous material (i.e., higher and more scattered values in SiO_2, TiO_2, Al_2O_3, K_2O, and Co). This finding is in agreement with the lithostratigraphy and our own observations during grinding and homogenization (i.e., first macroscopic occurrence of detrital grains and small dropstones from 175 mbsf downhole).

The diamict recovered at the very bottom of Hole U1357A shows the most extreme geochemical values observed at Site U1357 (low SiO_2 and high Al_2O_3, TiO_2, MgO, CaO, V, and Sr).

Diagenetic mineral formation

During core description, several 1–2 mm thick layers of a clear, glassy mineral oriented parallel to the bedding were observed (Sample 318-U1357A-8H-8, 54–55 cm), as well as at several other deeper levels in Hole U1357A (Fig. F11). This mineral has been identified by XRD analyses as struvite ($NH_4MgPO_4 \cdot 6H_2O$), an authigenic phosphate mineral that is commonly formed by bacterial biomineralization in anoxic sediments in the presence of ammonium (see "Pore water chemistry"). Although no shipboard geochemical analyses were carried out on struvite minerals, their occurrence is likely to be of interest in terms of both biogeochemistry and carbonate preservation/overgrowth at Site U1357. González-Muñoz et al. (2008) suggested that struvite formation by *Idiomarina* sp. bacteria strains at modern seawater salinities initiates secondary Ca-Mg carbonate production. If such a process is determined to occur at Site U1357, it may impact the utility of foraminifers found in Hole U1357A for age dating and/or paleoclimatic interpretations based on stable isotope geochemistry.

Pore water chemistry

Forty-three interstitial water samples were taken in close collaboration with the microbiology samples from the uppermost 20 m (0.1–20.35 mbsf) of Hole U1357C (Fig. F33). Shipboard chemical analyses included pH, salinity, chlorinity, alkalinity, dissolved inorganic carbon (DIC), sulfate, phosphate, ammonium, sodium, potassium, magnesium, calcium, boron, manganese, strontium, barium, and silica measurements. The data are provided in Table T7 and are shown in Figures F34, F35, F36, and F37.

Because the topmost cores recovered from Site U1357 were very soupy, extremely porous, and gas-expanded further downhole, near-surface mixing processes and seawater infiltration at core tops was inevitable. In the pore water chemistry data, seawater contamination was recognized by unusually high sulfate contents at all core tops (see "pH, salinity, chloride, and sodium"). We marked these seawater-infiltrated or mixed intervals as shaded bars in Figures F34, F35, F36, and F37 and refrained from any interpretations of the corresponding data (Table T7). Cited values for average seawater composition throughout the text are taken from Millero and Sohn (1992) and Broecker and Peng (1982).

pH, salinity, chloride, and sodium

The pH of pore waters ranges from 7.8 to 7.5, with all values lower than average seawater (pH = 8.1). The pH profile shows some variations for the uppermost 7 mbsf, with pH values from 7.8 to 7.6. Below 7 mbsf, pH decreases progressively to ~7.5 at 20 mbsf (Fig. F34).

Chloride measured by ion chromatography displays a complex trend with decreasing values from 559 to 539 mM in the uppermost 6.2 mbsf and a progressive increase from 539 to 551 mM between 5 and 20 mbsf (Fig. F34). It should be noted that chloride concentrations obtained by titration are not featured in this report, as they are not solely representative of the chloride content itself. The $AgNO_3$ used for the titration reacted with hydrogen sulfides (H_2S) present in the pore waters, yielding erroneous results of decreasing chloride concentration with depth.

Sulfate, ammonium, dissolved inorganic carbon, alkalinity, and phosphate

Sulfate contents in interstitial waters are below detection limit, except for samples around the top of all three cores (1–5 mM at 0.1–0.5, 9.4–11.4, and 19.4–20.3 mbsf) and samples between 1.8 and 2.4 mbsf (Fig. F35).

Ammonium increases almost linearly from near-surface values of 900 to 4500 µM at 18 mbsf. Such high ammonium concentrations reflect a vigorous degradation of organic matter by biotic activity, supported by covariation of ammonium with DIC values (values increase from 39.8 to 79.6 mM at depth) (Fig. F35). The combination of sulfate-free interstitial waters with very high levels of ammonium in the uppermost 20 mbsf suggests that this part of the core is located in the carbon dioxide (methanic) reduction zone.

Alkalinity follows a trend similar to ammonium, with a gradual increase from 50 mM at the surface to 88 mM at ~18 mbsf. However, measured phosphate concentrations in interstitial waters show a more complicated pattern, with pronounced variations between 286 and 610 µM (Fig. F35). This could indicate phosphate removal from pore waters, potentially related with dissolution and/or precipitation of authigenic phases such as the mineral struvite (see discussion above).

Magnesium and calcium

Magnesium and calcium follow a parallel trend with highly variable concentration levels in the uppermost 6.2 mbsf (Mg = ~53.5 to ~55 mM, Ca = 10.67–10.98 mM) (Fig. F36). Between 6.2 and 10.5 mbsf, magnesium and calcium contents increase progressively, reaching 56.5 and 11.5 mM, respectively. From 10.5 to 20.3 mbsf, magnesium concentrations in the interstitial waters vary from 56.5 to 55.7 mM and calcium concentrations range from 11.33 to 11.59 mM.

Potassium, strontium, silica, boron, barium, and phosphorus

Potassium concentrations in interstitial waters show a gradual decrease downcore from a minimum value of 10.6 mM in the shallowest sample (0.1 mbsf) to a maximum value of 12.3 mM at 15.4 mbsf (Fig. F37). All of these values are higher than average seawater (10.2 mM). Two data points at 1.2 and 3.7 mbsf fall outside the described data range (9.7 and 9.8 mM).

Concentrations of silica and strontium in interstitial waters follow parallel patterns, with highly variable values between 386 and 506 µM and 21 to 33 µM, respectively. Two pronounced excursions to lower values can be observed at ~12 mbsf and from 16 to 19 msbf (Fig. F37). Boron values oscillate between 244 and 334 µM, levels that are lower than the average seawater value of 416 µM (Fig. F37). In the lower part of the profile, B values show two pronounced maxima that are anticorrelated to Si and Sr and may be related to an early dissolution and/or recrystalization of opal-A (Bidle and Azam, 1999) and/or specific surface area and sorption changes.

Phosphorous concentrations on the other hand are positively correlated to boron in the lower part of the profile (i.e., below 10 mbsf) and are highly variable in the upper part of the profile (as is the case for B, Sr, and Si) (Fig. F37). An important note for the final interpretation of the P, Si, Sr, K, and B data may be to consider that each interstitial water sample is integrating over several distinct centimeter-scale laminations in the diatom ooze. Hence different levels of oxidation, and their relative representation in each pore water sample, could govern the two apparent levels of concentrations below and above ~320 µM.

Finally, barium concentrations in interstitial waters are generally low and show a convex pattern from 0 to 10 mbsf, with concentrations from 5 to 20 µM. From 10 to 20.3 mbsf, barium shows more fluctuating values, which are not clearly correlated to other elemental maxima and minima described above (Fig. F37).

Microbiology

Microbiological sampling was conducted in Hole U1357C in concert with pore water sampling as highlighted in Figure F33. A high-resolution sampling plan was implemented for the uppermost 20 m of the hole, where 10 cm whole rounds were reserved for onshore phospholipid analyses and molecular 16S rRNA sequencing. Beyond 20 mbsf, 5 cm^3 samples were taken for onshore molecular 16S rRNA sequencing.

Physical properties

Three holes were cored at Site U1357. The physical property measurements program included nondestructive measurements of GRA bulk density and magnetic susceptibility (loop sensor) on all cores and *P*-wave velocity on the cores from Holes U1357A and U1357B. NGR was measured on selected whole-round core sections from Hole U1357A and on all core sections from Holes U1357B and U1357C. Because cores from Hole U1357A were the only ones split onboard, moisture, density, and porosity measurements were performed on samples taken from the working half of each of these sections.

The suite of measurements was adjusted for each hole from information learned from the previous hole at this site. Hole U1357A cores were measured on the Special Task Multisensor Logger (STMSL), which consists of GRA bulk density and loop sensor magnetic susceptibility. These measurements are done as soon as the core is in the laboratory and were to be used for interhole correlation. After thermal equilibration, Hole U1357A cores were run through the WRMSL, which included GRA bulk density, loop sensor magnetic susceptibility, and a *P*-wave logger (PWL). All these measurements were made on all APC cores in Hole U1357A to 184.6 mbsf (Cores 318-U1357A-1H through 20H).

Some core sections in Hole U1357A (Section 318-U1357A-1H-2 and Cores 318-U1357A-5H through 10H and 19H) were also run through the Natural Gamma Radiation Logger (NGRL). However, because of the sensitive nature of the detectors (the cores were leaking gas, water, and sediment from holes drilled to release gas), lithology of the sediments characterized by extremely low measurable counts, and time constraints, it was decided to stop the NGR measurements before core splitting and describing for the remainder of the Hole U1357A cores.

For Hole U1357B, the cores were also run through the STMSL with the overall strategy to use these data for quick correlation to Hole U1357A data for potential adjustment of the drilling offset during drilling Hole U1357C. Afterward, the core sections were allowed to equilibrate to room temperature and were run through the WRMSL. These measurements were made on Cores 318-U1357B-1H through 19H. Later in the cruise, when time permitted, all core sections of Holes U1357B were run through the NGRL.

The first two cores of Hole U1357C were extensively sampled for microbiology and optical stimulated luminescence dating. As such, no physical properties measurements could be made on these two cores. Starting with Core 318-U1357C-3H, all cores from Hole U1357C were measured using the WRMSL.

However, because of experience with the previous two holes, the PWL was turned off during these runs. As with Hole U1357B, when time permitted later in the cruise all core sections in Hole U1357C were measured using the NGRL; otherwise no other measurements were obtained on board.

Whole-Round Multisensor Logger and Special Task Multisensor Logger measurements

Gamma ray attenuation bulk density

GRA density was measured at 5 cm intervals on the STMSL and at 2.5 cm intervals on the WRMSL (5 s and 10 s integration time, respectively). GRA density generally reflects variations in lithology and porosity, and values are as high as 1.3 g/cm^3 (Fig. **F38**).

However, GRA density data are generally of poor quality because these sediments have relatively high gas content, resulting in gas voids, core expansion (Fig. **F38**), and some ruptured core liners. GRA density data were filtered in a two-step process. In order to remove obvious voids and highly gas expanded sections, GRA density values of <0.6 g/cm^3 were removed from the data set. A running average was applied with 10 cm measurement spacing. This filtered data are displayed in Figure **F38**.

Magnetic susceptibility

Whole-core magnetic susceptibility was measured at 2.5 cm intervals (2 s measurement time). Data ranges from about –10 to 2.9 instrument units, with some peaks in Cores 318-U1357A-19H and 318-U1357B-19H, which represent the occurrence of gravel clasts. The magnetic susceptibility of the nearly pure diatom ooze results in data that are near the noise level, except for the basal clay-bearing diatom ooze of Core 318-U1357A-19H. Pilot measurements on discrete samples using the Kappabridge in the paleomagnetic laboratory yield more useful data because the Kappabridge has 100× higher sensitivity than the Bartington sensor on the WRMSL and thus better resolves smaller and/or negative values (see **"Paleomagnetism"**).

Natural gamma radiation

The NGRL measures the NGR of the sediments. However, because of the high purity of these diatom oozes and therefore low levels of clay or other minerals that act as carrier phases for potassium, thorium, or uranium isotopes, a special routine was required to resolve statistically significant results. First, before these analyses were conducted, a site-specific background measurement was obtained. This background measurement requires a 6 h integration time to fully characterize any variation in the site radiation. Additionally, to generate statistically significant results, unusually long integration times were required (600 s per detector position, adding up to a 20 min run time per 1.5 m section). The combination of long integration time and a site-specific background measurement allows the measurement of counts that range from 1 to 18 cps, even while the average background counts are 6 cps. The longer integration time allows for the relative uncertainties in these measurements to be <15% and generally <5%. The NGR data obtained for some cores from Hole U1357A and all cores from Holes U1357B and U1357C were used for an initial attempt to correlate between cores of three adjacent holes (see **"Stratigraphic correlation and composite section"**).

P-wave velocity

Because of the pervasive gas-induced expansion, no valid data were obtained.

Moisture and density measurements

Measurements of density, porosity, and grain density were undertaken on 130 samples taken from Hole U1357A (Cores 318-U1357A-1H through 20H). Dependent on core recovery and quality, one sample was taken per section. These samples were carefully selected to cover the representative lithology of each core section and were taken in undisturbed sediments whenever possible. However, because of pervasive gas pockets these data may be problematic.

Bulk densities (moisture and density [MAD]) from discrete samples are plotted in Figure **F39** and range from 1.02 to 1.31 g/cm^3.

GRA densities and wet bulk densities from samples (MAD) correlate only in the upper 5 m of Hole U1357A. Below 5 mbsf, the GRA density results are consistently lower then those measured on discrete samples. We interpret this to be a result of significant gas-induced core expansion resulting in systematic underestimation of the bulk density as measured by the GRA density meter. Therefore, GRA density results from all three cores should be taken as highly suspect.

Porosity ranges from 50% to 99% and generally decreases with depth (Fig. **F40**).

Grain densities are plotted in Figure **F40.** Grain density as well as wet bulk and dry density (Fig. **F41**) exhibit a slight shift at ~160 mbsf. We interpret this shift to signify the transition from diatom oozes with millimeter-scale gas release texture, which characterizes lithostratigraphic Unit I, to the clay-bearing to clay-rich olive-green diatom ooze that represents lithostratigraphic Unit II (see **"Lithostratigraphy"**).

Moisture content and void ratio show similar trends of decreasing with depth, as expected (Fig. F42).

Stratigraphic correlation and composite section

Physical property measurements of whole-round sections are strongly impacted by the high concentration of diatoms in the sediments as well as pervasive gas expansion and release. Therefore, density (Fig. F43) and velocity data are of very poor quality (or lacking). In addition, magnetic susceptibility is at or below the instrument noise level. Stratigraphic correlation between the three holes at Site U1357 is problematic because of the nature of the available shipboard data (Fig. F43).

Some core sections from Hole U1357A and all core sections from Holes U1357B and U1357C were run through the NGRL (see "Physical properties"). The NGR data from cores from Holes U1357A, U1357B, and U1357C from a comparable depth range (~40–70 mbsf) exhibit very low counts, on the order of 3–5 cps. Nevertheless, a possible characteristic feature (sudden step from relatively higher to relatively lower values) was recorded in all holes, which may serve as a tie point for correlation between the holes (Fig. F44).

A complete composite section may not be possible with these shipboard data and may have to be resolved with shore-based data such as color, core imaging, and X-ray fluorescence scanning.

References

Acton, G.D., Guyodo, Y., and Brachfeld, S.A., 2002. Magnetostratigraphy of sediment drifts on the continental rise of West Antarctica (ODP Leg 178, Sites 1095, 1096, and 1101). *In* Barker, P.F., Camerlenghi, A., Acton, G.D., and Ramsay, A.T.S. (Eds.), *Proc. ODP, Sci. Results,* 178: College Station, TX (Ocean Drilling Program), 1–61. doi:10.2973/odp.proc.sr.178.235.2002

Armand, L.K., Crosta, X., Romero, O., and Pichon, J.-J., 2005. The biogeography of major diatom taxa in Southern Ocean sediments: 1. Sea ice related species. *Palaeogeogr., Palaeoclimatol., Palaeoecol.*, 223(1–2):93–126. doi:10.1016/j.palaeo.2005.02.015

Barnes, P.W., 1987. Morphologic studies of the Wilkes Land continental shelf, Antarctica: glacial and iceberg effects. *In* Eittreim, S.L., and Hampton, M.A. (Eds.), *The Antarctic Continental Margin: Geology and Geophysics of Offshore Wilkes Land.* Earth Sci. Ser., (N. Y.), 5A:175–194.

Berggren, W.A., 1992. Neogene planktonic foraminifer magnetobiostratigraphy of the southern Kerguelen Plateau (Sites 747, 748, and 751). *In* Wise, S.W., Jr., Schlich, R., et al., *Proc. ODP, Sci. Results,* 120: College Station, TX (Ocean Drilling Program), 631–647. doi:10.2973.odp.proc.sr.120.153.1992

Bidle, K.D., and Azam, F., 1999. Accelerated dissolution of diatom silica by marine bacterial assemblages. *Nature (London, U. K.),* 397(6719):508–512. doi:10.1038/17351

Broecker, W.S., and Peng, T.-H., 1982. *Tracers in the Sea:* Palisades, NY (Eldigio Press).

Costa, E., Dunbar, R.B., Kryc, K.A., Mucciarone, D.A., Brachfeld, S., Roark, E.B., Manley, P.L., Murray, R.W., and Leventer, A., 2007. Solar forcing and El Niño–Southern Oscillation (ENSO) influences on productivity cycles interpreted from a late Holocene high-resolution marine sediment record, Adélie Drift, East Antarctic margin. *In* Cooper, A.K., and Raymond, C.R., et al. (Eds.), *Antarctica: A Keystone in a Changing World*. USGS Open-File Rep., 2007-1047:1–6. doi:10.3133/of2007-1047.srp036

Crosta, X., Crespin, J., Billy, I., and Ther, O., 2005a. Major factors controlling Holocene $\delta^{13}C_{org}$ changes in a seasonal sea-ice environment, Adélie Land, East Antarctica. *Global Biogeochem. Cycles,* 19(4):GB4029. doi:10.1029/2004GB002426

Crosta, X., Denis, D., and Ther, O., 2008. Sea ice seasonality during the Holocene, Adélie Land, East Antarctica. *Mar. Micropaleontol.,* 66(3–4):222–232. doi:10.1016/j.marmicro.2007.10.001

Crosta, X., Romero, O., Armand, L.K., and Pichon, J.-J., 2005b. The biogeography of major diatom taxa in Southern Ocean sediments, 2. Open ocean related species. *Palaeogeogr., Palaeoclimatol., Palaeoecol.,* 223(1–2):66–92. doi:10.1016/j.palaeo.2005.03.028

Denis, D., Crosta, X., Zaragosi, S., Romero, O., Martin, B., and Mas, V., 2006. Seasonal and subseasonal climate changes in laminated diatom ooze sediments, Adélie Land, East Antarctica. *Holocene,* 16(8):1137–1147. doi:10.1177/0959683606069414

Domack, E.W., 1982. Sedimentology of glacial and glacial marine deposits on the George V–Adelie continental shelf, East Antarctica. *Boreas,* 11(1):79–97. doi:10.1111/j.1502-3885.1982.tb00524.x

Domack, E., Amblàs, D., Gilbert, R., Brachfeld, S., Camerlenghi, A., Rebesco, M., Canals, M., and Urgeles, R., 2006. Subglacial morphology and glacial evolution of the Palmer deep outlet system, Antarctic Peninsula. *Geomorphology,* 75(1–2):125–142. doi:10.1016/j.geomorph.2004.06.013

Eittreim, S.L., Cooper, A.K., and Wannesson, J., 1995. Seismic stratigraphic evidence of ice-sheet advances on the Wilkes Land margin of Antarctica. *Sediment. Geol.,* 96(1–2):131–156. doi:10.1016/0037-0738(94)00130-M

González-Muñoz, M.T., De Linares, C., Martínez-Ruiz, F., Morcillo, F., Martín-Ramos, D., and Arias, J.M., 2008. Ca-Mg kutnahorite and struvite production by *Idiomarina* strains at modern seawater salinities. *Chemosphere,* 72(3):465–472. doi:10.1016/j.chemosphere.2008.02.010

Korte, M., and Constable, C.G., 2005. The geomagnetic dipole moment over the last 7000 years—new results from a global model. *Earth Planet. Sci. Lett.,* 236(1–2):348–358. doi:10.1016/j.epsl.2004.12.031

Leventer, A., Domack, E., Dunbar, R., Pike, J., Stickley, C., Maddison, E., Brachfeld, S., Manley, P., and McClennen, C., 2006. Marine sediment record from the East Antarctic margin reveals dynamics of ice sheet recession. *GSA Today,* 16(12):4–10. **doi:10.1130/GSAT01612A.1**

Leventer, A., Domack, E.W., Ishman, S.E., Brachfeld, S., McClennen, C.E., and Manley, P., 1996. Productivity cycles of 200–300 years in the Antarctic Peninsula region: understanding linkages among the sun, atmosphere, oceans, sea ice, and biota. *Geol. Soc. Am. Bull.,* 108(12):1626–1644. **doi:10.1130/0016-7606(1996)108<1626:PCOYIT>2.3.CO;2**

Leventer, A., Dunbar, R.B., and DeMaster, D.J., 1993. Diatom evidence for late Holocene climatic events in Granite Harbor, Antarctica. *Paleoceanography,* 8(3):373–386. **doi:10.1029/93PA00561**

Maddison, E.J., Pike, J., Leventer, A., Dunbar, R., Brachfeld, S., Domack, E.W., Manley, P., and McClennen, C., 2006. Post-glacial seasonal diatom record of the Mertz Glacier Polynya, East Antarctic. *Mar. Micropaleontol.,* 60(1):66–88. **doi:10.1016/j.marmicro.2006.03.001**

Marsland, S.J., Bindoff, N.L., Williams, G.D., and Budd, W.F., 2004. Modeling water mass formation in the Mertz Glacier Polynya and Adélie depression, East Antarctica. *J. Geophys. Res., [Oceans],*109(C11):C11003. **doi:10.1029/2004JC002441**

Massom, R.A., Hill, K.L., Lytle, V.I., Worby, A.P., Paget, M.J., and Allison, I., 2001. Effects of regional fast-ice and iceberg distributions on the behavior of the Mertz Glacier Polynya, East Antarctica. *Ann. Glaciol.,* 33(1):391–398. **doi:10.3189/172756401781818518**

Massom, R.A., Jacka, K., Pook, M.J., Fowler, C., Adams, N., and Bindoff, N., 2003. An anomalous late-season change in the regional sea ice regime in the vicinity of the Mertz Glacier Polynya, East Antarctica. *J. Geophys. Res., [Oceans],* 109(C7):3212. **doi:10.1029/2002JC001354**

Millero, F.J., and Sohn, M.L., 1992. *Chemical Oceanography:* Boca Raton (CRC Press).

Newesely, H., 1989. Fossil bone apatite. *Appl. Geochem.,* 4(3):233–245. **doi:10.1016/0883-2927(89)90023-1**

Parker, R.L., 2000. Calibration of the pass-through magnetometer—I. Theory. *Geophys. J. Int.,* 142(2):371–383. **doi:10.1046/j.1365-246x.2000.00171.x**

Parker, R.L., and Gee, J.S., 2002. Calibration of the pass-through magnetometer—II. Application. *Geophys. J. Int.,* 150:140–152. **doi:10.1046/j.1365-246X.2002.01692.x**

Rintoul, S., 1998. On the origin and influence of Adélie Land Bottom Water. *In* Jacobs, S.S., and Weiss, R.F. (Eds.), *Ocean, Ice and Atmosphere: Interactions at the Antarctic Continental Margin.* Antarct. Res. Ser., 75:151–172.

Schenau, S.J., and De Lange, G.J., 2000. A novel chemical method to quantify fish debris in marine sediments. *Limnol. Oceanogr.,* 45(4):963–971. **doi:10.4319/lo.2000.45.4.0963**

Siegert, M.J., Barrett, P., DeConto, R., Dunbar, R., Cofaigh, C.O., Passchier, S., and Naish, T., 2008. Recent advances in understanding Antarctic climate evolution. *Antarct. Sci.,* 20(4):313–325. **doi:10.1017/S0954102008000941**

Stickley, C.E., Pike, J., Leventer, A., Dunbar, R., Domack, E.W., Brachfeld, S., Manley, P., and McClennan, C., 2005. Deglacial ocean and climate seasonality in laminated diatom sediments, Mac.Robertson Shelf, Antarctica. *Palaeogeogr., Palaeoclimatol., Palaeoecol.,* 227(4): 290–310. **doi:10.1016/j.palaeo.2005.05.021**

van Morkhoven, F.P.C.M., Berggren, W.A., and Edwards, A.S., 1986. *Cenozoic Cosmopolitan Deep-Water Benthic Foraminifera.* Bull. Cent. Rech. Explor.—Prod. Elf-Aquitaine, 11.

Williams, G.D., Bindoff, N.L., Marsland, S.J., and Rintoul, S.R., 2008. Formation and export of dense shelf water from the Adélie Depression, East Antarctica. *J. Geophys. Res., [Oceans],* 113(C4):C04039. **doi:10.1029/2007JC004346**

Publication: 2 July 2011
MS 318-105

Figure F1. A. Bathymetric map of eastern Wilkes Land margin showing the location of Site U1357 and other Expedition 318 drill sites. Contour interval = 250 m. Box = approximate area of B. **B.** Bathymetric map of eastern Wilkes Land margin showing location of Site U1357 (black circle) and areas north and west of Adélie Basin.

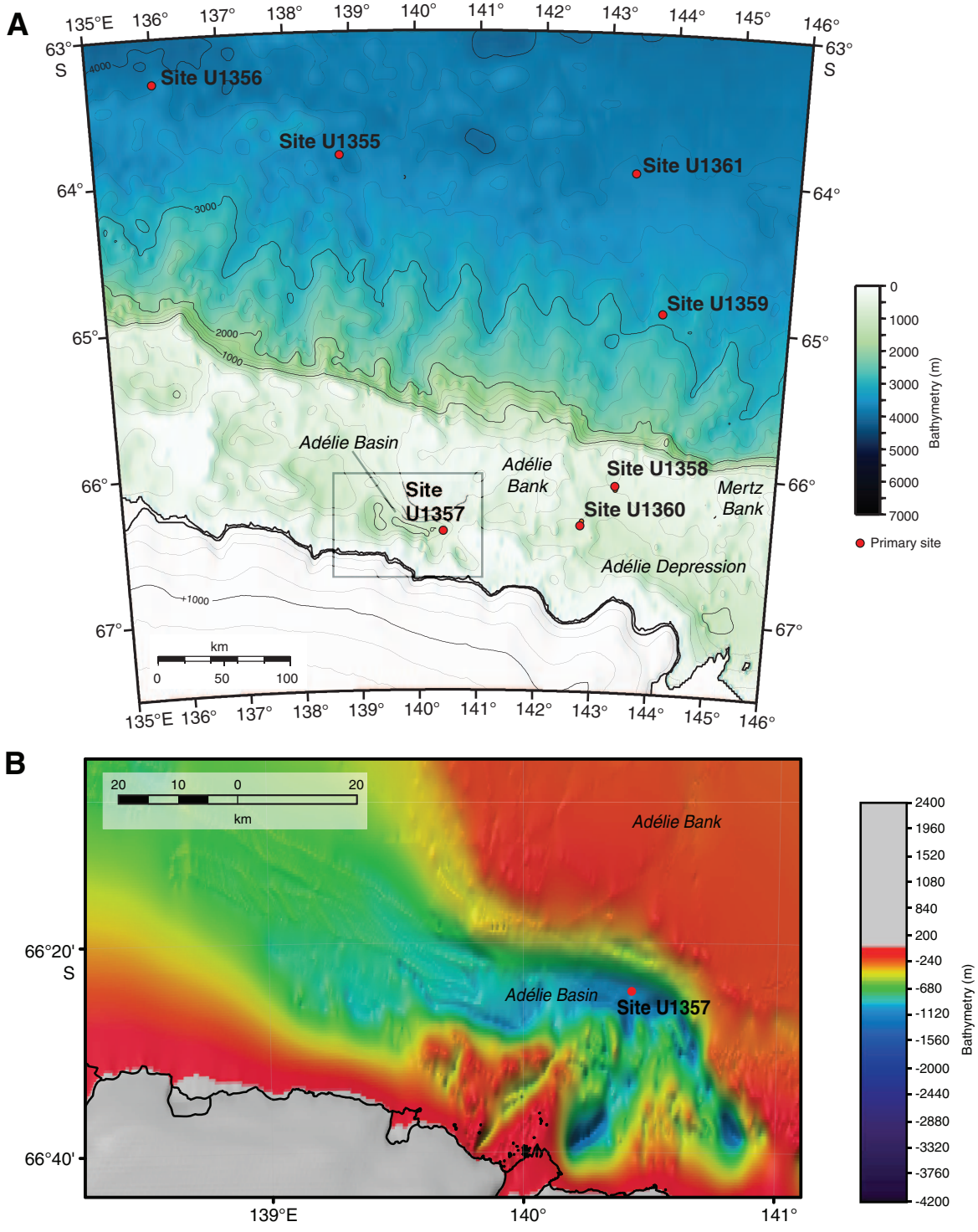

Figure F2. Swath bathymetry map of Adélie Basin in the vicinity of Site U1357. Bold black line = location of ODEC 2000 single-channel seismic line shown in Figure F3. Contour interval = 50 m.

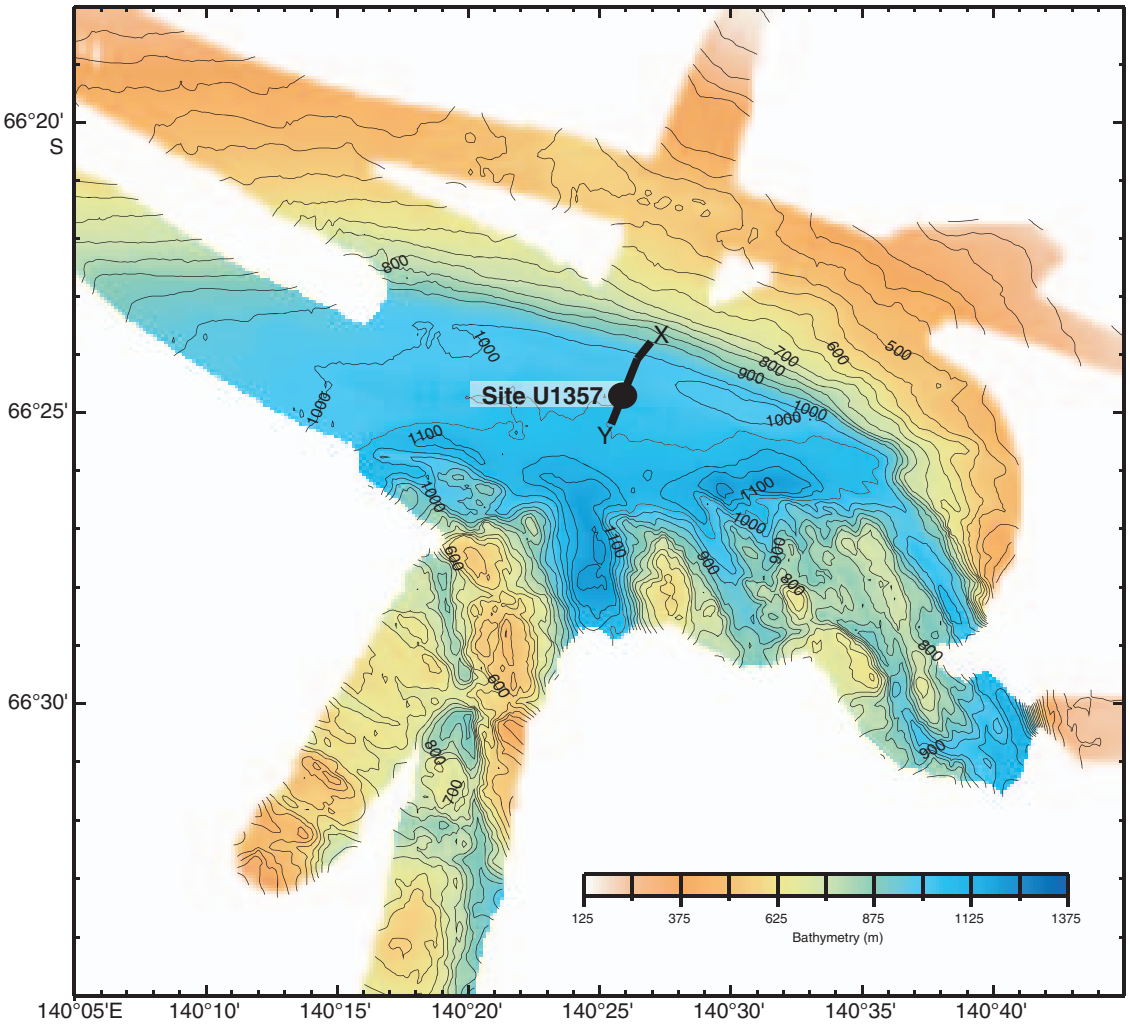

Figure F3. ODEC 2000 single-channel seismic line collected from northeast (X) to southwest (Y) across Site U1357. Red bar = approximate section cored in Holes U1357A–U1357C. Location of seismic profile is shown in Figure F2.

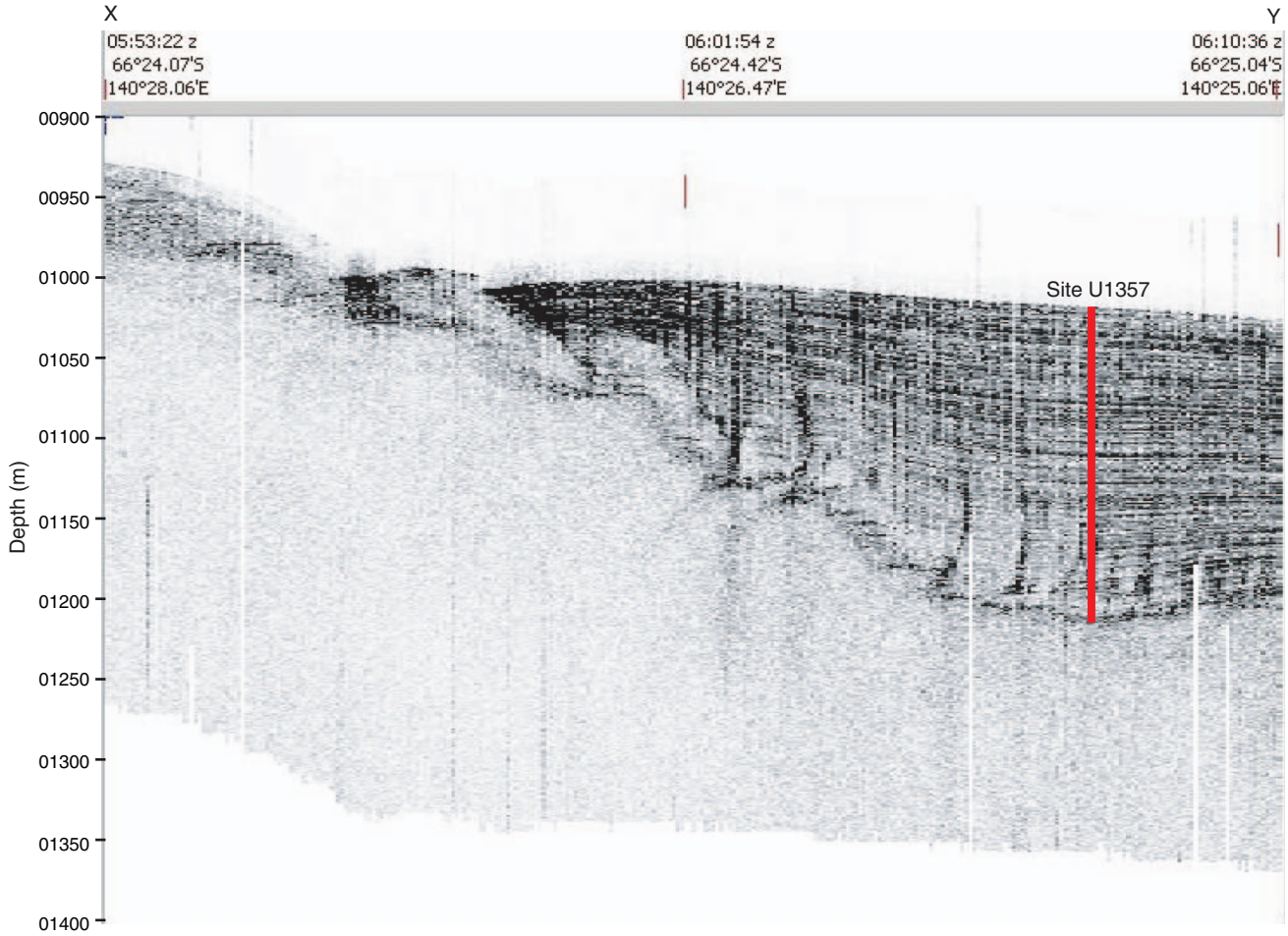

Figure F4. Core image of typical laminations observed in split sections of cores from Adélie Site U1357 (interval 318-U1357A-6H-4, 110–128 cm). Nine to ten laminations, defined here as pairs of color bands, one light and one dark, can be identified. If these features are produced annually, the laminations count over this 18 cm interval implies a sedimentation rate of close to 2 cm/y, similar to average sedimentation rates for the upper 50 m of the Adélie Basin sedimentary section derived from radiocarbon dating (Costa et al., 2007).

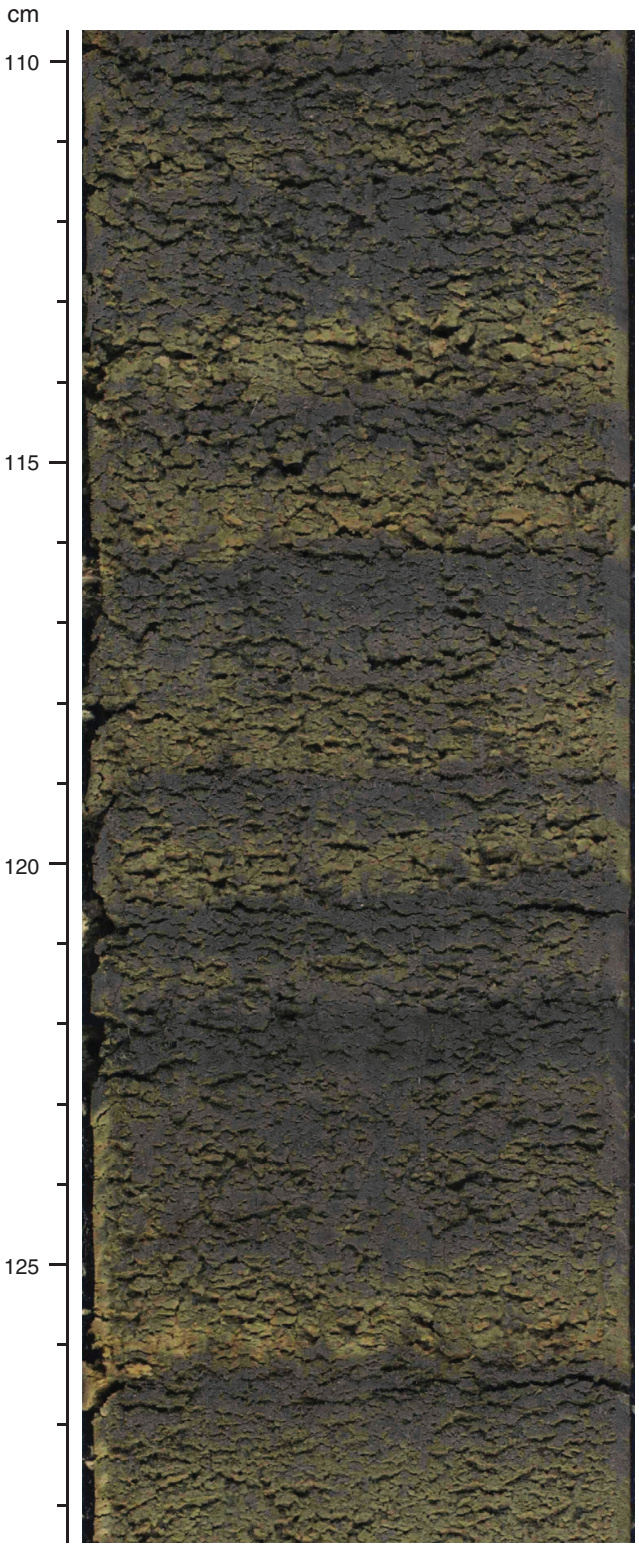

Figure F5. Core images of rapidly changing color in the freshly split surfaces of cores, Hole U1357A (Section 318-U1357A-6H-4). Scanned through the Section Half Imaging Logger. Time intervals are after core splitting and exposure to air.

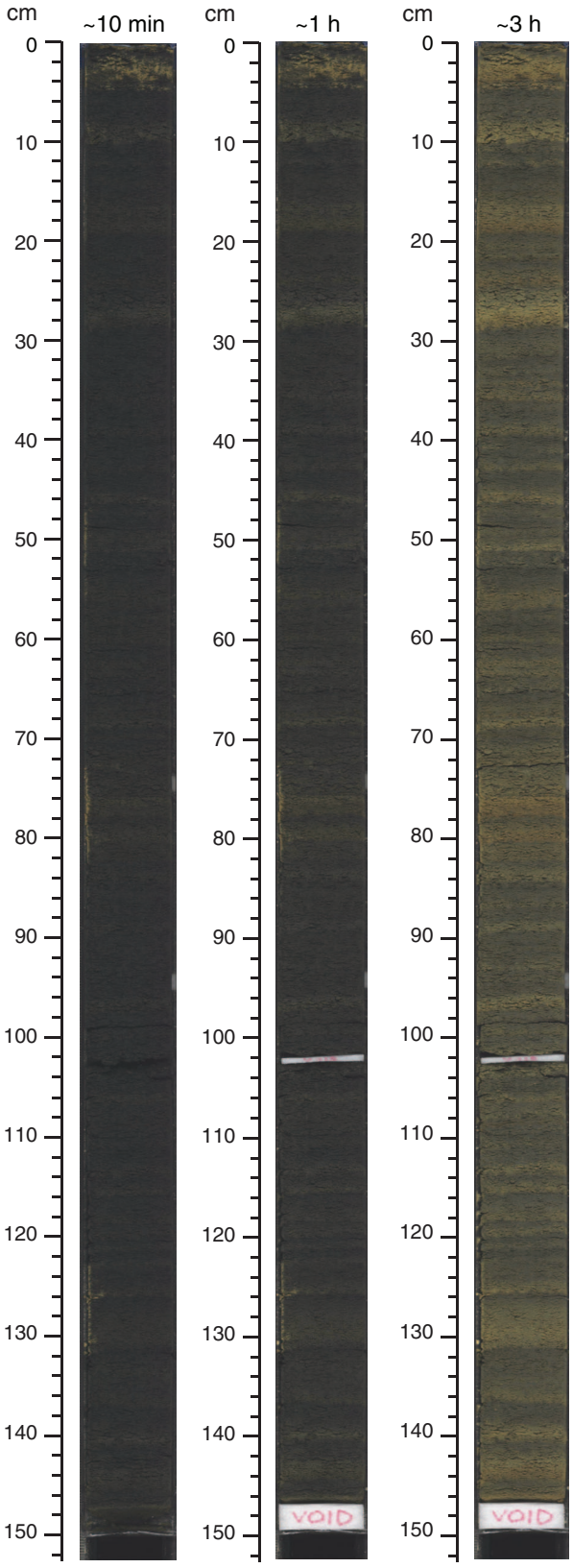

Figure F6. Core image of typical laminations observed at the base of lithostratigraphic Unit I, Hole U1357A (interval 318-U1357A-18H-7, 35–59 cm). As described for Figure F4, if a dark–light couplet represents annual sedimentation, the accumulation rates are slightly higher than 2 cm/y.

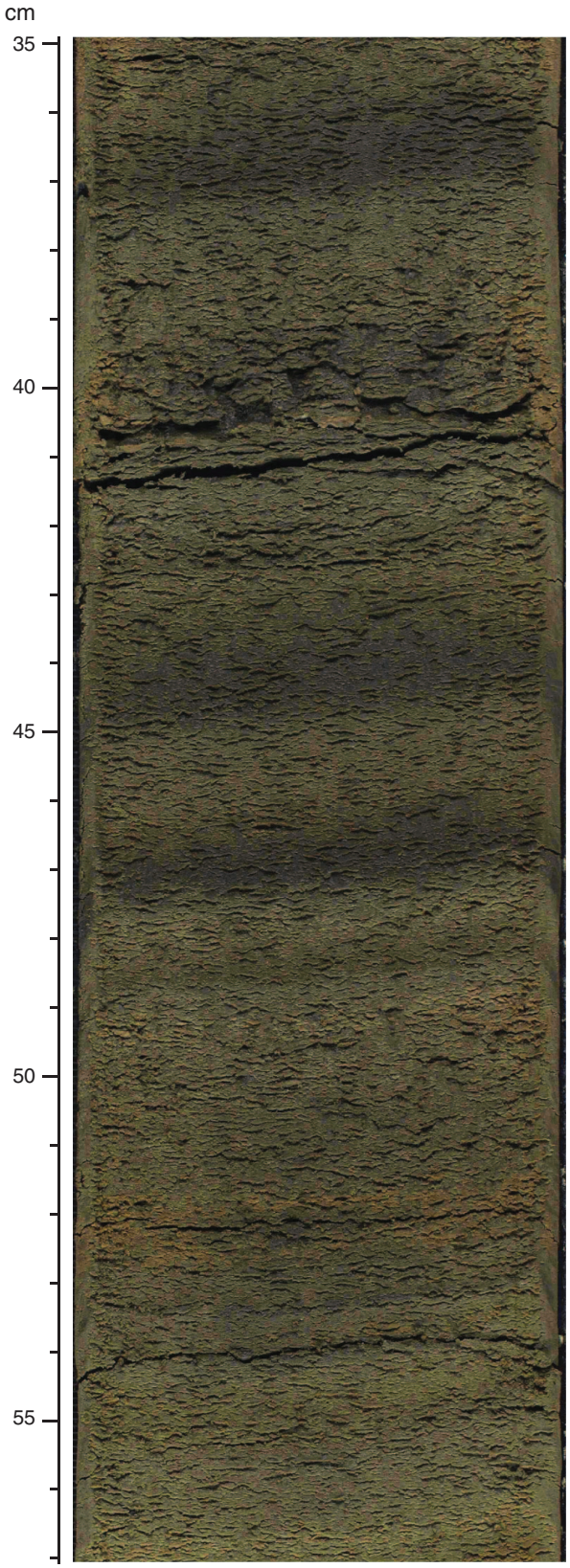

Figure F7. Core image close-up of sediment, Hole U1357A (interval 318-U1357A-7H-2, 55–63 cm). Textures are produced by degassing of H_2S and CH_4 from diatom and organic carbon–rich sediment. Gas release opens up small pockets and fractures that form along natural bedding surfaces and sometimes aggregate and cross-bedding surfaces to form larger (2–5 mm) voids in the core. These features pose a challenge for the use and interpretation of standard track-based logging systems (e.g., magnetic susceptibility and GRA density).

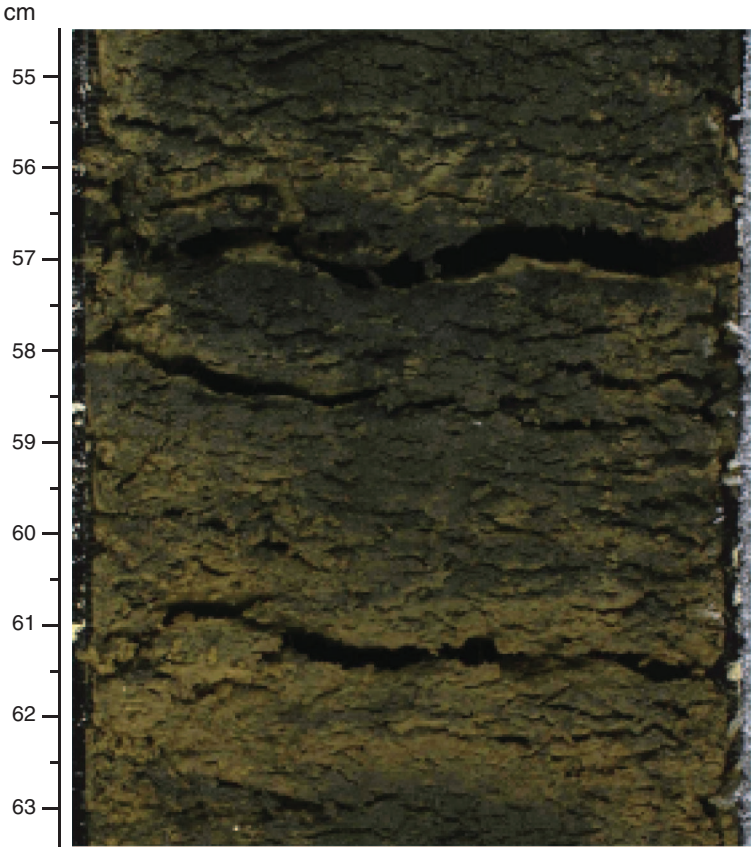

Figure F8. Photomicrograph of well-preserved diatoms representative of the upper portion of the Adélie site sedimentary section, Hole U1357A (Sample 318-U1357A-4H-CC, 40 cm). Diatom preservation in all cores is excellent and there are few, if any, reworked diatoms (see **"Biostratigraphy"**).

Figure F9. Core image close-up of sediment, Hole U1357A (interval 318-U1357A-8H-3, 61–64 cm). Fish vertebrae occur in the white-grained pocket between 62 and 63 cm. Concentrations of fish vertebrae are found throughout the core in layers or pockets. See Table T2 for locations of 48 levels within Hole U1357A with significant concentrations of fish debris.

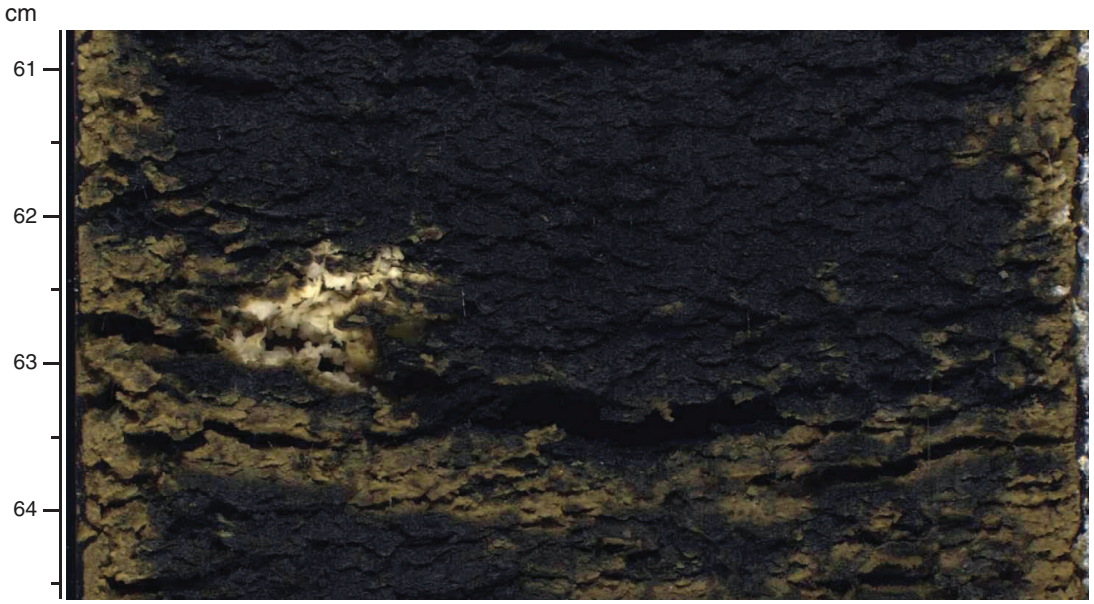

Figure F10. Photomicrograph of prepared (62 µm sieved fraction) slide indicating excellent preservation of biosiliceous materials, Adélie Site U1357 (Sample 318-U1357A-1H-CC). Radiolarian in the center is *Antarctissa strelkovi* Petrushevskaya, a typical component of the modern radiolarian fauna.

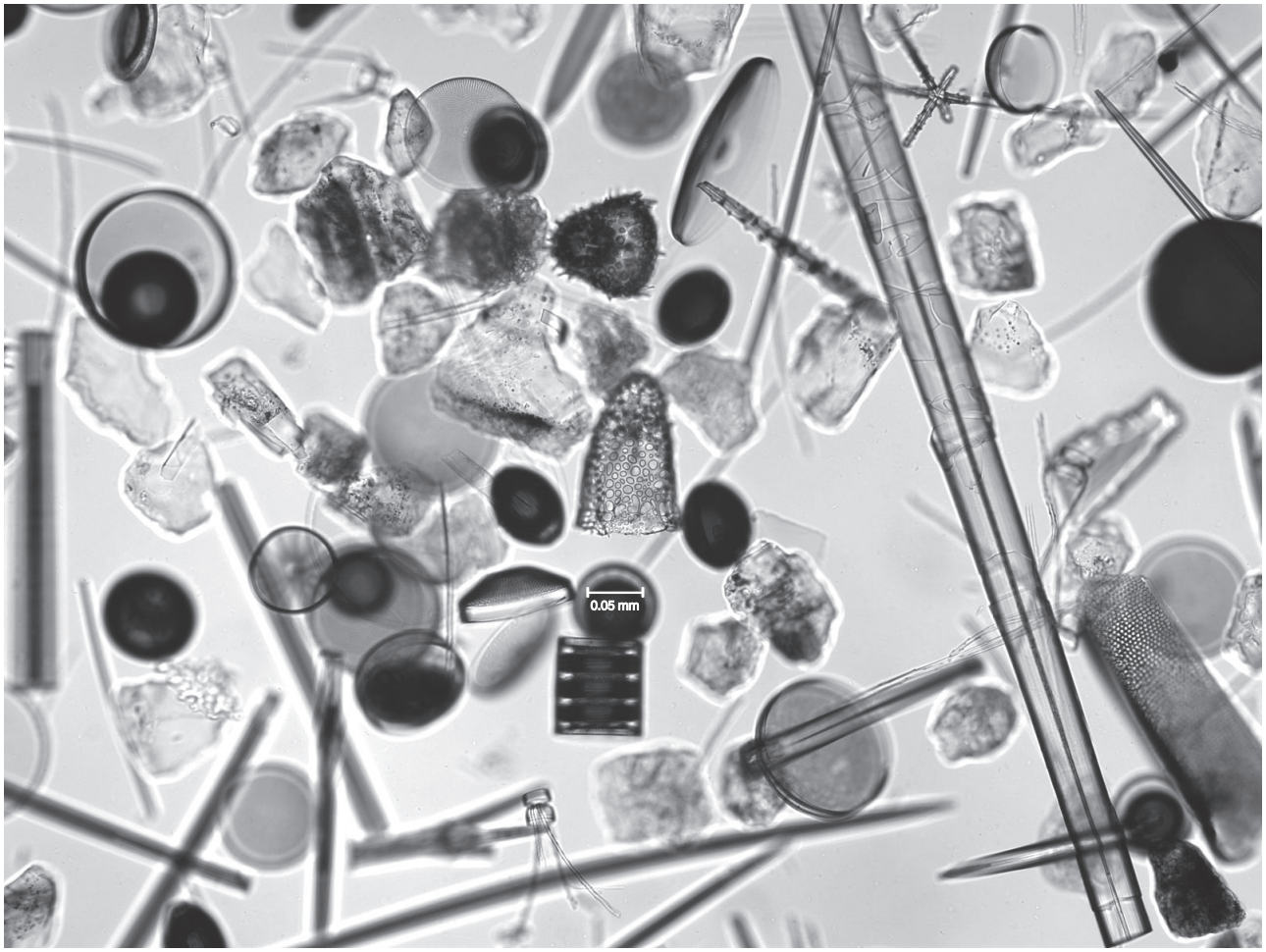

Figure F11. Image of tabular specimen of the mineral struvite, Hole U1357A (interval 318-U1357A-8H-8, 54–55 cm). Struvite is $NH_4MgPO_4 \cdot 6H_2O$ and is thought to form by bacterial biomineralization processes in anoxic sediments with abundant dissolved ammonium. Struvite was mostly observed as tabular crystalline layers aligned parallel with bedding or laminations.

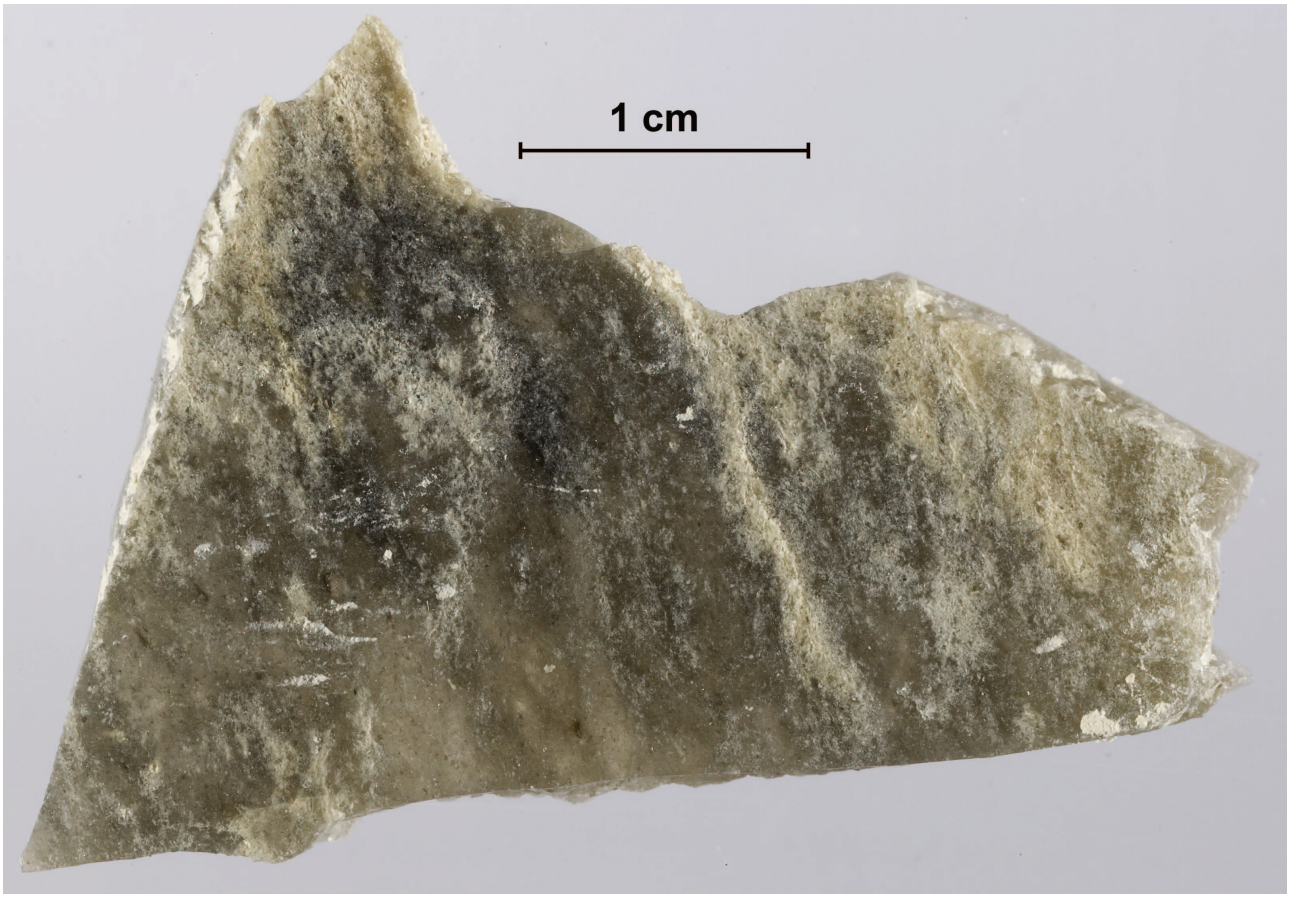

Figure F12. Core image of uppermost section of lithostratigraphic Unit II with distinctive centimeter-scale laminations defined by color, ranging from reddish brown to greenish gray to gray to light gray, Hole U1357A (interval 318-U1357A-19H-5, 48–64 cm).

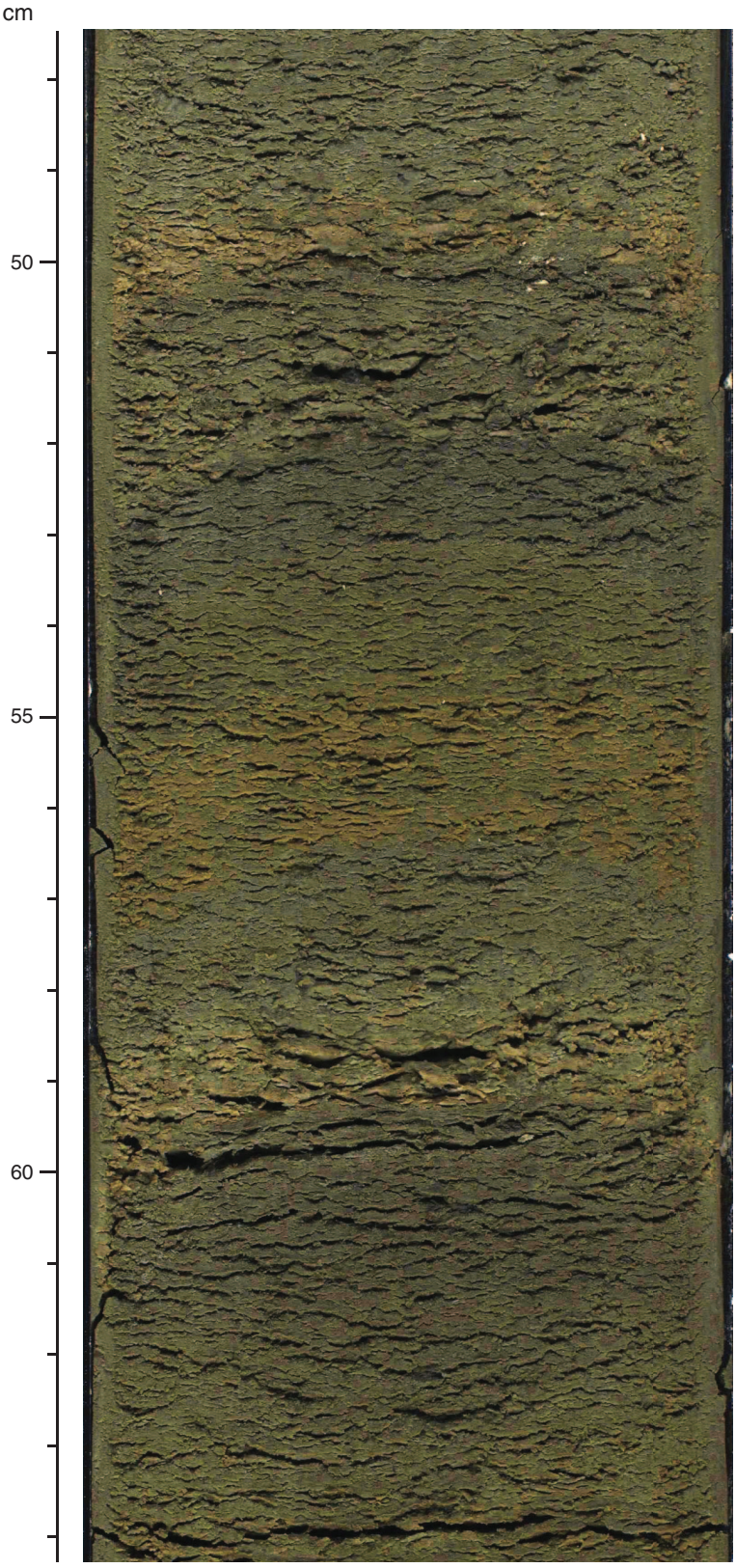

Figure F13. Core image close-up of lowermost section of lithostratigraphic Unit II with distinctive laminations similar to those uphole in Hole U1357A, but multicolored and as thick as 4 cm (interval 318-U1357A-20H-4, 51–61 cm). Laminations from this interval have been significantly bowed by the coring process.

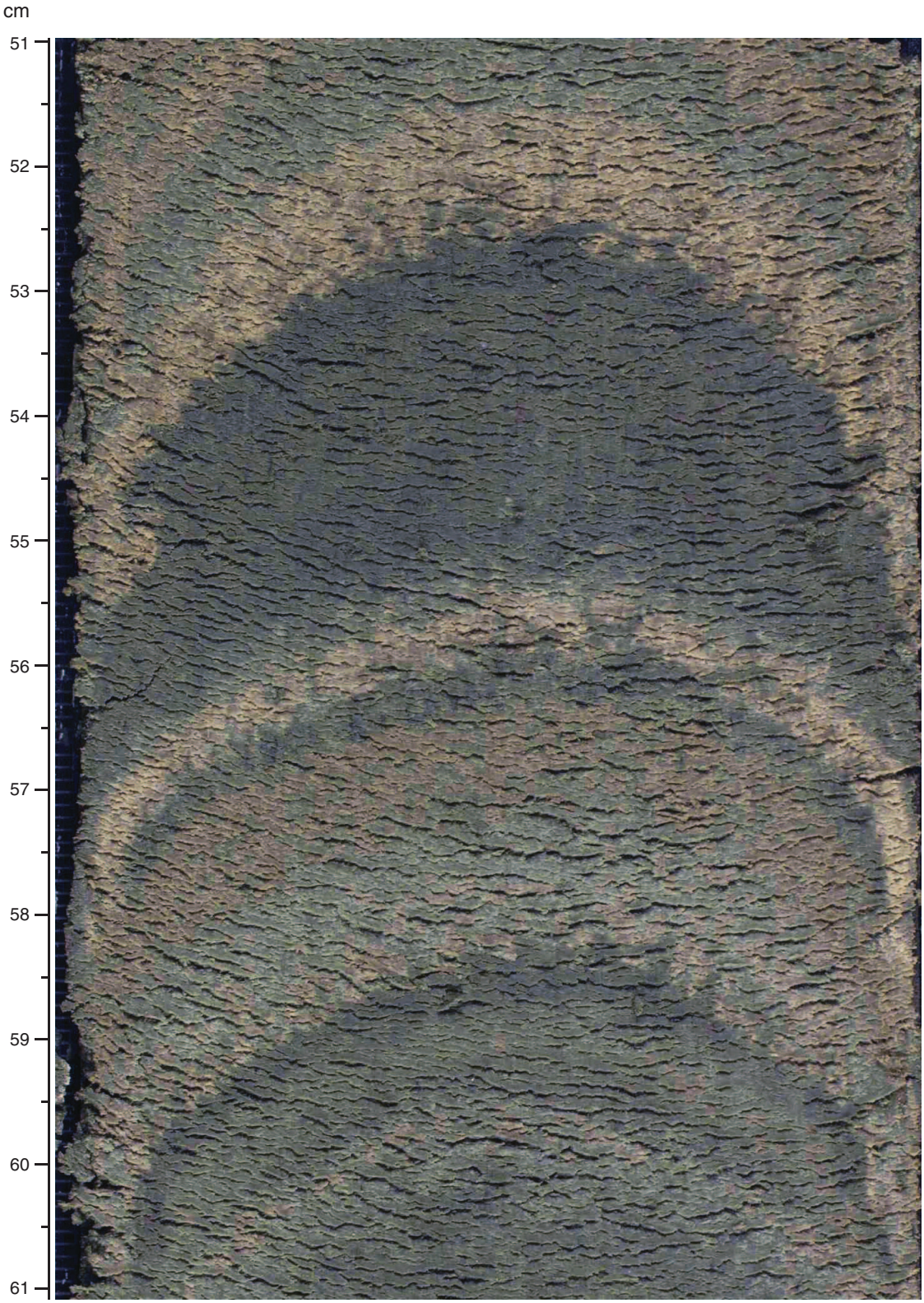

Figure F14. Photomicrograph of silt-rich layer in Core 318-U1357A-20H. Most of the equant silt-sized grains are quartz. Several pieces of broken sponge spicule are also visible.

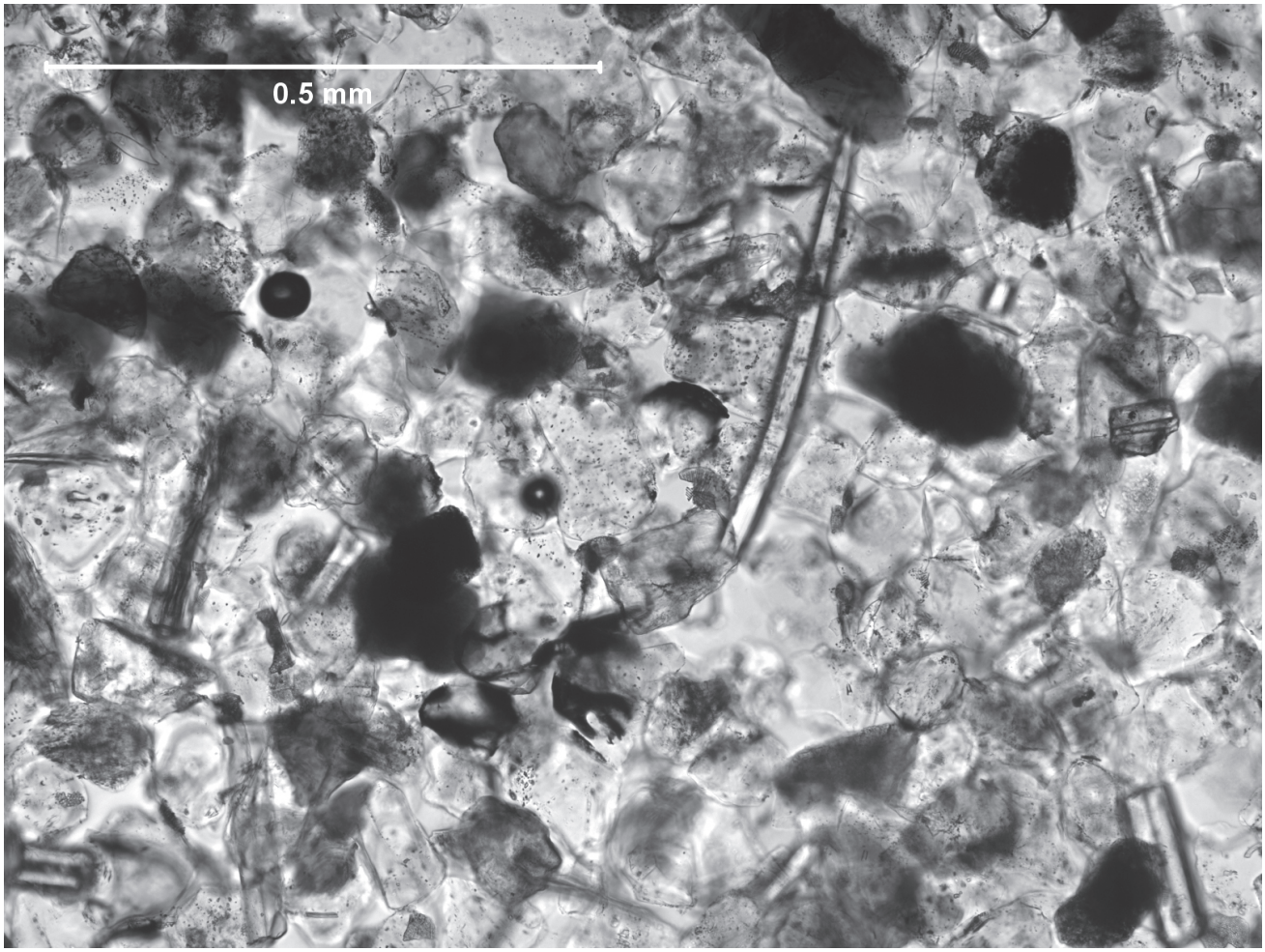

Figure F15. Photomicrograph of well-preserved diatom assemblage observed near the base of lithostratigraphic Unit II, Hole U1357A (Sample 318-U1357A-20H-3, 78 cm).

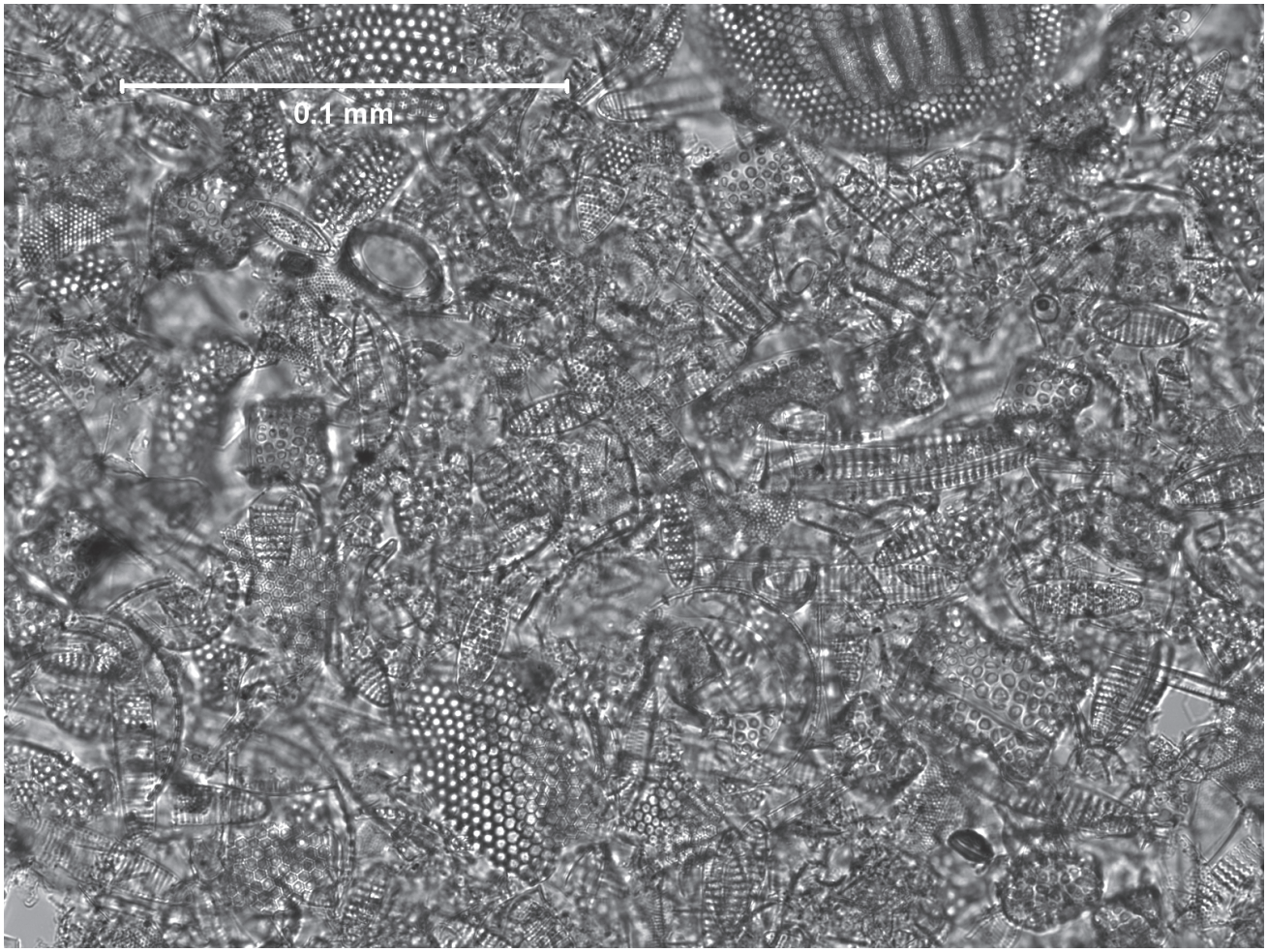

Figure F16. Core image close-up of lithostratigraphic Unit III, Hole U1357A (interval 318-U1357A-21X-CC, 1–10 cm). This unit is a carbonate-cemented, highly lithified, poorly sorted, matrix-supported, gravelly sandy mudstone typical of diamicts on the Antarctic continental shelf.

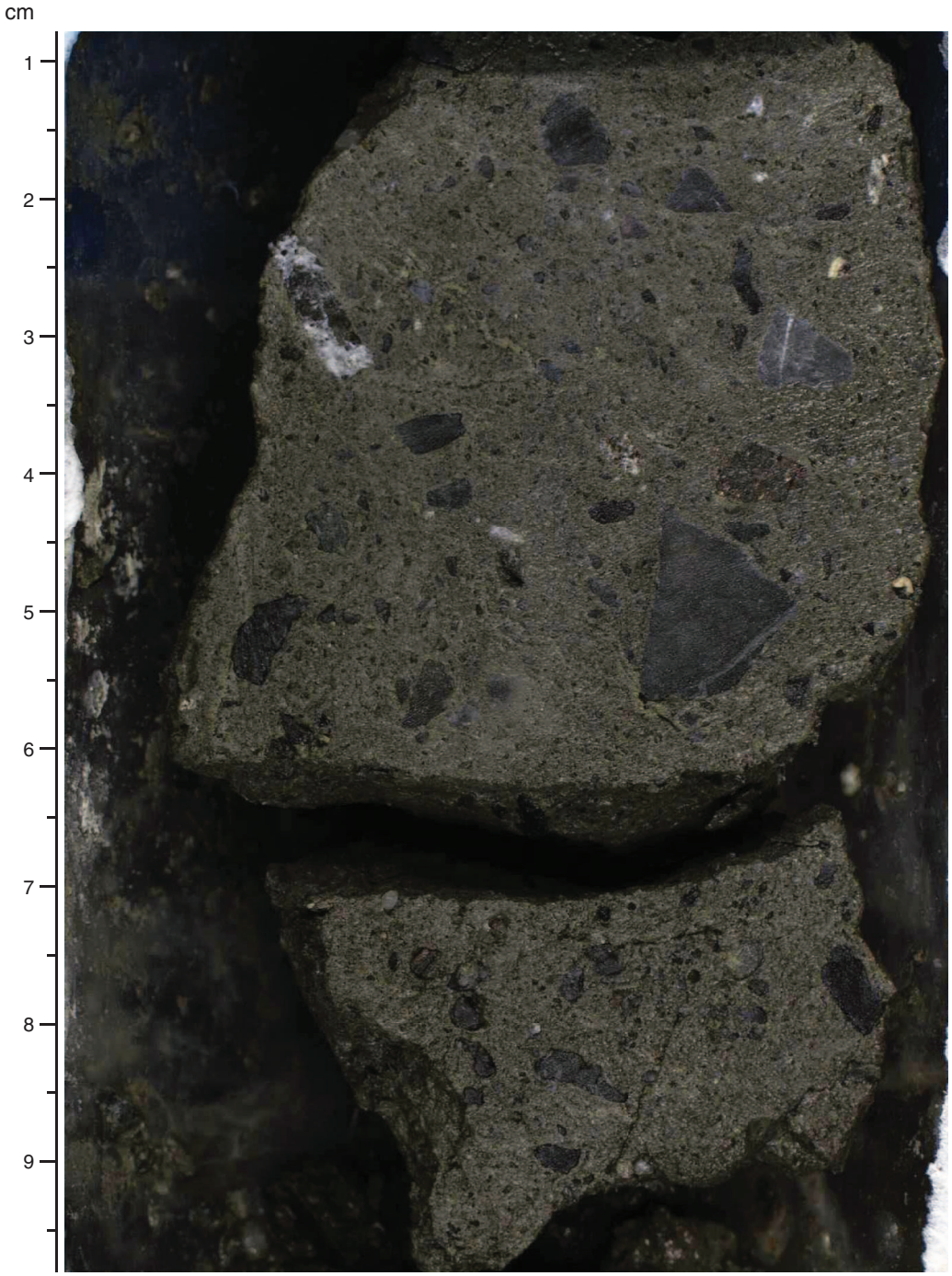

Figure F17. Photomicrograph of a thin section from a chip cut parallel to the core, Hole U1357A (Sample 318-U1357A-21X-CC, 3.5–7 cm). The diamict contains angular rock fragments of metasediments and volcanic and igneous rocks, as well as discrete mineral grains including abundant quartz sand grains. Some of the metasedimentary rock fragments, although angular in appearance within the diamict, contain rounded intraclasts. The matrix is largely mudstone with minor carbonate. Carbonate spar occurs as cements infilling minor voids and fractures. Cross-polarized light.

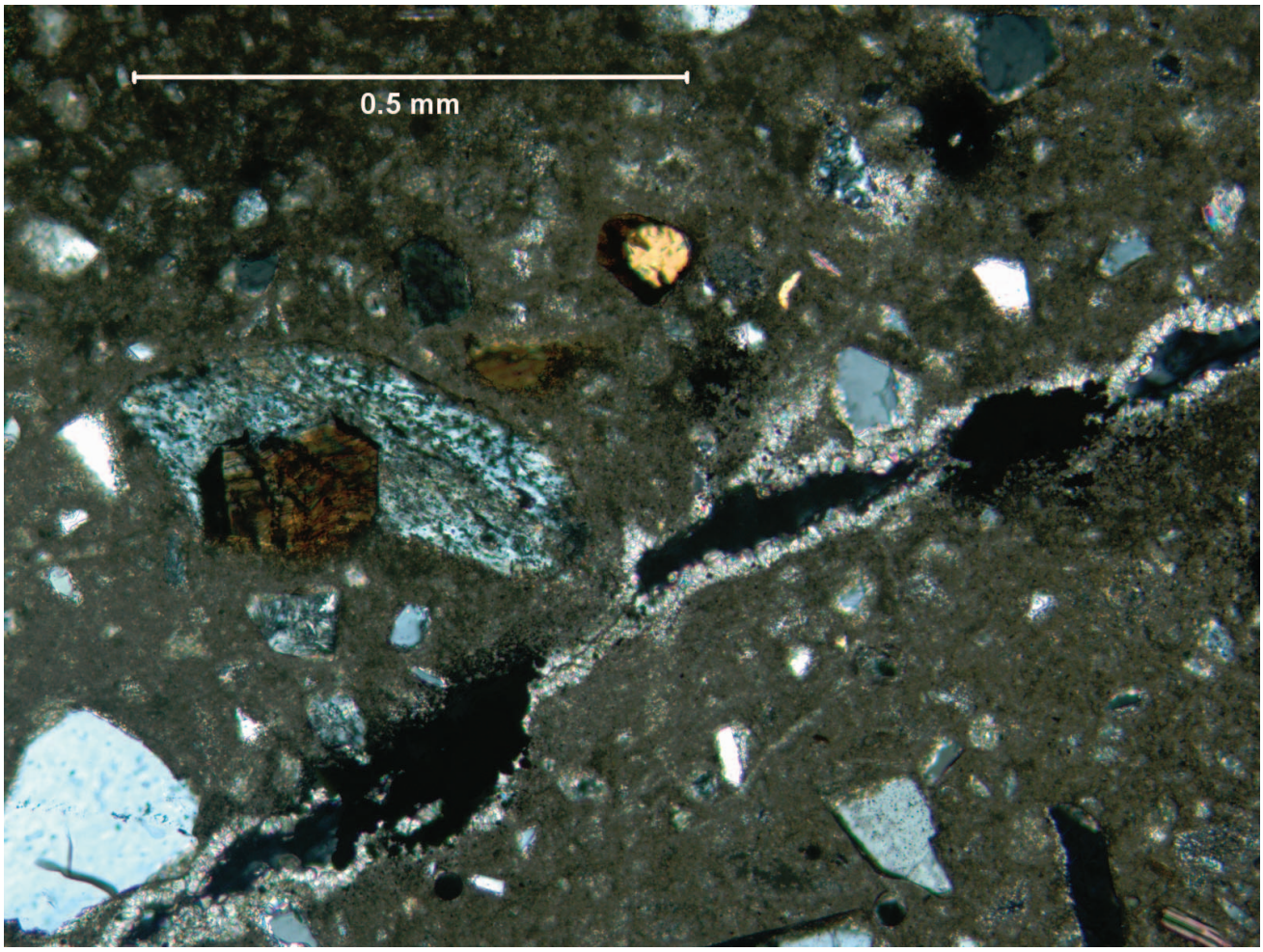

Figure F18. Photomicrographs of representative fields of view from millimeter- to centimeter-scale laminations, Hole U1357A. **A–C.** Biosiliceous-rich laminations; (A) gray fibrous lamina with large centric diatom *Thalassiosira lentiginosa,* a number of *Fragilariopsis* (pennate) species, and *Chaetoceros* resting spores (Sample 318-U1357A-19H-4, 147 cm; 147.00 mbsf); (B) orange lamina with multiple specimens of the silicoflagellate *Distephanus speculum speculum* (hexagonal structures) and numerous *Chaetoceros* resting spores (small dark shapes) (Sample 318-U1357A-19H-1, 86 cm; 169.96 mbsf); (C) white lamina with needle-shaped pennate diatoms *Thalassiothrix antarctica* (narrower pennate) and *Trichotoxon reinboldii* (wider pennate) (Sample 318-U1357A-19H-2, 19 cm; 170.78 mbsf). **D.** Olive-green siliciclastic lamina with several species of *Thalassiosira* (centric diatoms), fragmented pennate diatoms, and *Chaetoceros* resting spores (Sample 318-U1357A-19H-2, 80 cm; 171.39 mbsf). **E.** Black siliciclastic lamina with siliciclastic components and several fragmented pennates (Sample 318-U1357A-19H-6, 45 cm; 177.04 mbsf).

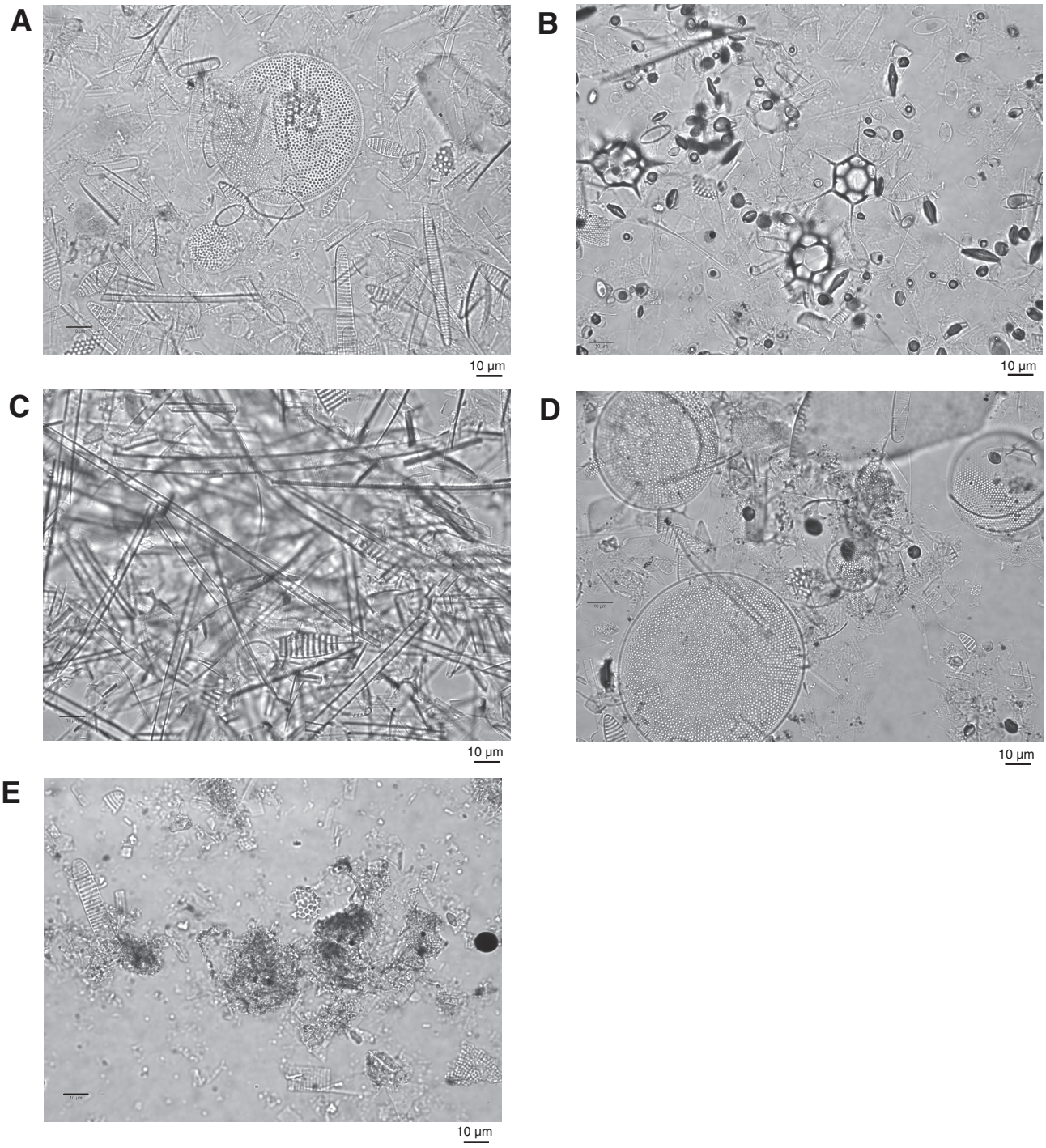

Figure F19. Photomicrographs of representative fields of view of a light–dark lamination couplet pair in Section 318-U1357A-15H-7. Green = open-ocean species (Crosta et al., 2005b), blue = sea ice–associated species (Armand et al., 2005). **A.** Light lamina from 67 cm (138.65 mbsf), where open-ocean species dominate. **B.** Dark lamina from 71 cm (138.69 mbsf), where sea ice–associated species dominate.

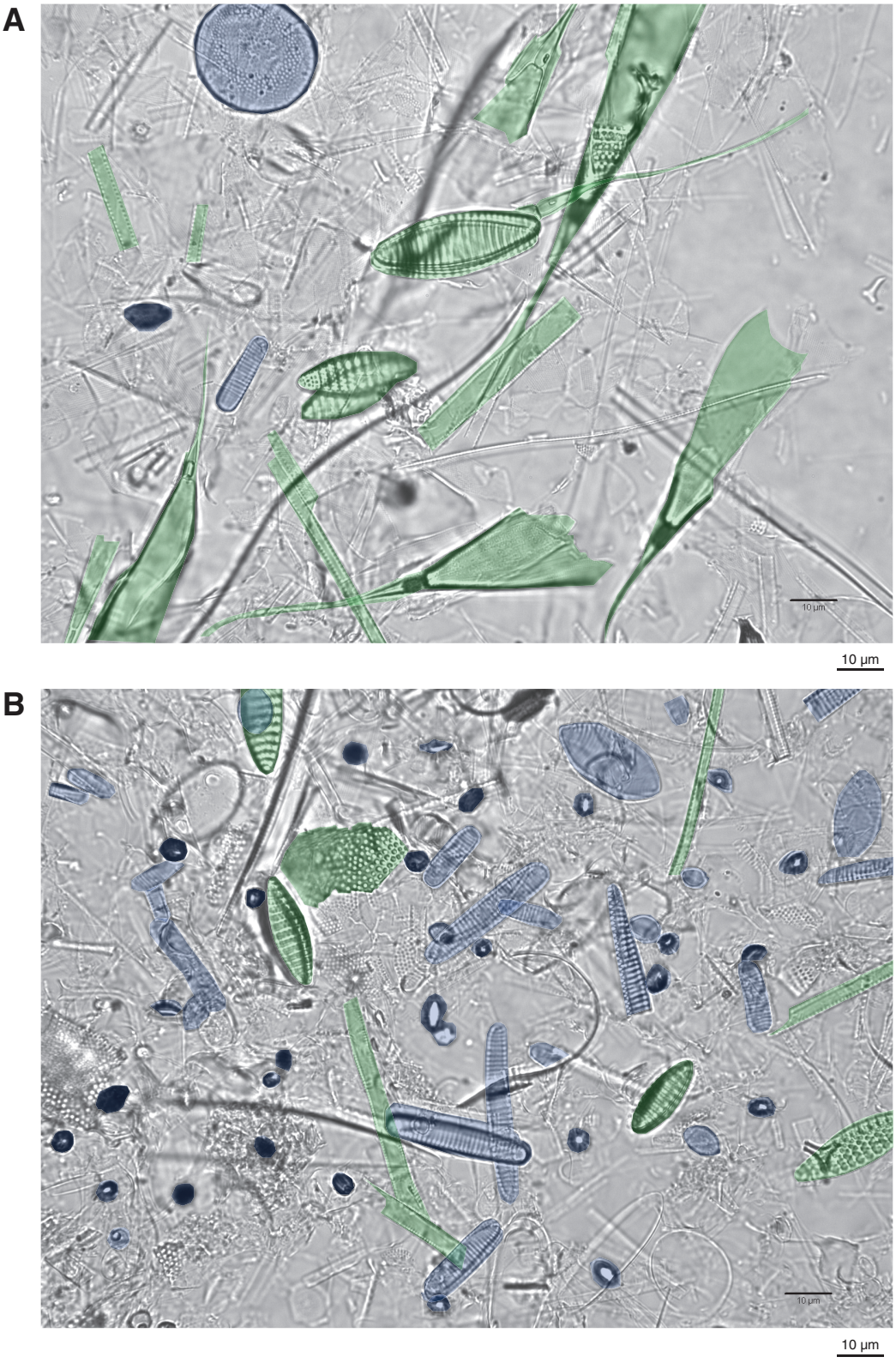

Figure F20. Photomicrographs of thin, hollow needles from the radiolarian genera (**A**) *Auloceros* and (**B**) *Aulographis* identified at Site U1357.

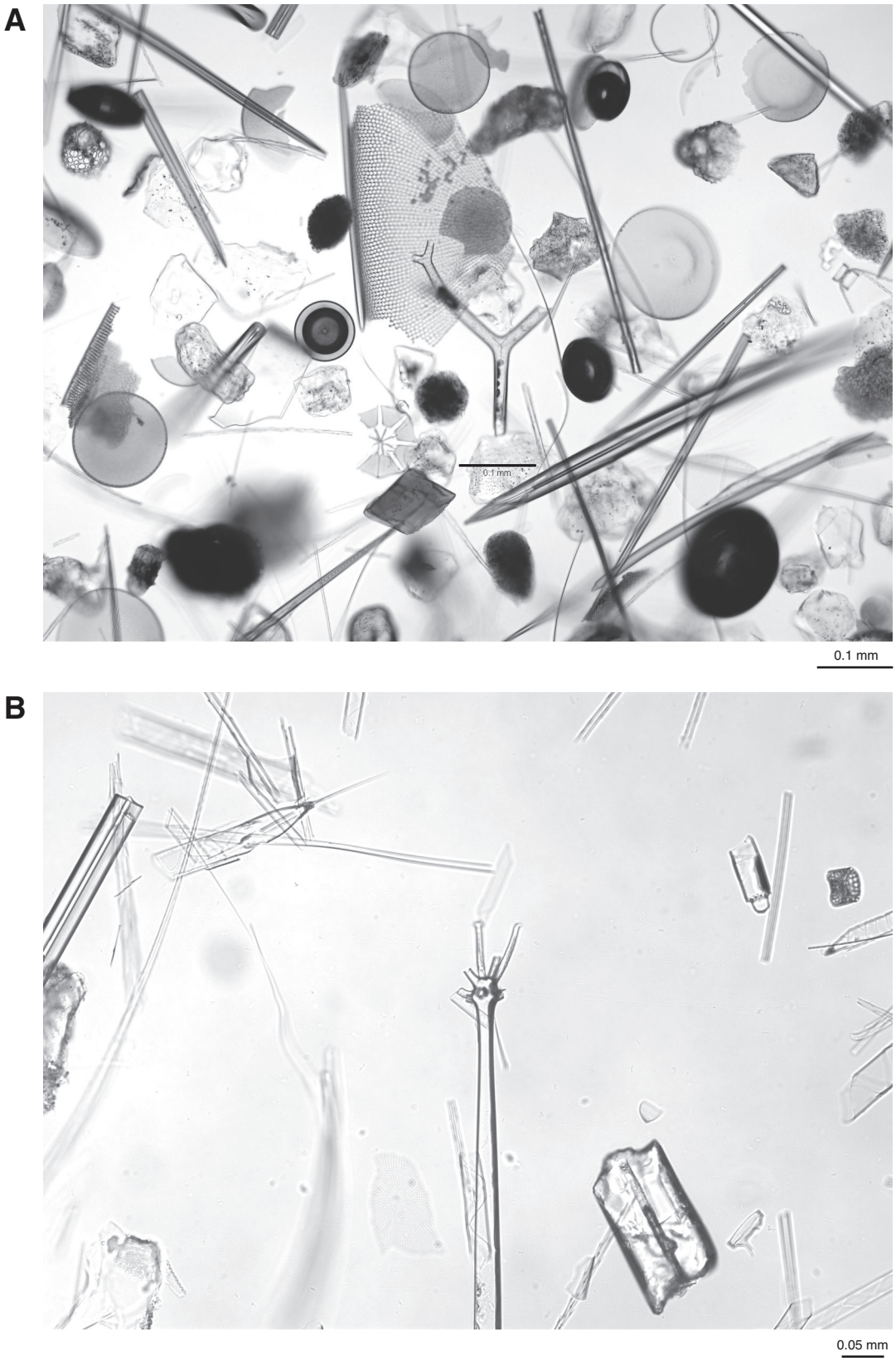

Figure F21. A, B. Close-up images of fish skeletal debris identified in the whole-round section-break sample from the top of Section 318-U1357A-8H-5 (68.79 mbsf).

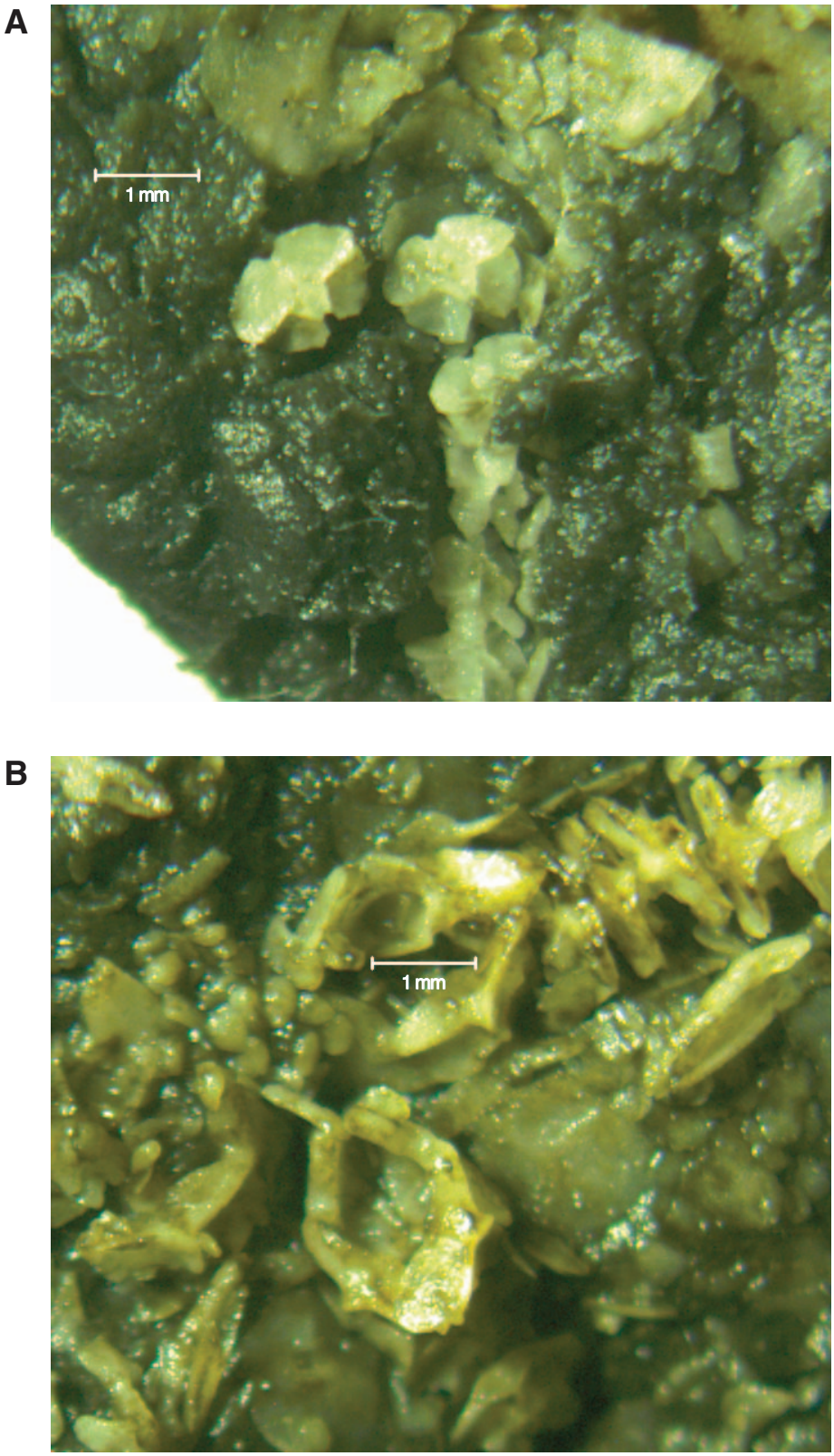

Figure F22. Plots of paleomagnetic measurements from archive halves, Hole U1357A. Data from intervals of disturbed or missing intervals (void spaces) have been removed. Dashed blue lines = core top depths. **A.** Natural remanent magnetization. (**Continued on next page.**)

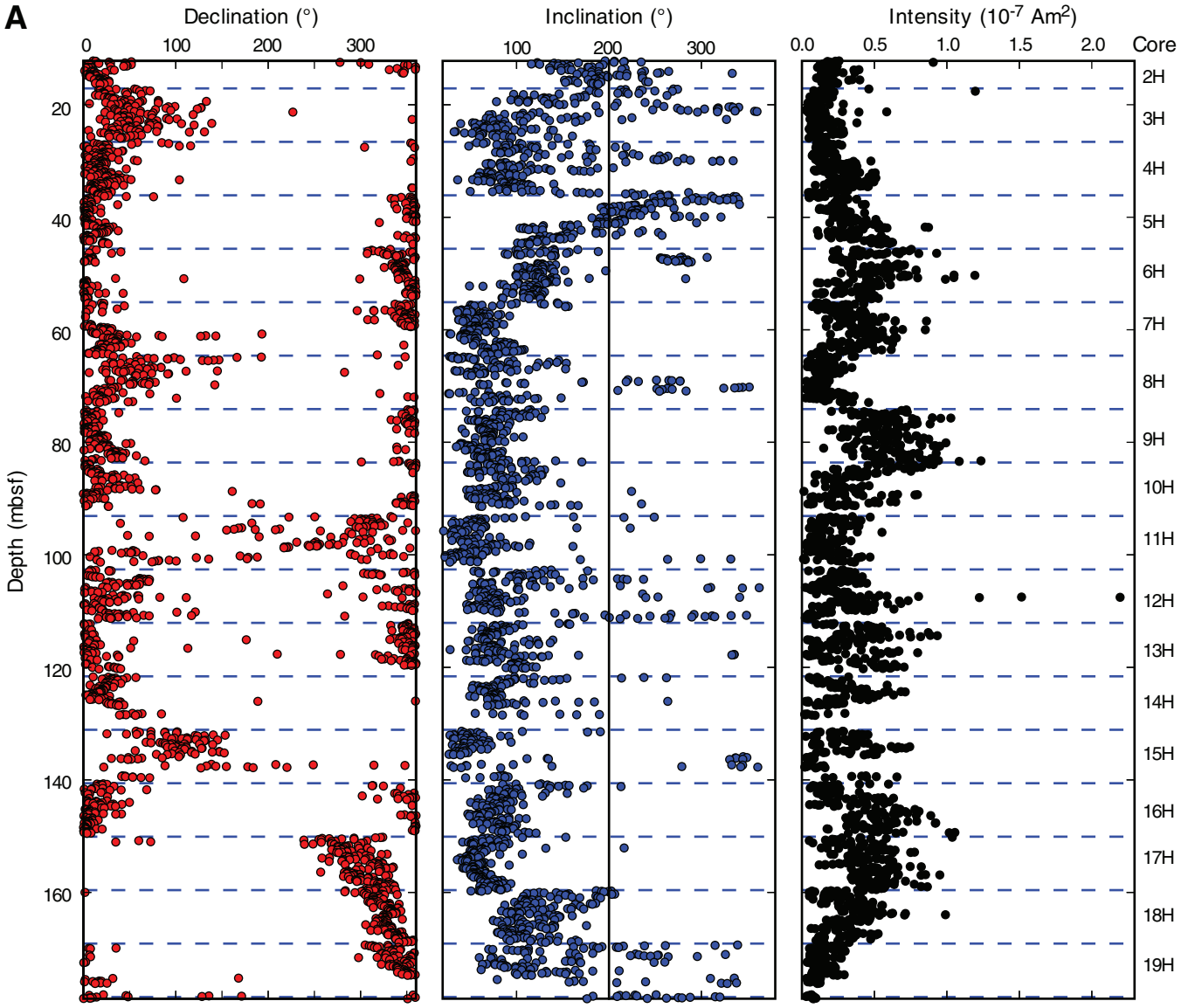

Figure F22 (continued). B. Measurement after demagnetization to 20 mT.

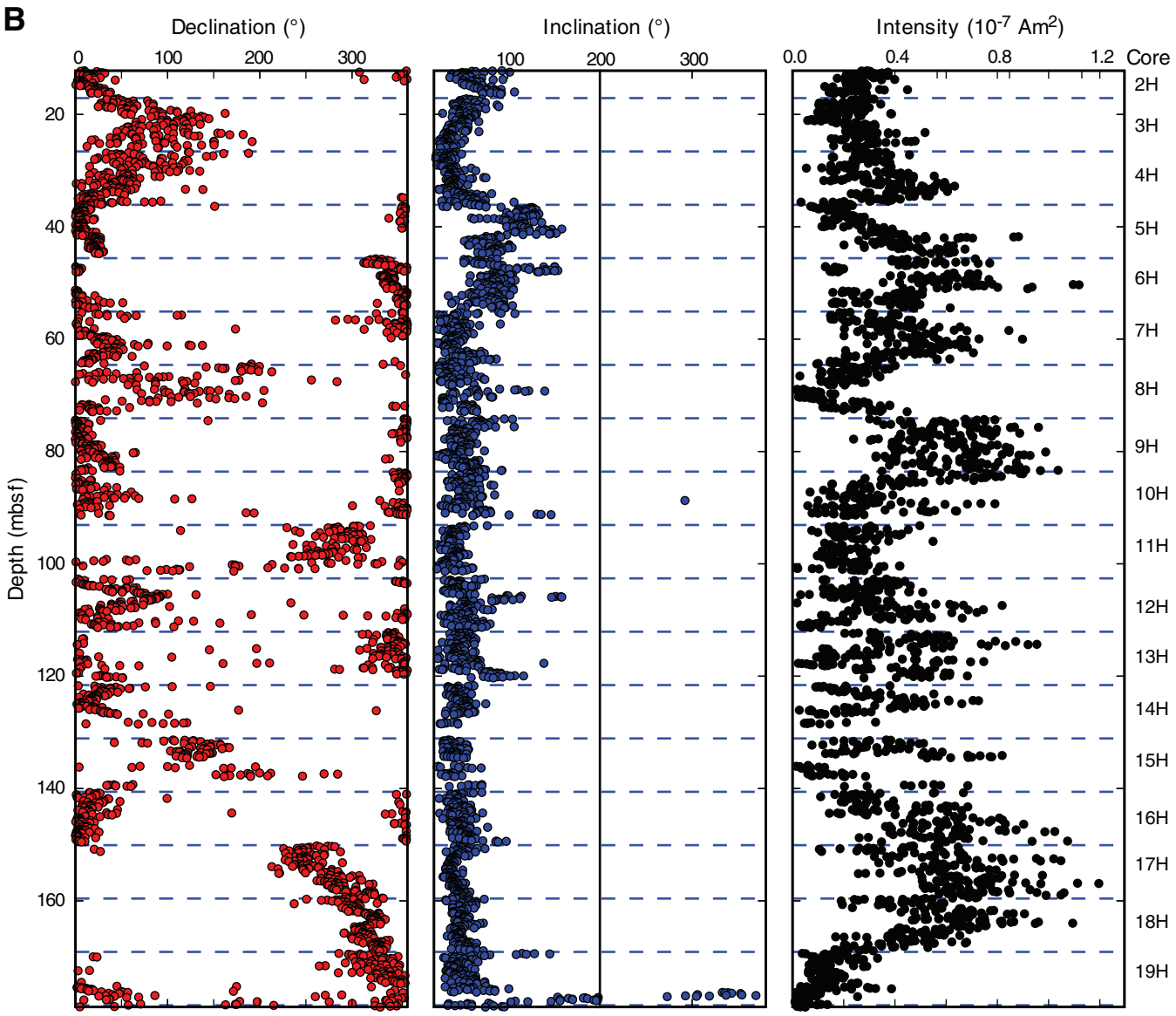

Figure F23. Equal area projections of core top directions, Hole U1357A. Open circles = upper hemisphere, solid circles = lower hemisphere. The *x*-direction is the sample coordinate system, pointing toward the double lines on the core liner. Down and up are geographic, assuming the core was taken vertically. **A.** Natural remanent magnetization directions. **B.** Directions after demagnetization to 20 mT.

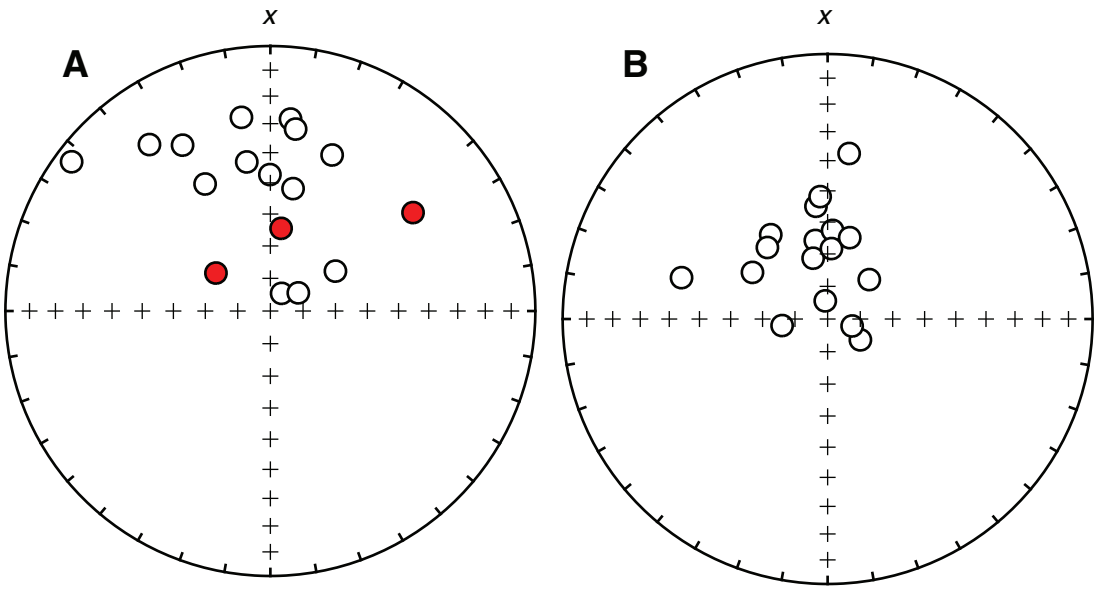

Figure F24. Diagram detailing the effect of coring disturbance on vertically upward–directed magnetizations.

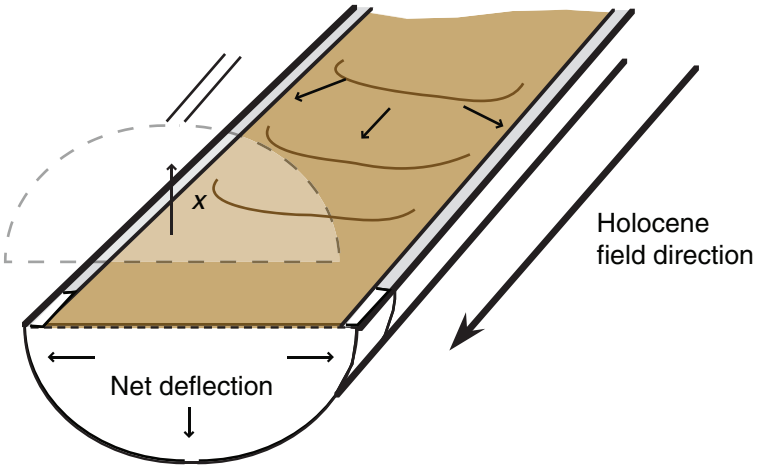

Figure F25. A. Plot of declinations from Figure F22B after rotation of each core top to coincide with the last declination from the previous core. The first core top was rotated to 45°. Tie points to CALS7k.2 model shown in B are numbered as in Table T5 and Figure F26. **B.** Declinations predicted for the location of Site U1357 from the CALS7k.2 secular variation model (Korte and Constable, 2005). Note difference in scale between A and B. **C.** Observed inclinations after demagnetization at 20 mT (Fig. F22B). **D.** Predicted inclinations from the CALS7k.2 model.

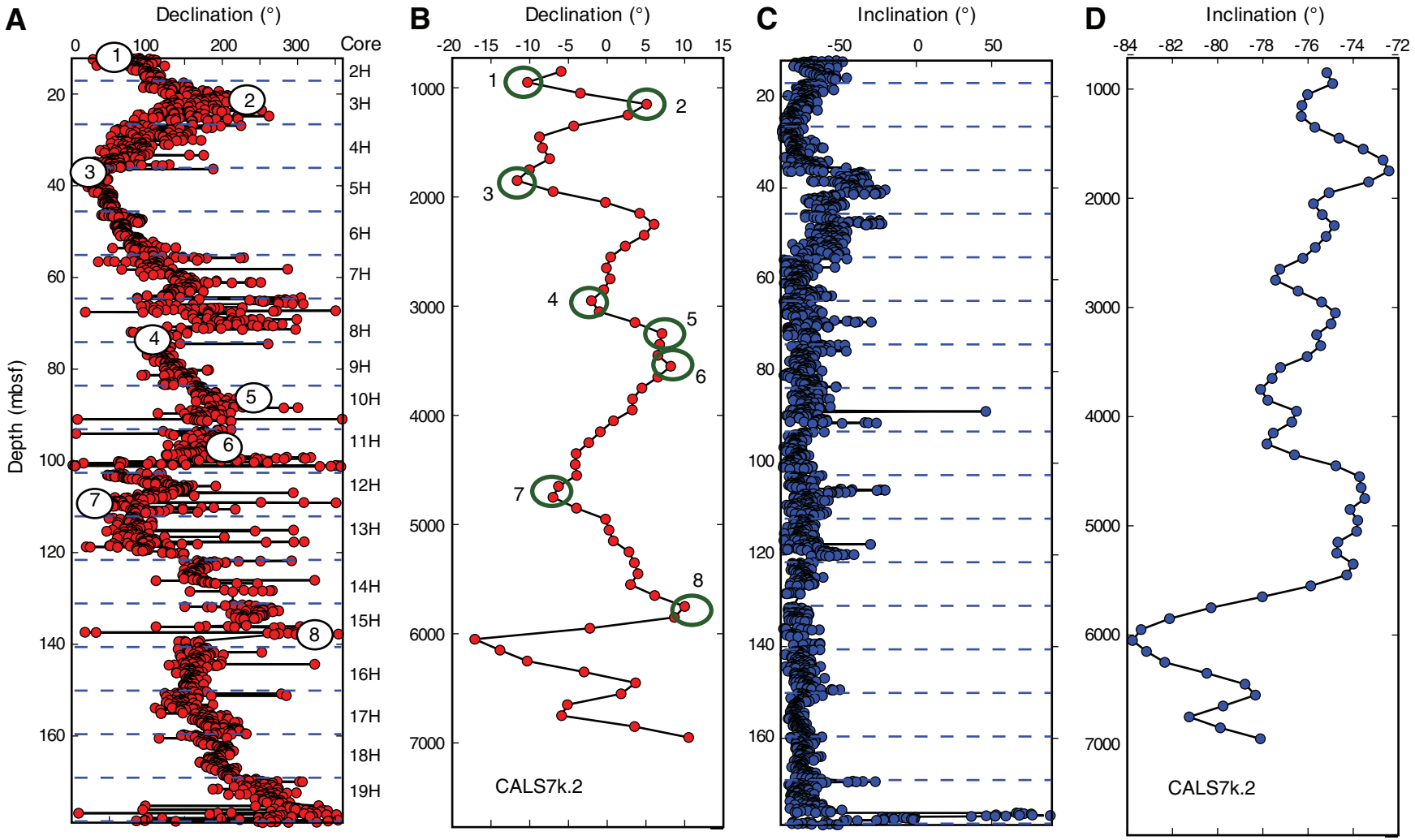

Figure F26. Age-depth model for Site U1357 using tie points identified in Figure F25 and Table T5.

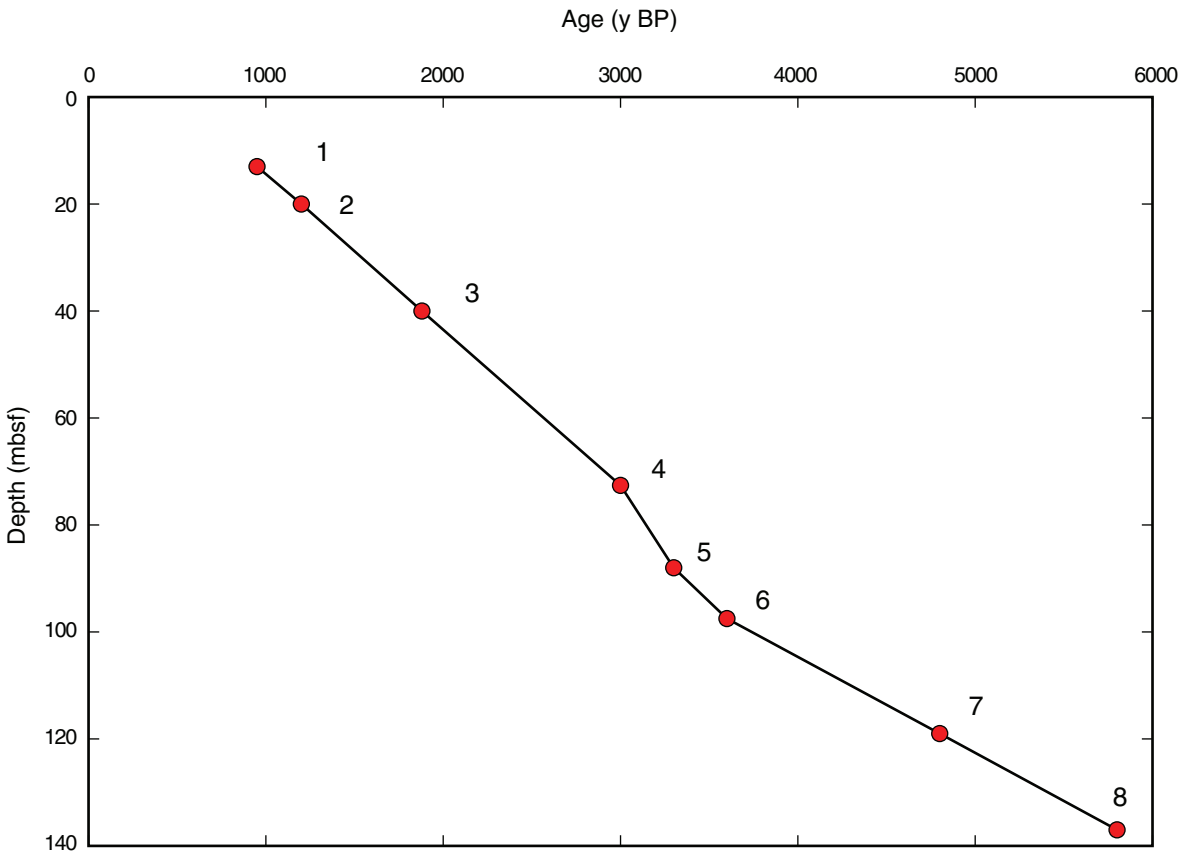

Figure F27. Magnetization plots, Hole U1357A. **A.** Saturation isothermal remanent magnetization (sIRM) vs. mass-normalized magnetic susceptibility. **B.** sIRM vs. anhysteretic remanent magnetization (ARM).

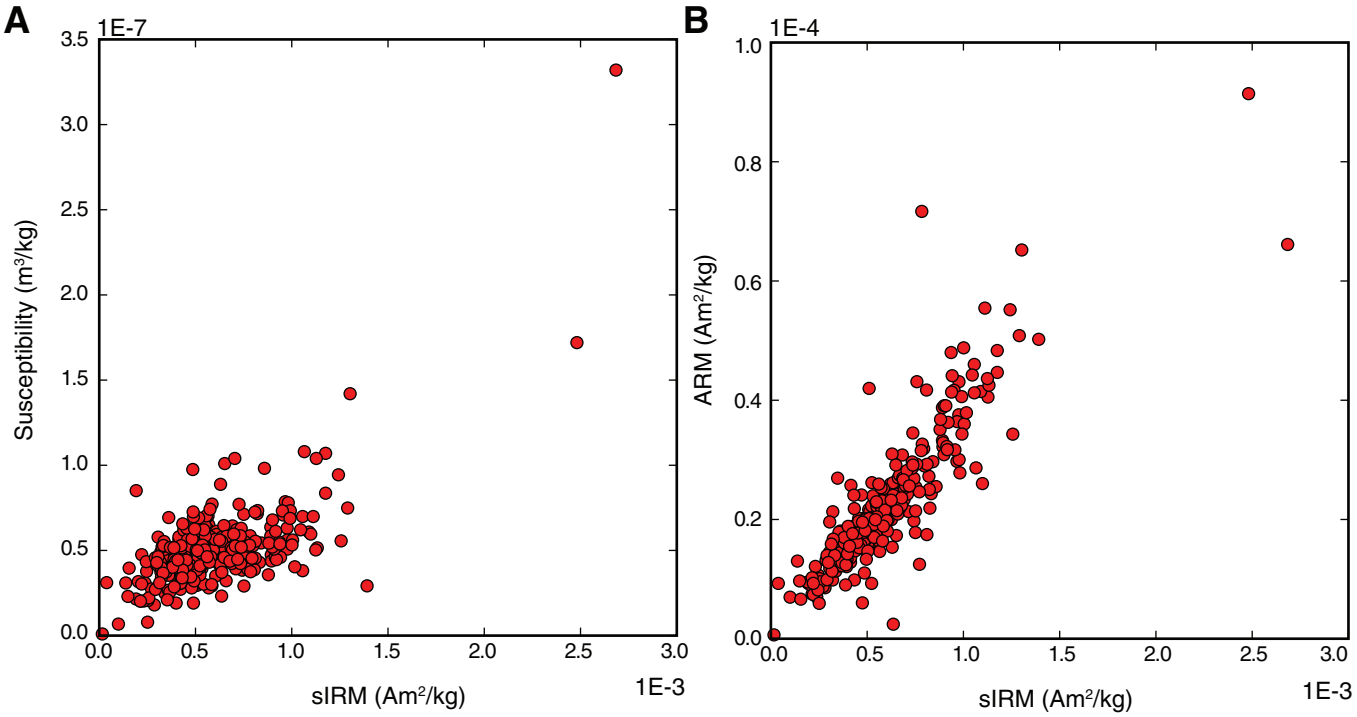

Figure F28. Plots of various bulk properties, Hole U1357A. **A.** Saturation isothermal remanent magnetization (sIRM). **B.** Density-corrected natural gamma radiation (NGR). **C.** Mass-normalized susceptibility.

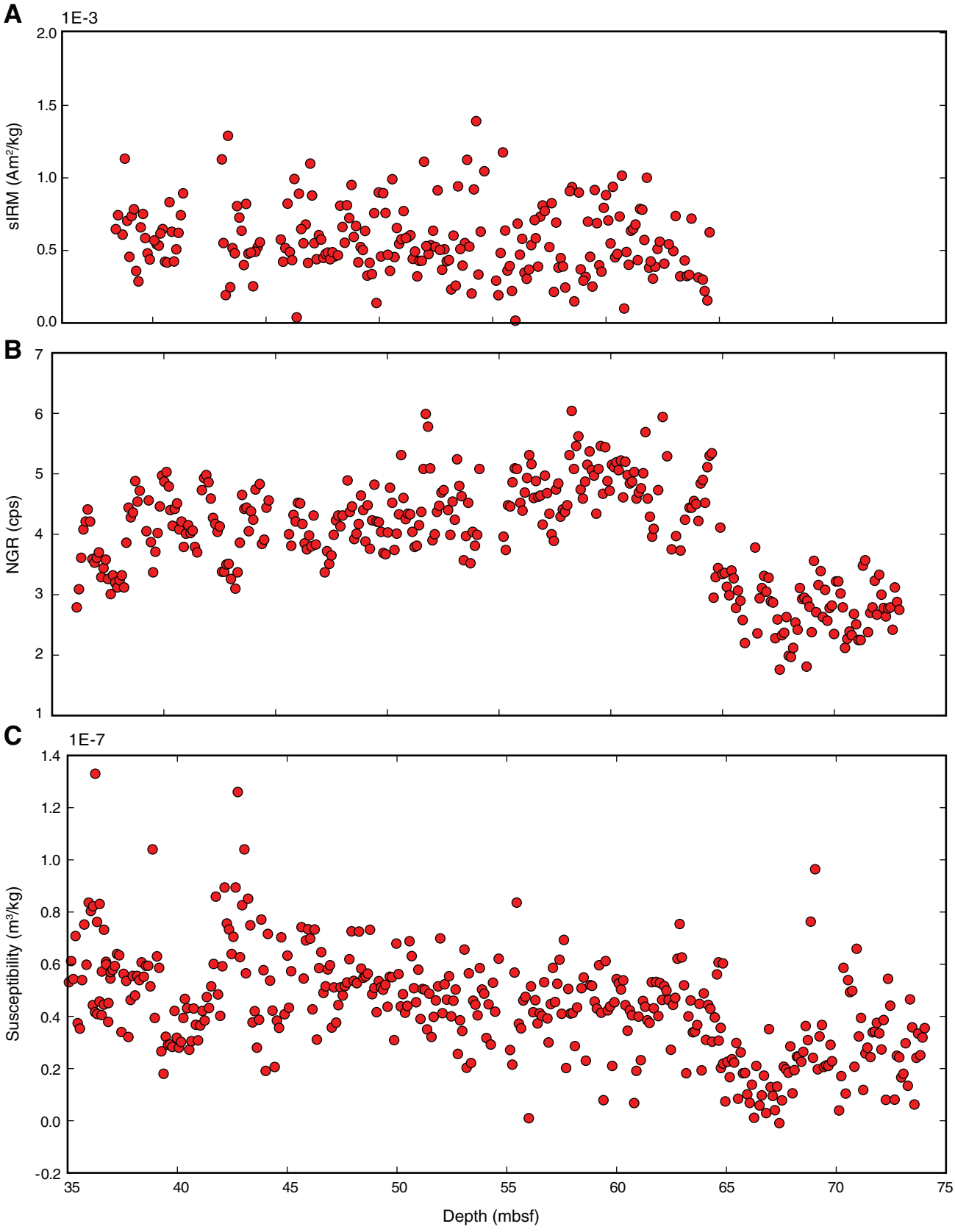

Figure F29. Plot of methane concentrations, Hole U1357A.

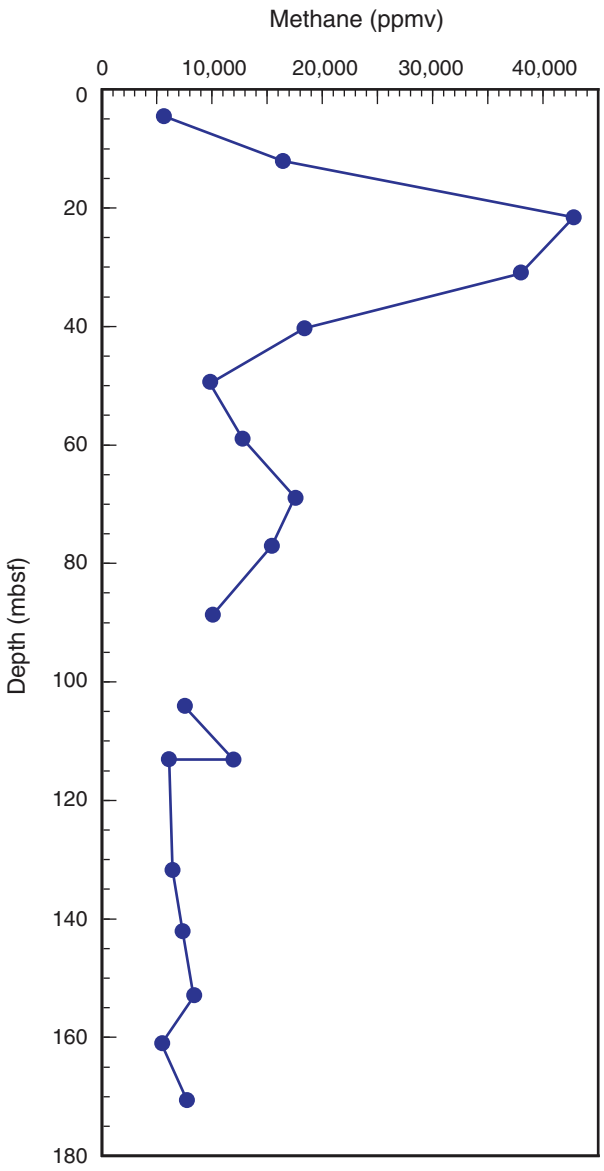

Figure F30. Plot of calcium carbonate data, Hole U1357A.

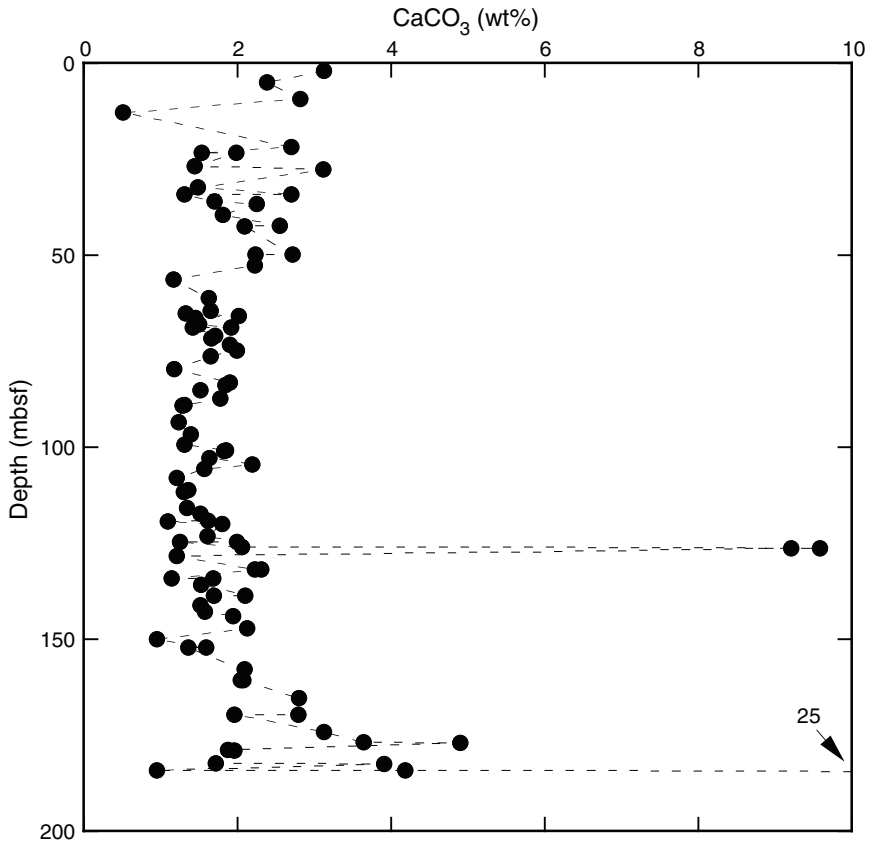

Figure F31. Plots of carbon, nitrogen, and sulfur contents, Hole U1357A. TOC = total organic carbon.

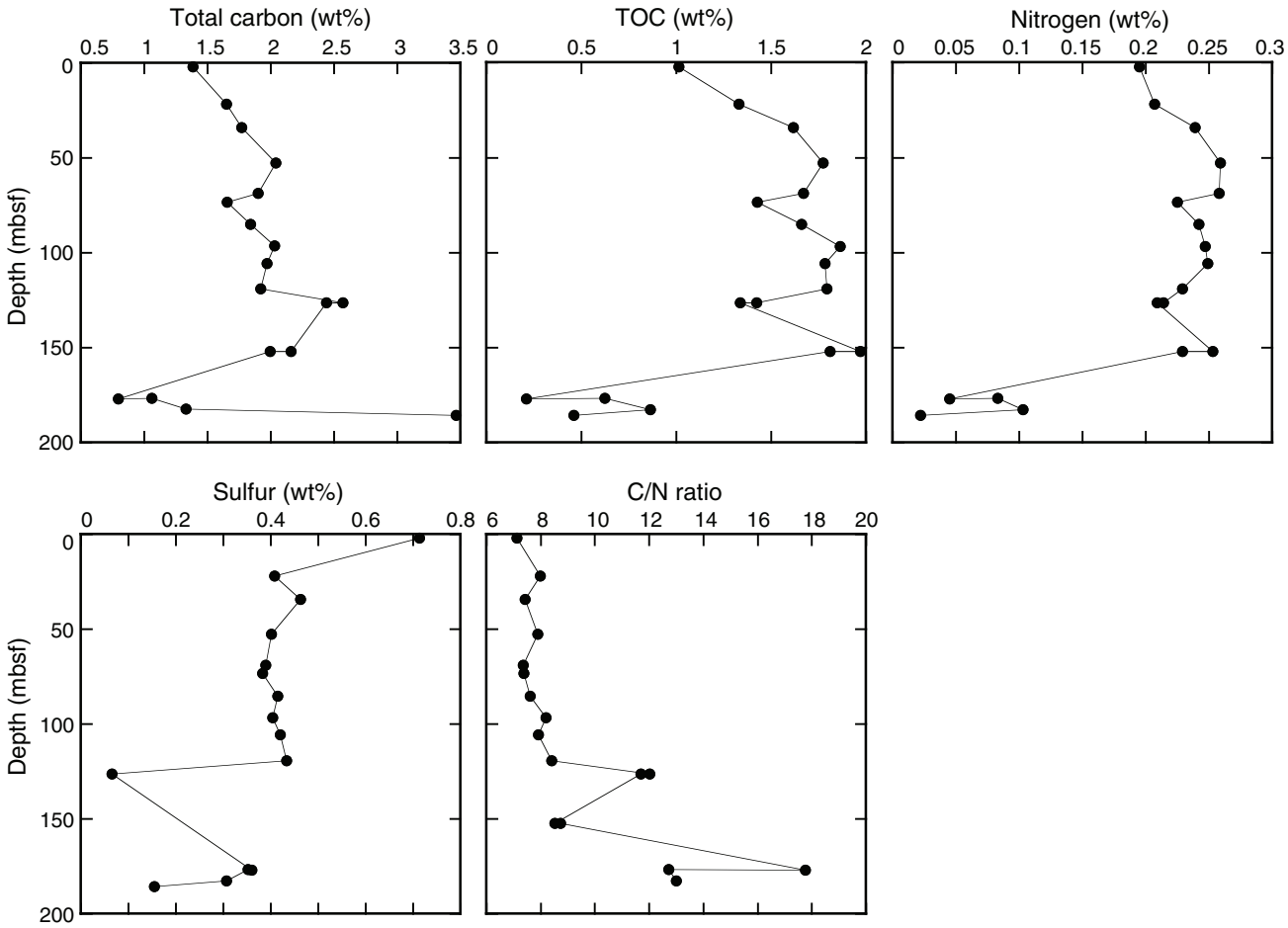

Figure F32. Plots of bulk geochemical data, Hole U1357A.

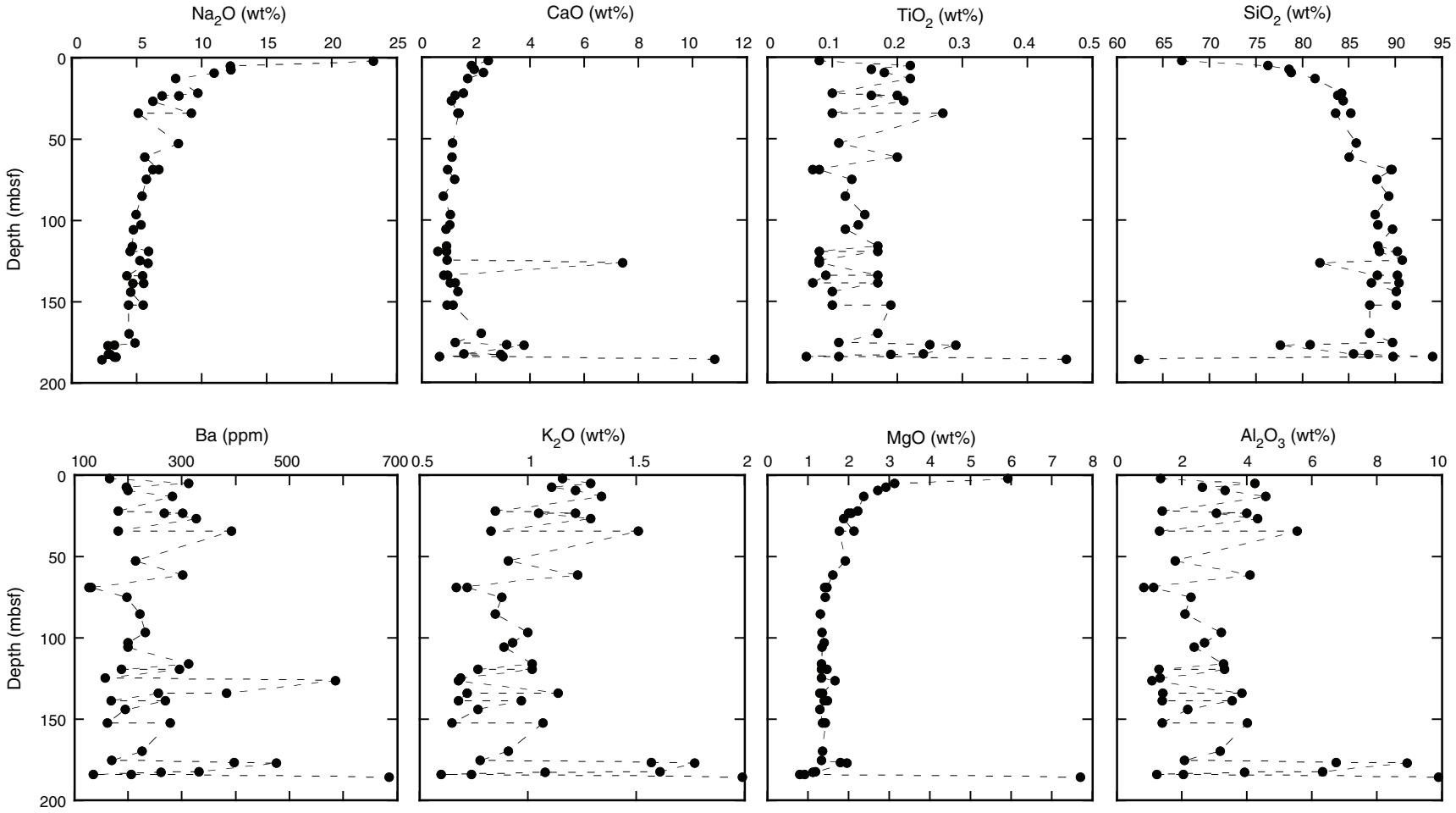

Figure F33. Microbiology and pore water sampling strategy (high-resolution sampling within the top 20 m), Hole U1357C.

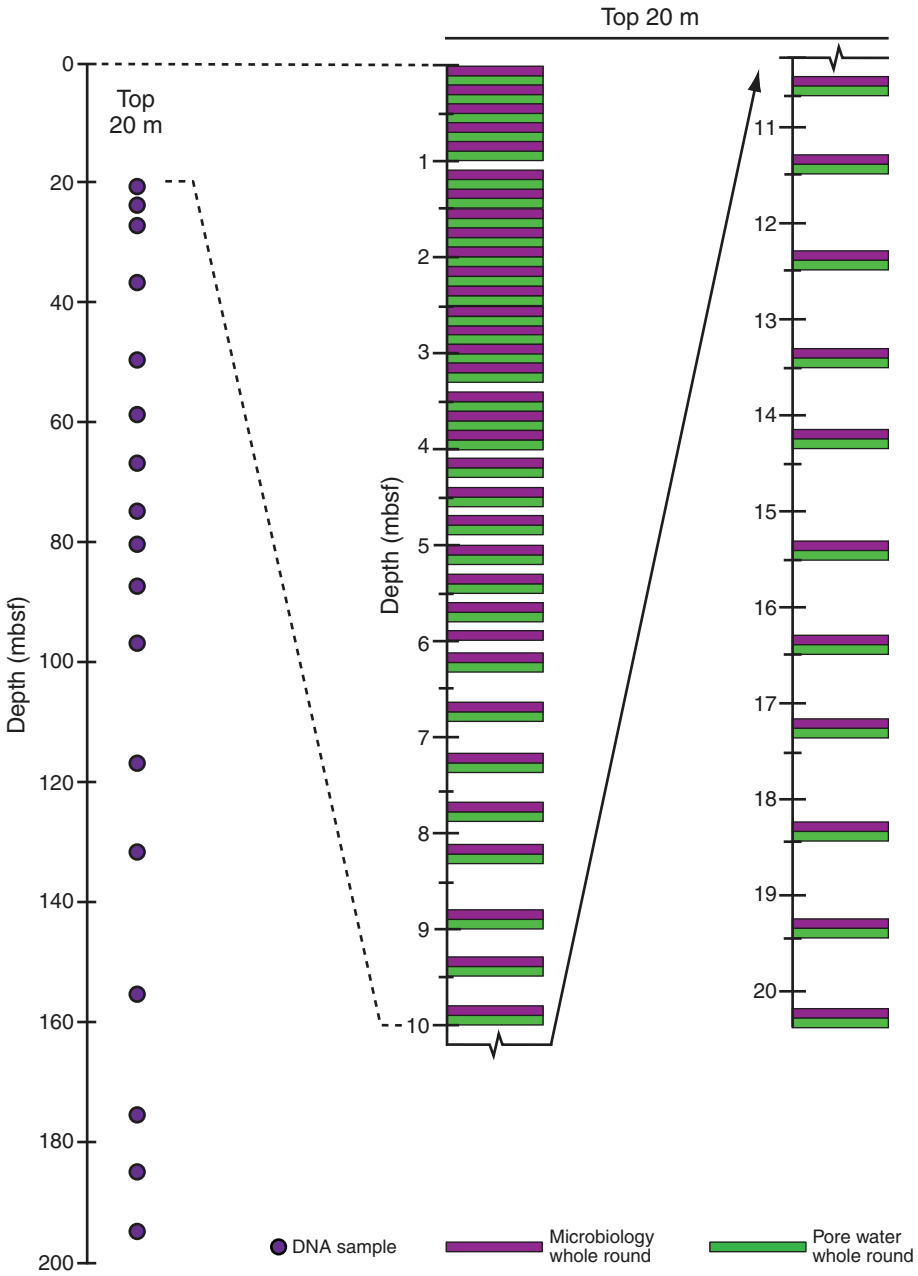

Figure F34. Interstitial water profiles for pH, salinity, chloride, and sodium, Hole U1357C. Shaded intervals = levels in the core where likely seawater infiltration occurred, based on elevated SO_4^{2-} concentrations.

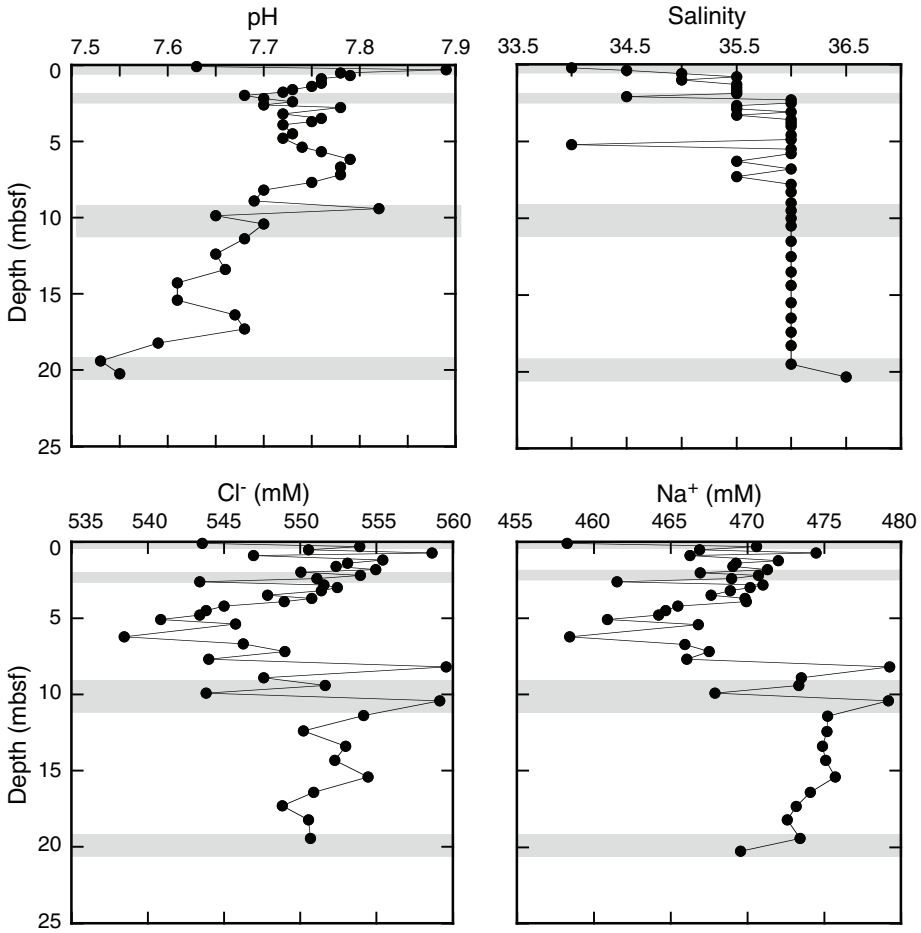

Figure F35. Interstitial water profiles for sulfate, ammonium, alkalinity, dissolved inorganic carbon (DIC; triangles), and phosphate, Hole U1357C. Shaded intervals = levels in the core where likely seawater infiltration occurred, based on elevated SO_4^{2-} concentrations.

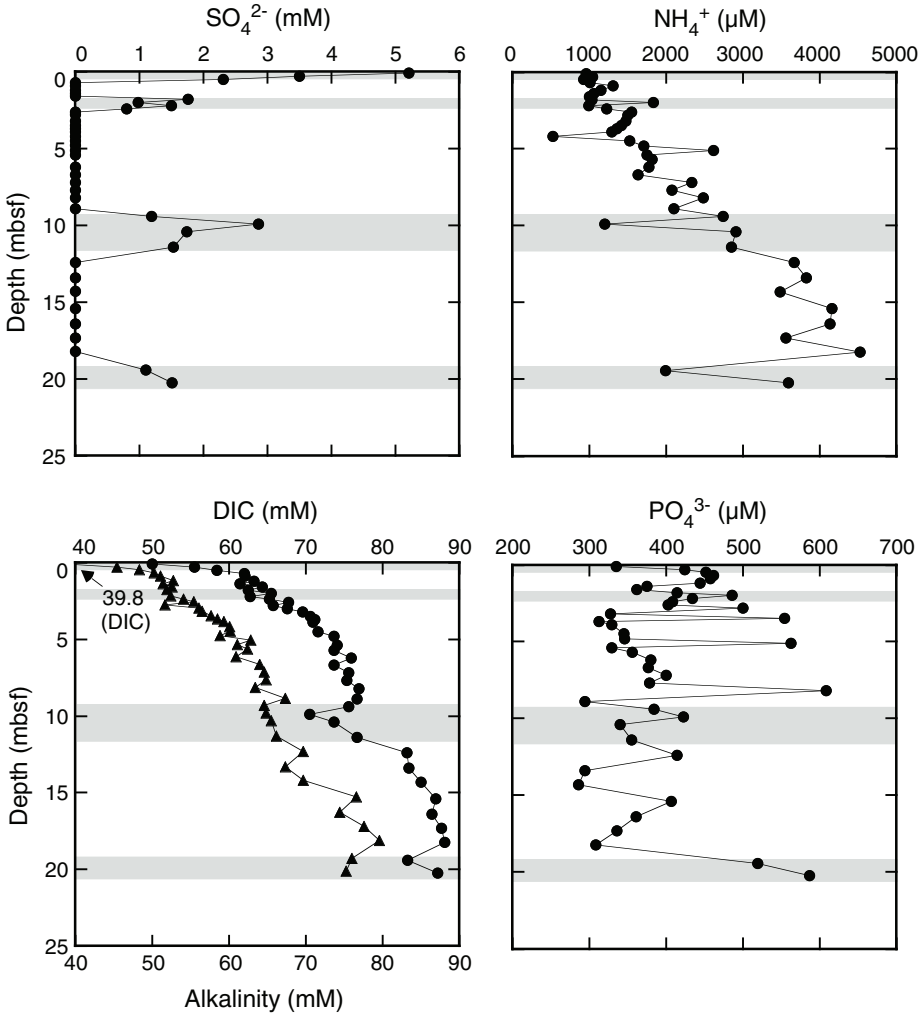

Figure F36. Interstitial water profiles for magnesium and calcium, Hole U1357C. Shaded intervals = levels in the core where likely seawater infiltration occurred, based on elevated SO_4^{2-} concentrations.

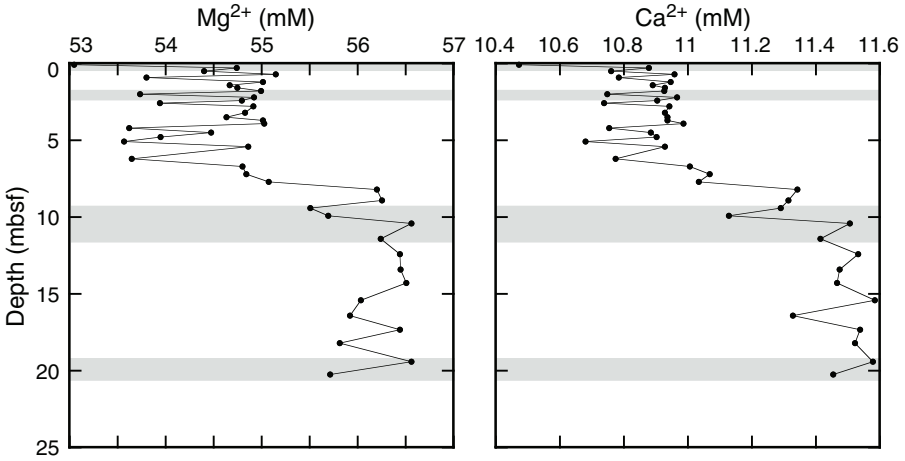

Figure F37. Interstitial water profiles for potassium, strontium, silica, boron, barium, and phosphorus, Hole U1357C. Shaded intervals = levels in the core where likely seawater infiltration occurred, based on elevated SO_4^{2-} concentrations.

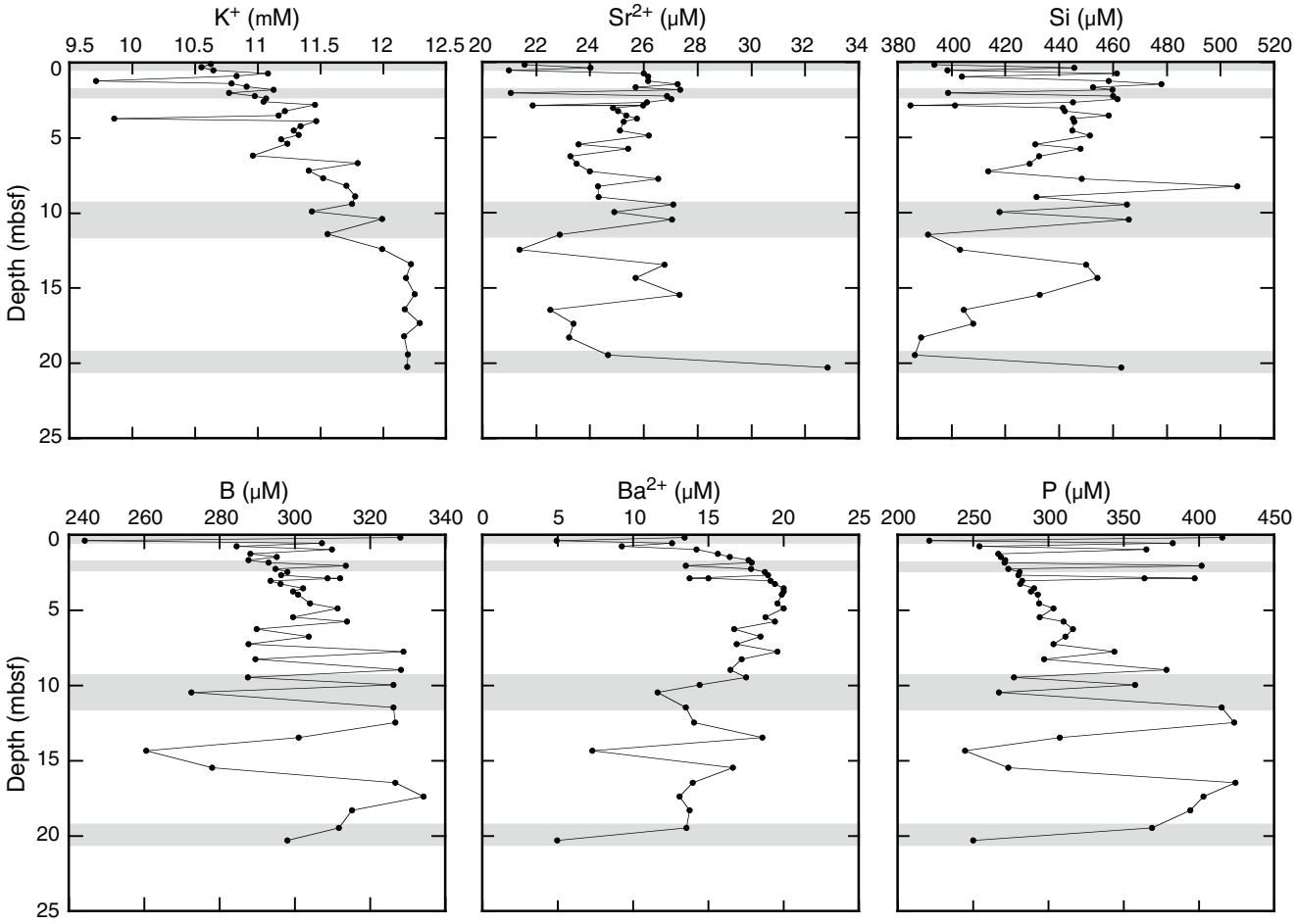

Figure F38. Gamma ray attenuation (GRA) bulk density data, Site U1357. Data offset: Hole U1357B = 0.5 g/cm^3, Hole U1357C = 1 g/cm^3.

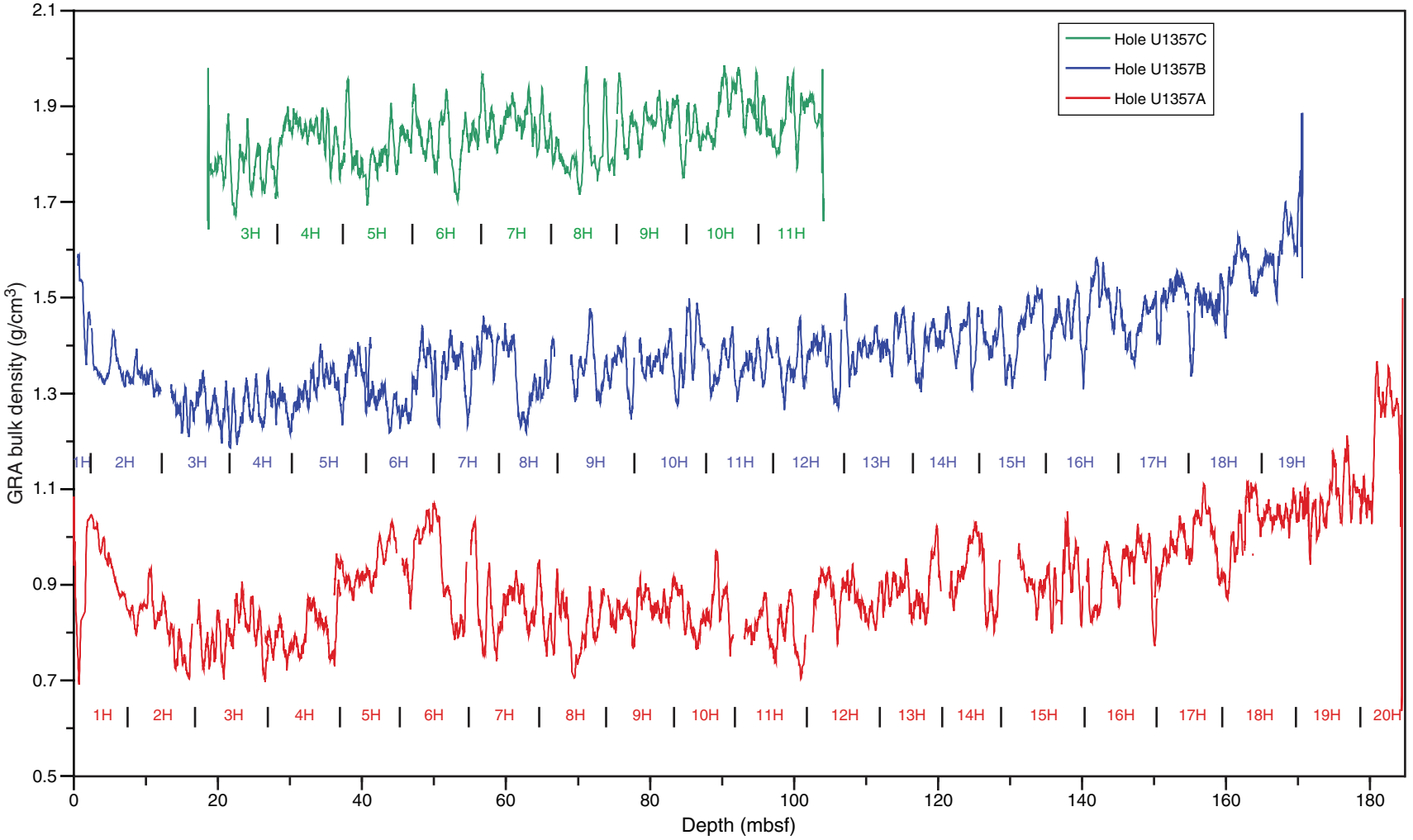

Figure F39. Plot of gamma ray attenuation (GRA) bulk density and bulk density from moisture and density (MAD) discrete measurements, Site U1357.

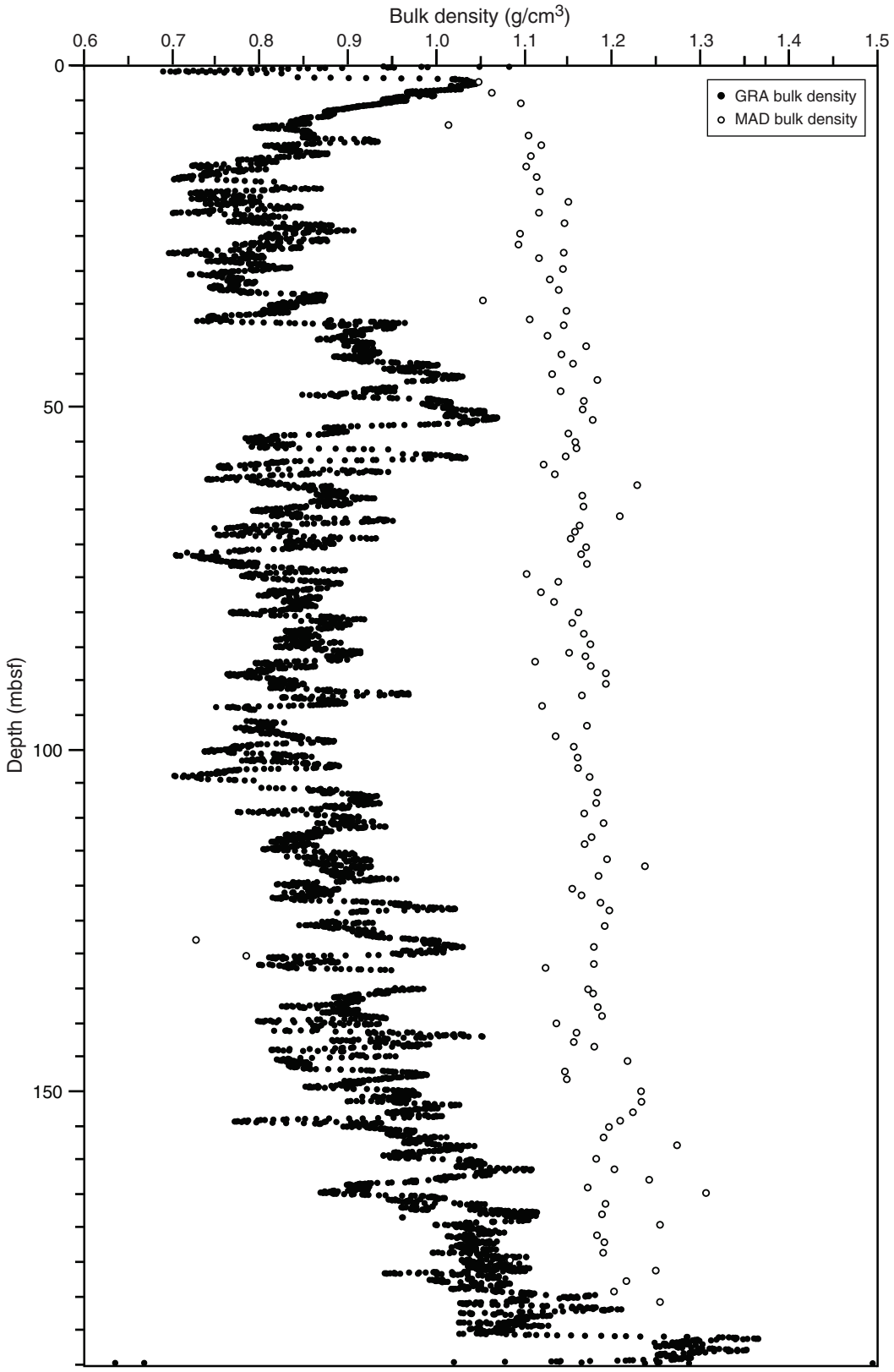

Figure F40. Plots of grain density and porosity from discrete measurements, Site U1357.

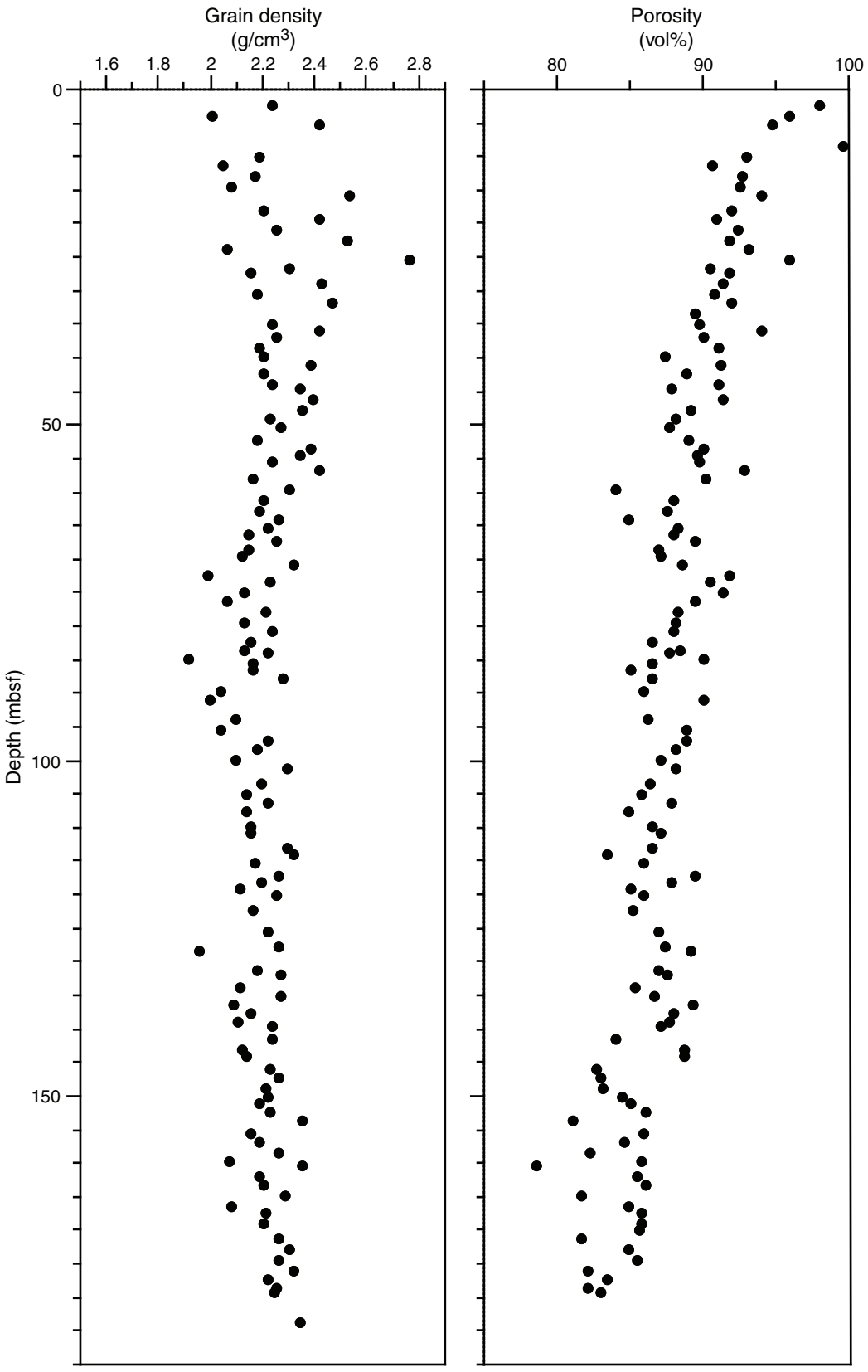

Figure F41. Plots of wet bulk and dry density from discrete measurements, Site U1357.

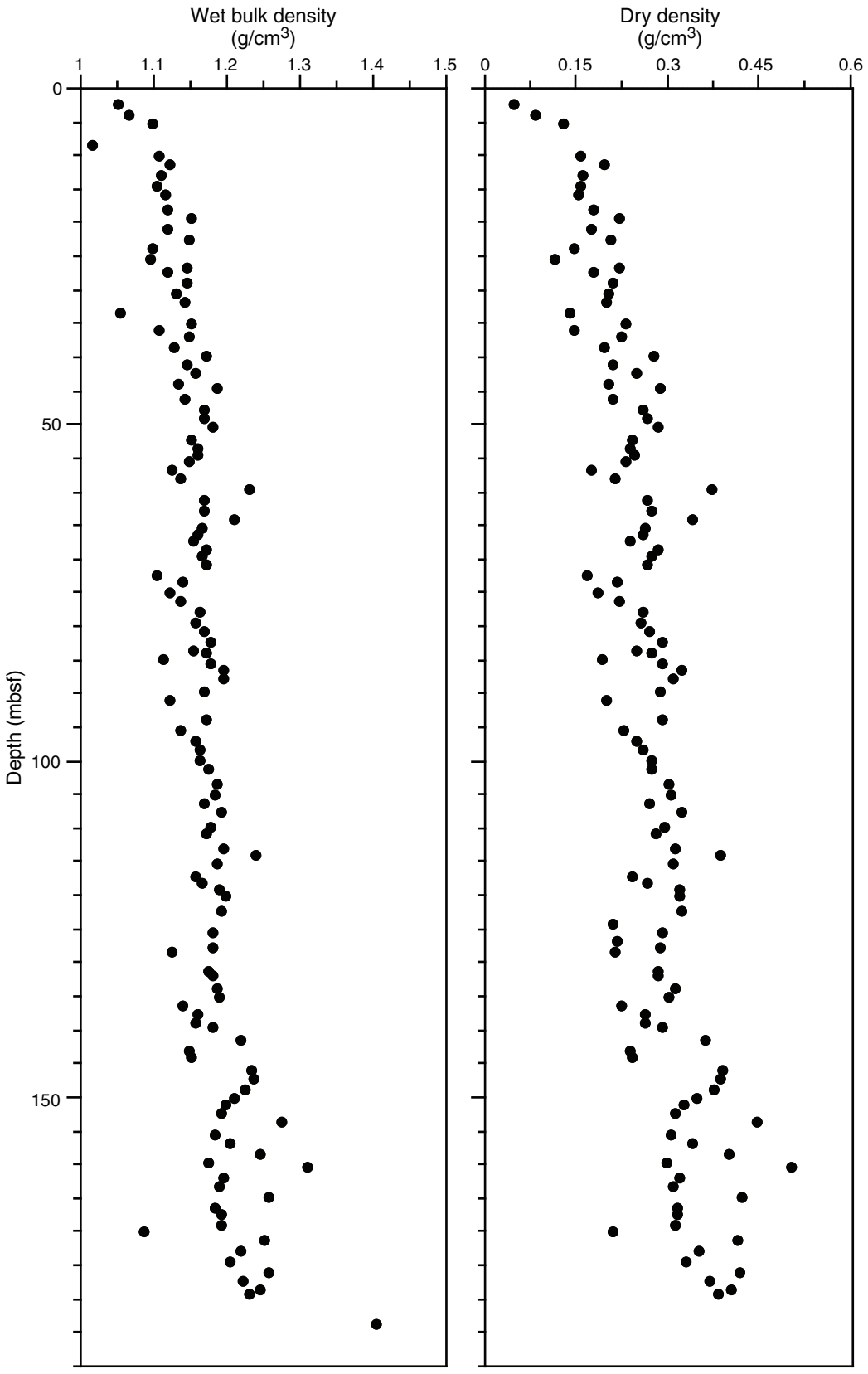

Figure F42. Plots of relative moisture content and void ratio from discrete measurements, Site U1357.

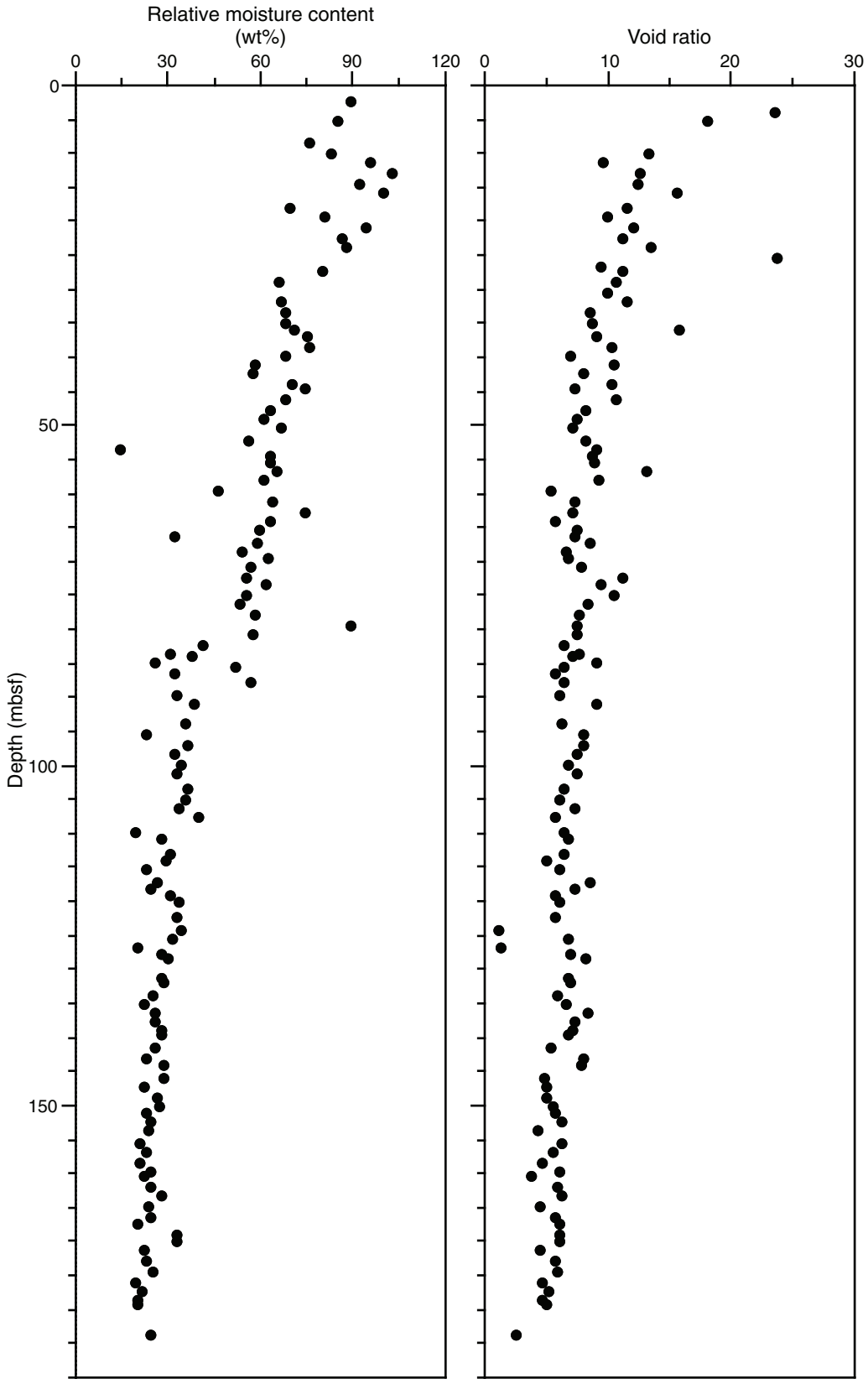

Figure F43. Gamma ray attenuation (GRA) bulk density data, Site U1357. Data offset: Hole U1357B = 0.5 g/cm³, Hole U1357C = 1 g/cm³. **A.** 0–100 mbsf. (**Continued on next page.**)

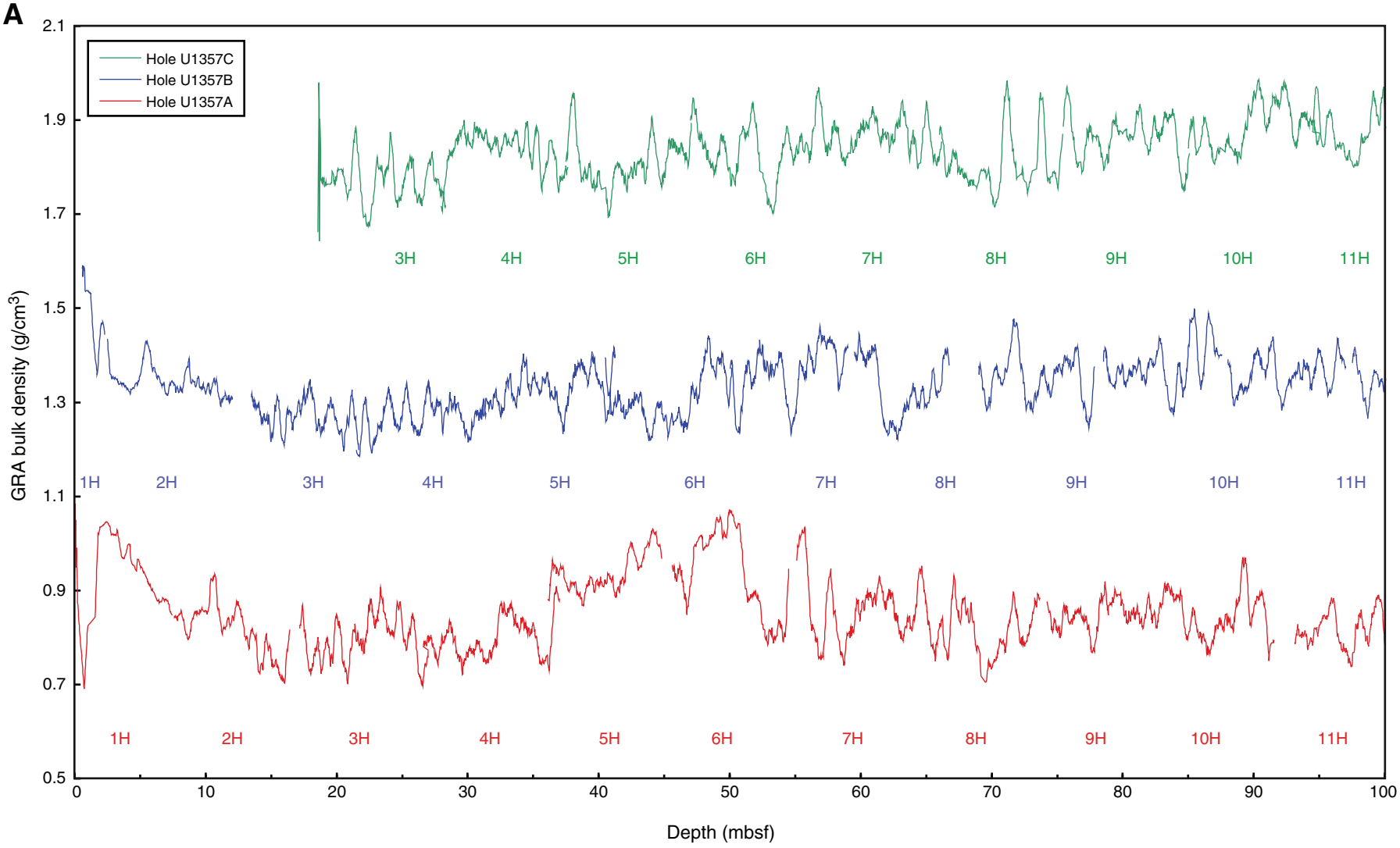

Figure F43 (continued). B. 100–200 mbsf.

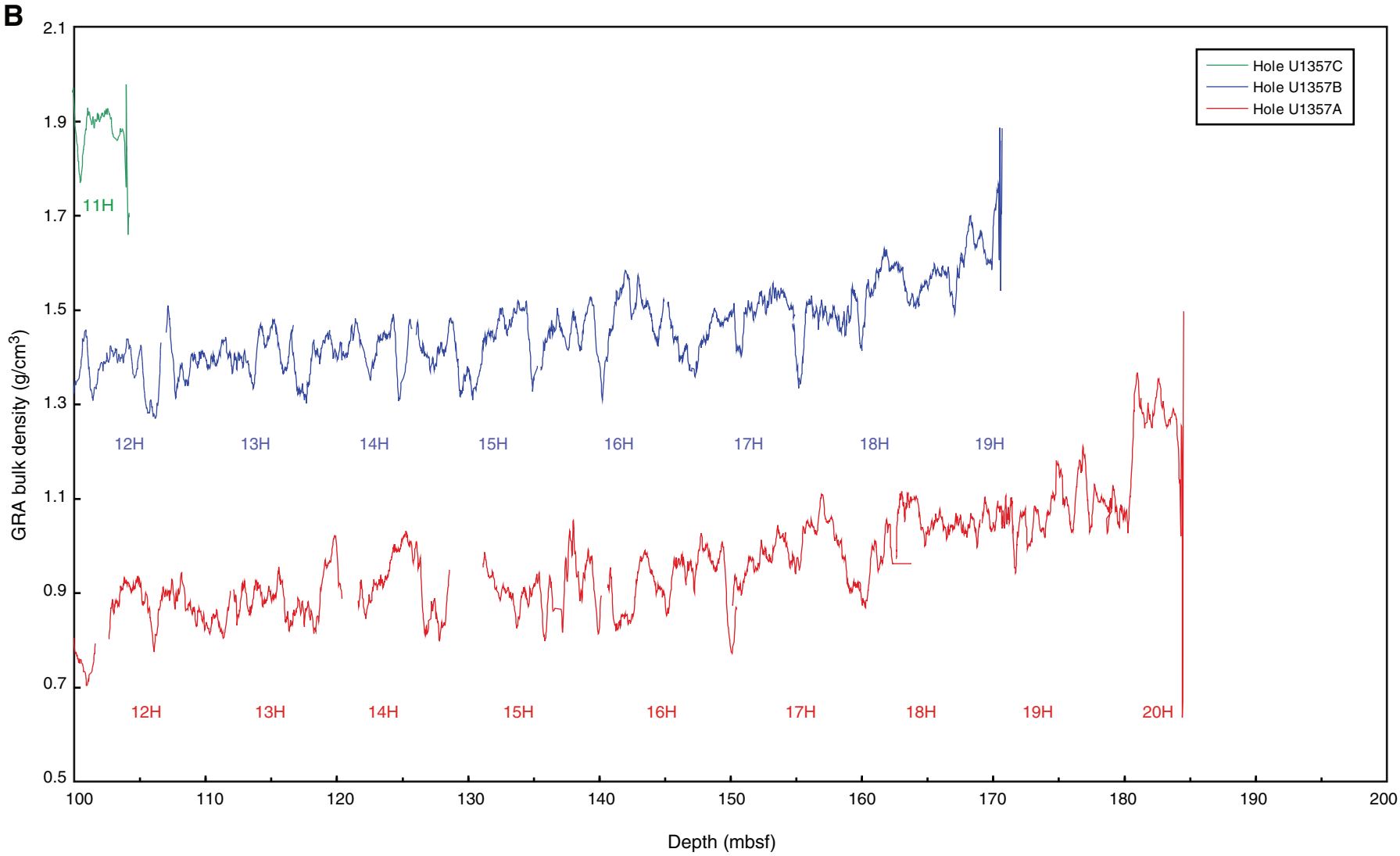

Figure F44. Natural gamma radiation (NGR) and magnetic susceptibility data, Site U1357. The sudden "drop" in NGR counts (aligned at 65 mcd) has been used to correlate between these cores and to create a preliminary joint depth scale for ~41–74 mcd. Note that the high-resolving mass magnetic susceptibility data measured by the Kappabridge (see **"Paleomagnetism"**) for Hole U1357A corroborate the sudden drop observed in the NGR counts. Data offset: Hole U1357B = 2.5 cps, Hole U1357C = 5 cps.

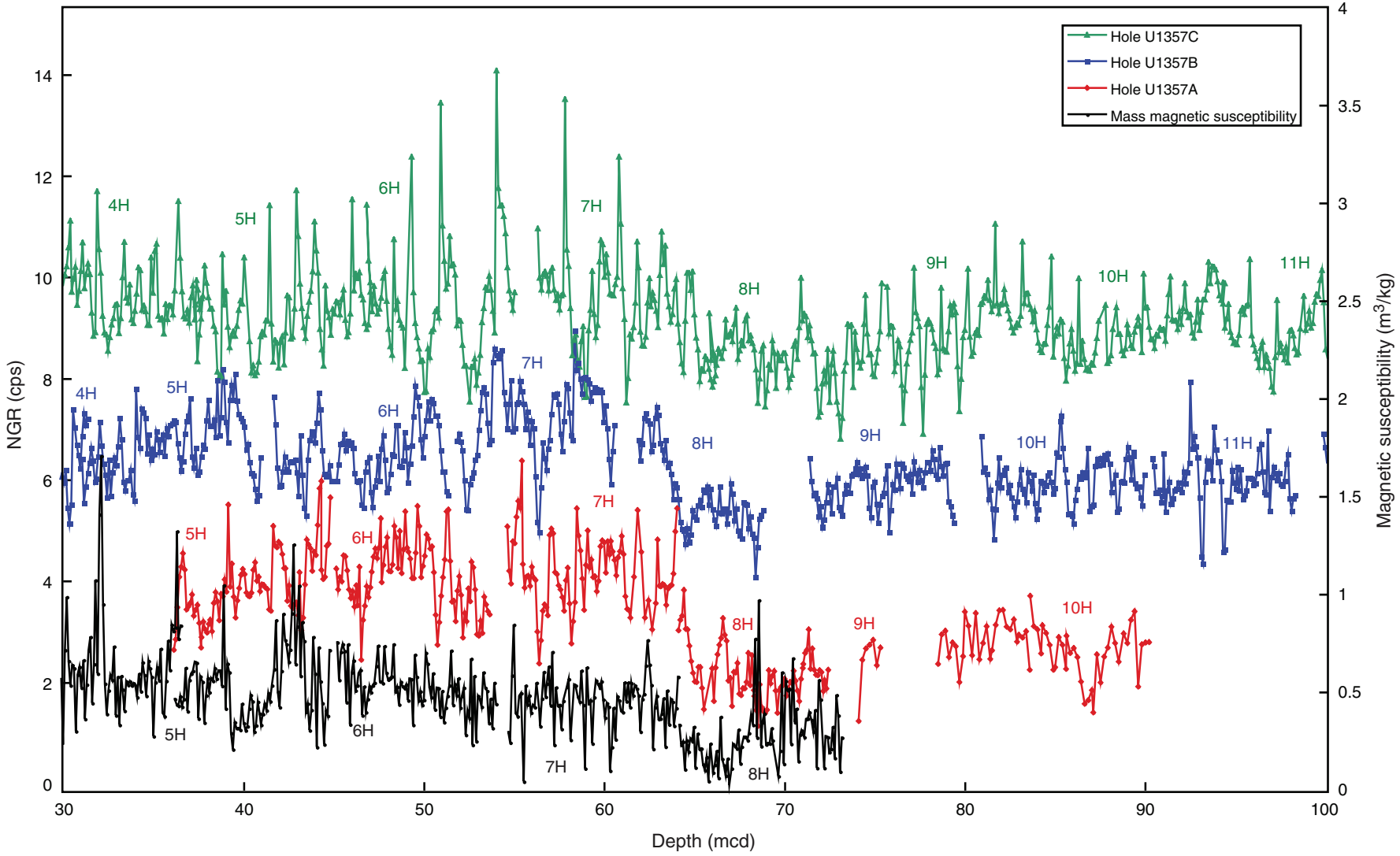

Table T1. Coring summary, Site U1357. (See table notes.) (Continued on next page.)

Site U1357
Time on site (h): 63.4 (0800 h, 3 February–0900 h, 6 February 2010)

Hole U1357A
Latitude: 66°24.7991′S
Longitude: 140°25.5008′E
Time on hole (h): 27.33(0800 h, 3 February–1120 h, 4 February 2010)
Seafloor (drill pipe measurement from rig floor, m DRF): 1025.9
Distance between rig floor and sea level (m): 11.0
Water depth (drill pipe measurement from sea level, m): 1014.9
Total penetration (m DSF): 186.6
Total depth (drill pipe measurement from rig floor, m DRF): 1212.5
Total length of cored section (m): 186.6
Total core recovered (m): 183.87
Core recovery (%): 99
Total number of cores: 21

Hole U1357B
Latitude: 66°24.7990′S
Longitude: 140°25.5705′E
Time on hole (h): 16.33 (1120 h, 4 February–0340 h, 5 February 2010)
Seafloor (drill pipe measurement from rig floor, m DRF): 1028.0
Distance between rig floor and sea level (m): 11.0
Water depth (drill pipe measurement from sea level, m): 1017.0
Total penetration (m DSF): 170.7
Total depth (drill pipe measurement from rig floor, m DRF): 1198.7
Total length of cored section (m): 170.7
Total core recovered (m): 172.44
Core recovery (%): 101
Total number of cores: 19

Hole U1357C
Latitude: 66°24.8013′S
Longitude: 140°25.4651′E
Time on hole (h): 19.75 (0340 h, 5 February–0900 h, 6 February 2010)
Seafloor (drill pipe measurement from rig floor, m DRF): 1027.7
Distance between rig floor and sea level (m): 11.0
Water depth (drill pipe measurement from sea level, m): 1016.7
Total penetration (m DSF): 103.8
Total depth (drill pipe measurement from rig floor, m DRF): 1131.5
Total length of cored section (m): 103.8
Total core recovered (m): 110.71
Core recovery (%): 107
Total number of cores: 11

			Depth DSF-B (m)			Depth CSF-A (m)			
Core	Date (2010)	Local time (h)	Top of cored interval	Bottom of cored interval	Interval advanced (m)	Top of cored interval	Bottom of cored interval	Length of core recovered (m)	Recovery (%)
318-U1357A-									
1H	3 Feb	1450	0.0	7.6	7.6	0.00	7.64	7.64	101
2H	3 Feb	1540	7.6	17.1	9.5	7.60	16.65	9.05	95
3H	3 Feb	1615	17.1	26.6	9.5	17.10	27.35	10.25	108
4H	3 Feb	1650	26.6	36.1	9.5	26.60	37.02	10.42	110
5H	3 Feb	1725	36.1	45.6	9.5	36.10	45.28	9.18	97
6H	3 Feb	1805	45.6	55.1	9.5	45.60	54.78	9.18	97
7H	3 Feb	1840	55.1	64.6	9.5	55.10	64.95	9.85	104
8H	3 Feb	1910	64.6	74.1	9.5	64.60	74.08	9.48	100
9H	3 Feb	1940	74.1	83.6	9.5	74.10	83.64	9.54	100
10H	3 Feb	2005	83.6	93.1	9.5	83.60	92.03	8.43	89
11H	3 Feb	2040	93.1	102.6	9.5	93.10	101.93	8.83	93
12H	3 Feb	2110	102.6	112.1	9.5	102.60	112.15	9.55	101
13H	3 Feb	2140	112.1	121.6	9.5	112.10	120.62	8.52	90
14H	3 Feb	2205	121.6	131.1	9.5	121.60	129.04	7.44	78
15H	3 Feb	2235	131.1	140.6	9.5	131.10	140.35	9.25	97
16H	3 Feb	2310	140.6	150.1	9.5	140.60	150.76	10.16	107
17H	3 Feb	2335	150.1	159.6	9.5	150.10	160.22	10.12	107
18H	4 Feb	0010	159.6	169.1	9.5	159.60	169.43	9.83	103
19H	4 Feb	0040	169.1	178.6	9.5	169.10	179.29	10.19	107
20H	4 Feb	0645	178.6	185.6	7.0	178.60	185.45	6.85	98
21X	4 Feb	0920	185.6	186.6	1.0	185.60	185.71	0.11	11
				Cored totals:	186.6			183.87	99
				Total interval cored:	186.6				

Table T1 (continued).

Core	Date (2010)	Local time (h)	Depth DSF-B (m) Top of cored interval	Depth DSF-B (m) Bottom of cored interval	Interval advanced (m)	Depth CSF-A (m) Top of cored interval	Depth CSF-A (m) Bottom of cored interval	Length of core recovered (m)	Recovery (%)
318-U1357B-									
1H	4 Feb	1410	0.0	2.5	2.5	0.00	2.49	2.49	100
2H	4 Feb	1625	2.5	12.0	9.5	2.50	12.29	9.79	103
3H	4 Feb	1700	12.0	21.5	9.5	12.00	22.28	10.28	108
4H	4 Feb	1740	21.5	31.0	9.5	21.50	31.70	10.20	107
5H	4 Feb	1820	31.0	40.5	9.5	31.00	41.31	10.31	109
6H	4 Feb	1850	40.5	50.0	9.5	40.50	50.43	9.93	105
7H	4 Feb	1920	50.0	59.5	9.5	50.00	59.08	9.08	96
8H	4 Feb	1950	59.5	69.0	9.5	59.50	66.77	7.27	77
9H	4 Feb	2030	69.0	78.5	9.5	69.00	78.09	9.09	96
10H	4 Feb	2100	78.5	88.0	9.5	78.50	87.86	9.36	99
11H	4 Feb	2130	88.0	97.5	9.5	88.00	97.33	9.33	98
12H	4 Feb	2150	97.5	107.0	9.5	97.50	106.82	9.32	98
13H	4 Feb	2220	107.0	116.5	9.5	107.00	117.02	10.02	105
14H	4 Feb	2250	116.5	126.0	9.5	116.50	126.05	9.55	101
15H	4 Feb	2320	126.0	135.5	9.5	126.00	135.51	9.51	100
16H	4 Feb	2350	135.5	145.0	9.5	135.50	145.18	9.68	102
17H	5 Feb	0035	145.0	154.5	9.5	145.00	155.19	10.19	107
18H	5 Feb	0107	154.5	164.0	9.5	154.50	164.77	10.27	108
19H	5 Feb	0150	164.0	170.7	6.7	164.00	170.77	6.77	101
				Cored totals:	170.7			172.44	101
				Total interval cored:	170.7				
318-U1357C-									
1H	5 Feb	0705	0.0	8.8	8.8	0.00	8.78	8.78	100
2H	5 Feb	0750	8.8	18.3	9.5	8.80	18.82	10.02	105
3H	5 Feb	0815	18.3	27.8	9.5	18.30	28.81	10.51	111
4H	5 Feb	0850	27.8	37.3	9.5	27.80	38.10	10.30	108
5H	5 Feb	0925	37.3	46.8	9.5	37.30	47.50	10.20	107
6H	5 Feb	1000	46.8	56.3	9.5	46.80	56.84	10.04	106
7H	5 Feb	1030	56.3	65.8	9.5	56.30	66.41	10.11	106
8H	5 Feb	1125	65.8	75.3	9.5	65.80	75.87	10.07	106
9H	5 Feb	1205	75.3	84.8	9.5	75.30	85.34	10.04	106
10H	5 Feb	1235	84.8	94.3	9.5	84.80	95.26	10.46	110
11H	5 Feb	1300	94.3	103.8	9.5	94.30	104.48	10.18	107
				Cored totals:	103.8			110.71	107
				Total interval cored:	103.8				

Notes: DRF = drilling depth below rig floor. DSF-A = drilling depth below seafloor determined by tagging seafloor, DSF-B = drilling depth below seafloor determined by mudline core recovery, CSF-A = core depth below seafloor, overlap if long. Local time = UTC + 11 h.

Table T2. Depths of layers or pockets of concentrated fish debris, Hole U1357A.

Core, section, interval (cm)	Depth (mbsf)	
	Top	Bottom
318-U1357A-		
3H-3, 121–121	21.32	21.32
3H-6, 127–128	25.89	25.90
4H-5, 94–94	33.55	33.55
4H-6, 145–145	35.56	35.56
5H-5, 75–75	42.35	42.35
5H-5, 107–107	42.67	42.67
5H-5, 137–137	42.97	42.97
6H-3, 27–27	48.39	48.39
7H-1, 49–49	55.59	55.59
7H-5, 8–8	60.53	60.53
8H-2, 9–9	66.10	66.10
8H-3, 19–19	66.65	66.65
8H-3, 63–63	67.09	67.09
8H-4, 20–20	68.16	68.16
9H-6, 142–142	82.91	82.91
9H-7, 3–3	83.02	83.02
10H-5, 82–82	87.94	87.94
10H-8, 4–4	90.34	90.34
11H-3, 80–80	96.90	96.90
11H-5, 67–67	99.77	99.77
11H-6, 93–93	101.53	101.53
12H-1, 123–123	103.83	103.83
12H-2, 89–89	104.99	104.99
12H-4, 107–108	108.12	108.13
12H-CC, 15–15	112.04	112.04
13H-3, 24–25	114.69	114.70
13H-5, 68–68	117.98	117.98
13H-6, 89–90	119.14	119.15
14H-1, 104–105	122.64	122.65
14H-4, 63–64	126.47	126.48
14H-6, 34–36	128.42	128.44
15H-1, 3–3	131.13	131.13
15H-1, 23–25	131.33	131.35
15H-2, 23–25	131.94	131.96
15H-2, 132–133	133.03	133.04
15H-3, 137–137	134.58	134.58
16H-1, 45–45	141.05	141.05
16H-2, 16–16	142.26	142.26
16H-2, 81–82	142.91	142.92
16H-4, 114–114	146.24	146.24
17H-3, 4–5	153.14	153.15
17H-3, 112–113	154.22	154.23
17H-6, 70–70	158.30	158.30
17H-7, 31–32	159.41	159.42
18H-4, 110–110	164.97	164.97
18H-6, 137–138	168.27	168.28
18H-7, 33–33	168.72	168.72
18H-CC, 5–6	169.28	169.29

Table T3. Diatom species, Site U1357. (See table notes.)

Sea ice–associated species
Actinocyclus actinochilus
Chaetoceros resting spores
Fragilariopsis curta
Fragilariopsis cylindrus
Fragilariopsis obliquecostata
Fragilariopsis rhombica
Fragilariopsis ritscheri
Fragilariopsis separanda
Fragilariopsis sublinearis
Porosira glacialis
Porosira pseudodenticula
Stellarima microtrias
Thalassiosira antarctica
Thalassiosira tumida
Cool open-ocean species
Rhizosolenia antennata var. *antennata*
Rhizosolenia antennata var. *semispina*
Thalassiosira gracilis
Trichotoxon reinboldii
Pelagic open-ocean species
Fragilariopsis kerguelensis
Thalassiosira lentiginosa
Thalassiosira oliverana
Thalassiothrix antarctica

Notes: Sea ice–associated species of Armand et al. (2005). Cool and pelagic open-ocean species of Crosta et al. (2005).

Table T4. Characteristic diatom species in select light–dark lamination couplets. (See table notes.) (Continued on next page.)

Light laminae					Dark laminae				
Core, section, interval (cm)	Depth (mbsf)	Abundance/ Preservation	Characteristic assemblage	Color	Core, section, interval (cm)	Depth (mbsf)	Abundance/ Preservation	Characteristic assemblage	Color
318-U1357A-					318-U1357A-				
1H-3, 50	3.50	A/G	***Chaetoceros dichaeta* (C)**, *Eucampia antarctica* resting form (terminal and intercalary) (F), ***Fragilariopsis curta* (A)**, ***F. kerguelensis* (A)**, ***F. rhombica* (C)**, ***Proboscia inermis* (C)**, ***Pseudonitzschia turgidula* (C)**, *Rhizosolenia antennata* var. *antennata* (R), ***R. antennata* var. *semispina* (C)**, ***R. simplex* (C)**		1H-3, 51	3.51	A/G	*Actinocyclus actinochilus* (F), *Asteromphalus* spp. (F), ***Chaetoceros* spp. resting spores (C)**, ***F. curta* (A)**, ***F. kerguelensis* (C)**, *F. obliquecostata* (F), ***F. rhombica* (C)**, *F. ritscheri* (F), ***F. sublinearis* (C)**, ***Shionodiscus gracilis* (C)**, *Thalassiosira antarctica* (F), *T. lentiginosa* (F)	
2H-4, 86	**12.97**	A/G	***C. dichaeta* (C)**, ***Chaetoceros* spp. RS (A)**, *E. antarctica* resting (intercalary) (F), ***F. curta* (A)**, *F. kerguelensis* (F), *F. obliquecostata* (F), ***F. rhombica* (A)**, *F. ritscheri* (F), *F. sublinearis* (F), *Proboscia alata* (F), *Proboscia inermis* (F), *R. antennata var. semispina* (F), *R. simplex* (F), ***Thalassiothrix antarctica* (C)**		2H-4, 82	12.93	A/M-G	***Chaetoceros criophilus* (C)**, *C. dichaeta* (F), ***Chaetoceros* spp. RS (C)**, *E. antarctica* resting (intercalary) (F), ***F. curta* (A)**, *F. kerguelensis* (F), *F. obliquecostata* (F), *F. rhombica* (F), *F. ritscheri* (F), *F. sublinearis* (F), P. *inermis* (F), *R. antennata* var. *semispina* (F), ***S. gracilis* (C)**, ***Thalassiothrix antarctica* (C)**	
3H-5, 148.5	24.60	A/G	***C. dichaeta* (C)**, ***Chaetoceros* spp. RS (C)**, *E. antarctica* resting (R), *E. antarctica* vegetative (R), ***F. curta* (A)**, *F. kerguelensis* (F), *F. obliquecostata* (F), ***F. rhombica* (A)**, *F. sublinearis* (F), *S. gracilis* (F), ***Thalassiothrix antarctica* (C)**		3H-5, 147.5	24.59	A/M-G	*A. actinochilus* (R), *C. dichaeta* (F), ***F. curta* (A)**, ***E. antarctica* resting (C)**, ***F. kerguelensis* (A)**, *F. obliquecostata* (F), *F. rhombica* (F), *F. ritscheri* (F), *F. sublinearis* (F), *T. lentiginosa* (F), *T. tumida* (F)	
5H-5, 82	42.42	A/G	***C. dichaeta* (A)**, ***Chaetoceros* spp. RS (A)**, ***F. curta* (A)**, ***F. kerguelensis* (C)**, *F. obliquecostata* (F), ***F. rhombica* (C)**, ***F. sublinearis* (C)**, *S. gracilis* (F), ***Thalassiothrix antarctica* (C)**		5H-5, 84	42.44	A/G	*A. actinochilus* (R), ***Chaetoceros* spp. RS (A)**, *E. antarctica* resting (F), ***F. curta* (A)**, ***F. kerguelensis* (C)**, ***F. obliquecostata* (C)**, ***F. rhombica* (C)**, ***F. ritscheri* (C)**, ***F. sublinearis* (C)**, *Porosira glacialis* (F), ***S. gracilis* (C)**, ***Thalassiosira antarctica* (C)**, *T. lentiginosa* (F), *T. tumida* (F)	
7H-1, 21	55.31	A/G	***E. antarctica* vegetative (A)**, ***F. curta* (C)**, *F. ritscheri* (F), *F. obliquecostata* (F), ***F. sublinearis* (A)**, *Porosira glacialis* (F), ***R. antennata* var. *semispina* (C)**		7H-1, 21.5	55.32	A/M	*E. antarctica* resting (F), ***F. curta* (C)**, ***F. kerguelensis* (C)**, *F. obliquecostata* (F), *F. ritscheri* (F), *F. rhombica* (F), *F. separanda* (F), ***F. sublinearis* (C)**, ***P. glacialis* (C)**, *S. gracilis* (F), ***Thalassiosira antarctica* (C)**, *T. lentiginosa* (F)	
9H-1, 68	74.78	A/G	*C. criophilus* (F), ***C. dichaeta* (C)**, ***Chaetoceros spp. RS* (C)**, ***F. curta* (A)**, ***F. kerguelensis* (A)**, ***F. obliquecostata* (C)**, ***F. ritscheri* (C)**, ***F. rhombica* (A)**, *F. sublinearis* (F), ***R. antennata* var. *semispina* (C)**, ***Thalassiosira antarctica* (C)**, *T. lentiginosa* (F), ***Thalassiothrix antarctica* (C)**		9H-1, 72	74.82	A/M–G	*Actinocyclus actinochilus* (F), ***Chaetoceros* spp. *RS* (A)**, *E. antarctica* resting (F), ***F. curta* (A)**, ***F. kerguelensis* (C)**, *F. obliquecostata* (F), *F. ritscheri* (F), ***F. rhombica* (A)**, *F. sublinearis* (F), *Odontella* spp. (X), ***R. antennata* var. *semispina* (C)**, ***S. gracilis* (C)**, ***Thalassiosira antarctica* (C)**, *T. lentiginosa* (F)	
13H-7, 21	119.96	A/G	*C. dichaeta* (F), ***F. curta* (A)**, ***F. kerguelensis* (A)**, ***F. rhombica* (A)**, ***S. gracilis* (C)**, ***Thalassiosira antarctica* (C)**		13H-7, 22	119.97	A/G	*Actinocyclus actinochilus* (F), ***Chaetoceros* spp. RS (A)**, ***F. curta* (A)**, ***F. kerguelensis* (C)**, *F. obliquecostata* (F), *F. ritscheri* (F), ***F. rhombica* (A)**, *F. sublinearis* (F), *Odontella* spp. (X), *Porosira glacialis* (R), *S. gracilis* (F), ***Thalassiosira antarctica* (C)**, ***T. lentiginosa* (C)**, *T. tumida* (F)	
14H-4, 50	126.34	A/M–G	*E. antarctica* resting (F), ***F. curta* (C)**, ***F. kerguelensis* (A)**, ***F. rhombica* (A)**, ***S. gracilis* (C)**, ***Thalassiosira antarctica* (C)**, *T. lentiginosa* (F), *T. oliverana* (F), *T. tumida* (F)		14H-4, 52	126.36	A/G	*C. criophilus* (F), ***Corethron pennatum* (A)**, ***F. kerguelensis* (C)**, *F. ritscheri* (F), ***R. antennata* var. *semispina* (C)**, *Trichotoxon reinboldii* (F)	Orange

Table T4 (continued).

Light laminae					Dark laminae				
Core, section, interval (cm)	Depth (mbsf)	Abundance/ Preservation	Characteristic assemblage	Color	Core, section, interval (cm)	Depth (mbsf)	Abundance/ Preservation	Characteristic assemblage	Color
15H-7, 67	138.65	A/G	***F. curta* (C)**, ***F. kerguelensis* (C)**, ***F. rhombica* (C)**, *F. vanhuerckii* (F), ***R. antennata* var. *semispina* (A)**, ***Thalassiosira antarctica* (C)**		15H-7, 71	138.69	A/G	***Chaetoceros* spp. RS (A)**, ***F. curta* (C)**, ***F. kerguelensis* (A)**, ***F. obliquecostata* (C)**, ***F. ritscheri* (C)**, ***F. rhombica* (C)**, ***Thalassiosira antarctica* (C)**, ***T. lentiginosa* (C)**	
16H-3, 59	144.19	A/G	***Chaetoceros* spp. RS (A+)**, ***F. kerguelensis* (C)**, ***P. glacialis* (C)**, *S. gracilis* (F), ***Thalassiosira antarctica* (C)**, ***T. lentiginosa* (C)**		16H-3, 61	144.21	A/G	*Azpetia tabularis* (R), ***Chaetoceros* spp. RS (A)**, *E. antarctica* resting (F), ***F. curta* (A)**, ***F. kerguelensis* (C)**, *F. obliquecostata* (F), *F. ritscheri* (F), *F. rhombica* (F), *F. sublinearis* (F), *Odontella* spp. (X), *P. glacialis* (F), *S. gracilis* (F), ***Thalassiosira antarctica* (C)**, *T. lentiginosa* (F)	
16H-6, 92	**149.02**	A/G	***Chaetoceros* spp. RS (A+)**, *E. antarctica* resting (terminal and intercalary) (F), *E. antarctica* vegetative (F), ***F. curta* (A)**, ***F. kerguelensis* (C)**, ***F. rhombica* (A)**, ***P. glacialis* (C)**, ***S. gracilis* (C)**, *Thalassiosira antarctica* (F), ***T. lentiginosa* (C)**, *Thalassiothrix antarctica* (F)		16H-6, 90	149.00	A/M–G	***Chaetoceros* spp. RS (A)**, *E. antarctica* resting (F), ***F. curta* (A)**, ***F. kerguelensis* (C)**, *F. obliquecostata* (F), ***F. rhombica* (C)**, *F. sublinearis* (F), *F. vanhuerckii* (R), *P. glacialis* (F), ***R. antennata* var. *semispina* (C)**, *R. simplex* (F), ***S. gracilis* (C)**, ***Thalassiosira antarctica* (C)**, *T. lentiginosa* (F)	
17H-7, 62	152.22	A/G	***Chaetoceros* spp. RS (A+)**, ***F. curta* (A)**, ***F. kerguelensis* (C)**, ***F. rhombica* (A)**, *F. ritscheri* (F), ***P. glacialis* (C)**, *R. antennata* var. *semispina* (F), ***S. gracilis* (C)**, *Thalassiosira antarctica* (F), ***T. lentiginosa* (C)**		17H-7, 64	152.24	A/M	***Chaetoceros* spp. RS (A)**, *E. antarctica* resting (F), ***F. curta* (A)**, ***F. kerguelensis* (C)**, ***F. obliquecostata* (C)**, *F. rhombica* (F), *F. ritscheri* (F), *F. sublinearis* (F), *F. vanhuerckii* (R), *Odontella* spp. (X), *R. antennata* var. *semispina* (F), ***S. gracilis* (C)**, ***Thalassiosira antarctica* (C)**, *T. lentiginosa* (F)	
18H-1, 111	**160.71**	A/G	*A. actinochilus* (F), *C. criophilus* (F), ***Chaetoceros* spp. RS (A+)**, ***C. pennatum* (C)**, ***F. curta* (C)**, ***F. kerguelensis* (A)**, ***F. rhombica* (C)**, *F. sublinearis* (F), *F. vanhuerckii* (R), ***R. antennata* var. *semispina* (C)**, *Thalassiosira antarctica* (F), *T. lentiginosa* (F), *Thalassiothrix antarctica* (F)		18H-1, 109	160.69	A/M	***Chaetoceros* spp. RS (A)**, ***F. curta* (A)**, ***F. kerguelensis* (A)**, ***F. obliquecostata* (C)**, ***F. rhombica* (C)**, *F. ritscheri* (F), *F. separanda* (F), *F. sublinearis* (F), *F. vanhuerckii* (R), *P. glacialis* (F), ***S. gracilis* (C)**, ***Thalassiosira antarctica* (C)**, ***T. lentiginosa* (C)**	
19H-2, 80	171.39	A/G	*F. curta* (F), ***F. kerguelensis* (C)**, *F. rhombica* (F), *T. lentiginosa* (F), ***Thalassiothrix antarctica* (A)**	White	19H-2, 80	171.39	A/M–G	*A. actinochilus* (F), ***Chaetoceros* spp. RS (A)**, *Coscinodiscus occulus-iridis* (F), ***F. curta* (C)**, ***F. kerguelensis* (C)**, ***F. rhombica* (C)**, *F. ritscheri* (F), *F. separanda* (R), *F. sublinearis* (F), *F. vanhuerckii* (R), ***P. glacialis* (C)**, *S. gracilis* (F), *Stellarima microtrias* (F), *Thalassiosira antarctica* (F), *T. lentiginosa* (F)	Olive

Notes: Abundance: A+ = very abundant (≥100 specimens/field of view), A = abundant, C = common, F = few, R = rare, X = trace. Preservation: G = good, M = medium, P = poor. Bold depths = paired samples in which the light lamination is stratigraphically lower than the dark lamination. Green text = open-ocean affinity (Crosta et al., 2005), blue text = sea ice affinity (Armand et al., 2005), bold text = present at common or greater abundances.

Table T5. Paleomagnetic age model, Hole U1357A. (See table note.)

Tie point	Core, section, interval (cm)	Depth (mbsf)	Age (ka)
	318-U1357A-		
1	2H-4, 80	12.91	950
2	3H-3, 65	20.76	1200
3	5H-3, 85	39.97	1880
4	8H-7, 130	72.81	3000
5	10H-5, 75	87.87	3300
6	11H-3, 140	97.50	3600
7	13H-6, 70	118.95	4800
8	15H-6, 95	137.43	5800

Note: Ages based on correlation to CALS7k.2 (Korte and Constable, 2005).

Table T6. Major and trace element concentrations, Site U1357. (See table notes.)

Core, section, interval (cm)	Depth (mbsf)	Major element oxide (wt%)									Trace element (ppm)				
		SiO_2	TiO_2	Al_2O_3	Fe_2O_3	MgO	CaO	Na_2O	K_2O	P_2O_5	Ba	Sr	V	Sc	Co
318-U1357A-															
1H-2, 57–58	2.07	67.00	0.08	1.36	0.00	5.93	2.46	23.19	1.16	0.17	166	150	11	3	7
1H-4, 50–51	5.00	76.29	0.22	4.26	0.59	3.14	1.84	12.19	1.29	0.17	313	116	23	4	5
1H-5, 142–143	7.42	78.58	0.16	2.63	0.27	2.93	1.94	12.24	1.11	0.13	197	108	16	3	5
2H-2, 30–31	9.40	78.77	0.18	3.34	0.34	2.73	2.29	10.94	1.22	0.17	200	115	17	3	5
2H-4, 83–84	12.94	81.36	0.22	4.58	0.24	2.38	1.70	8.00	1.34	0.16	283	105	26	5	9
3H-4, 23–25	21.84	84.23	0.10	1.40	0.00	2.23	1.55	9.71	0.85	0.14	182	97	12	3	5
3H-5, 29–30	23.40	84.10	0.20	4.01	0.11	2.01	1.24	6.96	1.22	0.13	302	86	25	5	7
3H-5, 31–32	23.42	83.81	0.16	3.07	0.21	2.07	1.25	8.24	1.05	0.14	267	91	21	3	5
3H-7, 66–67	26.79	84.41	0.21	4.34	0.34	1.88	1.10	6.26	1.29	0.13	327	87	27	5	7
4H-6, 9.5–10.5	34.20	85.21	0.10	1.32	0.00	2.13	1.35	9.20	0.83	0.12	182	83	13	2	4
4H-6, 11.5–12.5	34.22	83.56	0.27	5.56	0.64	1.78	1.39	5.13	1.51	0.14	392	100	34	5	9
6H-6, 8–9	52.70	85.81	0.11	1.81	0.00	1.92	1.14	8.19	0.91	0.11	214	80	16	3	5
7H-5, 72–73	61.17	85.06	0.20	4.10	0.91	1.62	1.13	5.62	1.23	0.11	302	82	30	4	5
8H-5, 10–11	68.89	89.55	0.07	0.83	0.00	1.47	0.96	6.68	0.67	0.10	127	62	11	2	4
8H-5, 11–12	68.90	89.64	0.08	1.14	0.00	1.41	0.96	6.26	0.72	0.10	131	60	15	2	4
9H-1, 80–81	74.90	88.02	0.13	2.29	0.17	1.43	1.23	5.75	0.88	0.10	198	73	18	3	4
10H-3, 22–23	85.22	89.32	0.12	2.11	0.00	1.31	0.81	5.40	0.85	0.11	222	59	16	3	5
11H-3, 52–53	96.62	87.83	0.15	3.22	0.29	1.35	1.06	4.96	1.00	0.13	232	76	21	3	5
12H-1, 20–21	102.80	88.15	0.14	2.70	0.18	1.40	1.04	5.33	0.93	0.13	200	70	21	3	4
12H-3, 20–21	105.75	89.72	0.12	2.38	0.00	1.35	0.90	4.74	0.89	0.12	200	64	17	3	8
13H-4, 17–18	115.97	88.13	0.17	3.29	0.33	1.34	0.93	4.66	1.02	0.11	313	71	23	3	4
13H-6, 99–100	119.24	90.24	0.08	1.31	0.00	1.47	0.61	5.91	0.77	0.07	188	47	12	3	7
13H-6, 101–102	119.26	88.28	0.17	3.32	0.35	1.33	0.92	4.48	1.02	0.11	296	69	22	3	5
14H-3, 10–11	124.66	90.76	0.08	1.34	0.00	1.33	0.95	5.23	0.69	0.09	158	56	13	3	8
14H-4, 52–53	126.36	81.88	0.08	1.09	0.00	1.67	7.42	5.87	0.68	1.54	586	283	25	2	5
15H-3, 89–90	134.10	88.05	0.17	3.85	0.08	1.37	0.96	4.24	1.14	0.11	383	80	24	5	8
15H-3, 91–92	134.12	90.25	0.09	1.42	0.00	1.30	0.82	5.44	0.72	0.10	256	59	14	2	4
15H-7, 68–69	138.66	90.39	0.07	1.40	0.00	1.48	1.06	5.53	0.68	0.09	169	64	13	3	7
15H-7, 69–70	138.67	87.45	0.17	3.56	0.35	1.40	1.24	4.70	0.97	0.14	269	83	22	4	5
16H-3, 41–42	144.01	90.12	0.10	2.18	0.00	1.30	1.35	4.55	0.77	0.11	195	77	16	4	7
17H-2, 61–62	152.21	90.11	0.10	1.41	0.00	1.37	0.95	5.49	0.65	0.09	162	60	14	2	4
17H-2, 63–64	152.23	87.24	0.19	4.02	0.39	1.43	1.17	4.35	1.07	0.12	279	81	25	4	8
19H-1, 62.5–63.5	169.72	87.26	0.17	3.19	0.39	1.36	2.20	4.42	0.91	0.10	226	112	24	3	5
19H-5, 34–35	175.43	89.71	0.11	2.09	0.00	1.34	1.25	4.86	0.78	0.07	170	72	18	3	7
19H-4, 20–21	176.79	80.82	0.25	6.75	2.18	1.81	3.14	3.28	1.57	0.14	397	145	32	4	7
19H-6, 44–45	177.03	77.65	0.29	8.94	2.62	1.96	3.78	2.77	1.77	0.14	476	199	41	7	14
20H-3, 76–77	182.36	85.51	0.24	6.34	0.60	1.19	1.56	2.82	1.61	0.07	332	99	24	6	9
20H-3, 100–101	182.60	87.13	0.19	3.94	0.53	1.12	2.93	2.94	1.08	0.12	261	119	24	4	5
20H-4, 100.5–101.5	184.10	94.03	0.06	1.24	0.00	0.80	0.66	3.41	0.60	0.03	135	38	12	3	7
20H-4, 103.5–104.5	184.14	89.76	0.11	2.06	0.01	0.92	3.01	3.29	0.74	0.09	206	98	15	3	5
21X-CC, 7–9	185.67	62.43	0.46	9.90	4.05	7.71	10.82	2.32	1.99	0.20	685	400	47	7	12

Notes: Major element oxides normalized to 100 wt%. Typical errors are 1%–5% for all elements over the course of two ICP-AES runs during which the samples were analyzed. Errors on the topmost 10 samples will be larger than this because of significant weighing errors during rough seas.

Table T7. Chemical composition of interstitial waters, Hole U1357C. (See table notes.)

Core, section, interval (cm)	Depth (mbsf)	pH	Salinity	Cl (mM)	Na (mM)	SO_4^{2-} (mM)	NH_4^+ (μM)	Alkalinity (mM)	DIC (mM)	PO_4^{3-} (μM)	Mg (mM)	Ca (mM)	K (mM)	Si (μM)	P (μM)	Sr (μM)	Ba (μM)	B (μM)
318-U1357C-																		
1H-1, 10–20	0.10	7.63	34.0	543.6	458.3	5.2	954.0	50.0	39.8	334.7	53.0	10.5	10.6	393.5	415.6	21.6	18.8	327.9
1H-1, 30–40	0.30	7.89	34.5	553.9	470.6	3.5	1038.9	55.5	45.4	424.3	54.7	10.9	10.6	445.5	220.9	24.0	7.7	244.2
1H-1, 50–60	0.50	7.78	35.0	550.5	466.9	2.3	920.1	58.4	48.3	451.7	54.4	10.8	10.6	398.5	382.4	21.0	17.9	307.1
1H-1, 70–80	0.70	7.79	35.5	558.6	474.5	0.0	1008.0	62.0	50.2	461.5	55.1	11.0	11.1	461.3	254.3	26.0	13.3	284.5
1H-1, 90–100	0.90	7.76	35.0	546.9	466.3	0.0	1308.9	62.0	51.0	457.0	53.8	10.8	10.8	403.8	364.9	26.1	20.1	309.8
1H-2, 20–30	1.20	7.76	35.5	555.4	472.0	0.0	1151.5	63.2	52.8	444.1	55.0	10.9	9.7	458.4	266.7	26.2	20.6	288.1
1H-2, 40–50	1.40	7.75	35.5	553.1	469.3	0.0	1058.9	61.4	51.4	374.9	54.7	10.9	10.8	477.9	268.3	27.3	21.7	295.1
1H-2, 60–70	1.60	7.73	35.5	552.3	469.1	0.0	998.8	64.3	52.6	362.0	54.7	10.9	10.9	452.5	271.1	25.7	23.0	287.6
1H-2, 80–90	1.80	7.72	35.5	554.9	471.3	1.8	1035.8	62.5	51.9	414.4	55.0	10.9	11.1	459.7	270.9	27.4	23.2	293.0
1H-3, 0–10	2.00	7.68	34.5	550.0	466.9	1.0	1830.3	65.5	215.9	485.8	53.7	10.7	10.8	398.6	401.6	21.0	18.9	313.4
1H-3, 20–30	2.20	7.7	36.0	553.9	470.7	1.5	989.5	62.7	52.4	434.2	54.9	11.0	11.0	460.1	273.4	26.9	23.1	294.9
1H-3, 40–50	2.40	7.73	36.0	551.1	469.0	0.8	1220.9	65.3	54.1	408.4	54.8	10.9	11.1	461.6	280.7	27.0	24.2	298.0
1H-3, 60–70	2.60	7.7	35.5	543.4	461.5	0.0	1552.6	67.7	55.4	402.3	53.9	10.7	11.0	445.1	280.0	26.1	24.4	296.4
1H-3, 80–90	2.80	7.78	35.5	551.5	471.0	0.0	1503.3	65.7	51.7	500.3	54.9	10.9	11.5	392.9	380.4	23.9	20.3	310.3
1H-4, 0–10	3.00	NA	36.0	552.4	470.2	0.0	1324.3	67.5	56.1	318.0	55.0	11.0	11.3	441.3	282.5	24.8	24.6	293.5
1H-4, 20–30	3.20	7.72	35.5	551.4	468.9	0.0	1478.6	69.6	56.5	327.1	54.8	10.9	11.2	442.1	281.3	25.0	24.9	296.1
1H-4, 50–60	3.50	7.76	36.0	547.9	467.6	0.0	1412.2	70.6	57.7	554.2	54.6	10.9	11.2	458.5	290.4	25.3	25.5	302.1
1H-4, 70–80	3.70	7.75	36.0	550.7	469.8	0.0	1361.3	71.1	58.5	312.6	55.0	10.9	9.9	445.2	288.4	25.7	25.6	299.4
1H-4, 90–100	3.90	7.72	36.0	548.9	469.9	0.0	1295.0	71.0	59.3	329.3	55.0	11.0	11.5	445.5	293.0	25.2	25.6	300.8
1H-5, 20–30	4.20	NA	NA	545.0	465.5	0.0	NA	0.0	60.1	NA	53.6	10.8	11.3	NA	NA	NA	NA	NA
1H-5, 50–60	4.50	7.73	36.0	543.8	464.7	0.0	1521.8	71.5	60.2	345.3	54.5	10.9	11.3	444.8	293.8	25.1	25.3	304.0
1H-5, 80–90	4.80	7.72	36.0	543.4	464.2	0.0	1708.5	73.7	58.8	346.1	53.9	10.9	11.3	451.4	303.5	26.2	25.7	311.3
1H-6, 10–20	5.10	NA	34.0	540.8	460.9	0.0	2614.1	NA	62.8	562.6	53.6	10.7	11.2	NA	NA	NA	NA	NA
1H-6, 40–50	5.40	7.74	36.0	545.7	466.8	0.0	1748.6	74.0	61.1	329.3	54.9	10.9	11.2	431.1	294.3	23.6	24.3	299.5
1H-6, 70–80	5.70	7.78	36.0	NA	NA	0.0	1816.5	73.7	62.4	355.9	NA	NA	NA	447.8	310.1	25.4	25.0	313.7
1H-7, 20–30	6.20	7.79	35.5	538.5	458.4	0.0	1777.9	75.9	60.9	380.2	53.6	10.8	11.0	432.5	316.2	23.3	23.4	289.9
1H-7, 70–80	6.70	7.78	36.0	546.3	465.9	0.0	1629.8	73.7	64.0	376.5	54.8	11.0	11.8	429.0	311.3	23.5	23.9	303.7
1H-8, 20–30	7.20	7.78	35.5	549.0	467.5	0.0	2331.8	75.6	64.6	400.0	54.8	11.1	11.4	413.6	303.3	24.0	23.6	287.7
1H-8, 80–90	7.70	7.75	36.0	544.0	466.0	0.0	2075.7	75.3	64.8	378.0	55.1	11.0	11.5	448.3	343.9	26.5	25.1	328.8
1H-8, 120–130	8.20	7.7	36.0	559.6	479.3	0.0	2478.3	76.9	63.4	608.2	56.2	11.3	11.7	506.2	297.1	24.3	24.0	289.5
2H-1, 10–20	8.90	7.69	36.0	547.6	473.5	0.0	2100.3	76.6	67.4	294.4	56.3	11.3	11.8	431.6	378.2	24.3	21.5	328.1
2H-1, 60–70	9.40	7.82	36.0	551.6	473.4	1.2	2739.1	75.6	64.6	384.0	55.5	11.3	11.8	465.0	277.2	27.1	24.5	287.5
2H-1, 110–120	9.90	7.65	36.0	543.8	467.9	2.9	1199.3	70.5	64.8	422.8	55.7	11.1	11.4	417.8	357.6	24.9	19.2	326.1
2H-2, 10–20	10.40	7.7	36.0	559.1	479.2	1.7	2905.7	73.6	65.5	340.0	56.6	11.5	12.0	465.8	266.9	27.0	16.7	272.5
2H-2, 110–220	11.40	7.68	36.0	554.1	475.2	1.5	2850.1	76.7	66.1	355.2	56.2	11.4	11.6	391.1	414.8	22.9	18.9	326.2
2H-3, 60–70	12.40	7.65	36.0	550.2	475.2	0.0	3663.2	83.1	69.7	414.4	56.4	11.5	12.0	403.0	423.2	21.4	19.8	326.7
2H-4, 10–20	13.40	7.66	36.0	553.0	474.9	0.0	3825.2	83.4	67.3	294.4	56.4	11.5	12.2	450.0	307.4	26.8	25.9	300.9
2H-4, 100–110	14.30	7.01	36.0	552.2	475.1	0.0	3485.8	85.0	69.7	286.0	56.5	11.5	12.2	454.2	244.7	25.7	10.8	260.5
2H-5, 60–70	15.40	7.61	36.0	554.5	475.7	0.0	4161.5	86.9	76.6	406.8	56.0	11.6	12.3	432.7	273.4	27.3	23.3	278.0
2H-6, 10–20	16.40	7.67	36.0	550.9	474.1	0.0	4130.7	86.4	74.4	360.5	55.9	11.3	12.2	404.5	424.3	22.5	19.7	326.6
2H-6, 101.5–111.5	17.32	7.68	36.0	548.8	473.2	0.0	3559.8	87.6	77.6	335.4	56.4	11.5	12.3	408.1	402.9	23.4	18.6	334.2
2H-7, 56–66	18.22	7.59	36.0	550.5	472.6	0.0	4527.2	88.1	79.6	308.1	55.8	11.5	12.2	388.6	394.2	23.2	19.3	315.1
3H-1, 112–122	19.42	7.53	36.0	550.7	473.4	1.1	1987.7	83.2	76.0	519.3	56.6	11.6	12.2	386.4	368.9	24.7	19.2	311.7
3H-2, 73–78	20.25	7.55	36.5	NA	469.5	1.5	3593.8	87.2	75.3	586.9	55.7	11.5	12.2	463.1	249.9	32.8	7.8	298.0

Notes: DIC = dissolved inorganic carbon. Gray shaded areas = levels in the core with elevated SO_4^{2-} concentrations. NA = not analyzed.

Appendix

Diatom floral list

Actinocyclus actinochilus (Ehrenberg) Simonsen
Actinocyclus curvatulus Janisch, in Schmidt et al.
Asteromphalus hyalinus Ehrenberg
Asteromphlus parvulus Karsten
Azpetia tabularis (Grunow) Fryxell et Sims, in Fryxell et al.
Chaetoceros bulbosus (Ehrenberg) Heiden, in Heiden and Kolbe
Chaetoceros criophilus Castracane
Chaetoceros dichaeta Ehrenberg
Chaetoceros spp.
Cocconeis costata Gregory
Cocconeis spp.
Corethron pennatum (Grunow) Ostenfeld
Coscinodiscus oculus-iridus Ehrenberg
Coscinodiscus spp.
Dactyliosolen antarcticus Castracane
Eucampia antarctica (Castracane) Mangin
Fragilariopsis curta (Van Heurck) Hustedt
Fragilariopsis cylindrus (Grunow) Krieger
Fragilariopsis kerguelensis (O'Meara) Hustedt
Fragilariopsis obliquecostata (Van Heurck) Hasle
Fragilariopsis rhombica (O'Meara) Hustedt
Fragilariopsis ritscheri Hustedt
Fragilariopsis separanda Hustedt
Fragilariopsis sublinearis (Van Heurck) Heiden
Fragilariopsis vanheurckii (Peragallo) Hustedt
Navicula spp.
Nitzschia spp.
Odontella litigiosa (Van Heurck) Hoban
Odontella weissflogii (Janisch) Grunow
Porosira glacialis (Grunow) Jörgensen
Porosira pseudodenticulata (Hustedt) Jousé, in Kozlova
Proboscia alata (Brightwell) Sundström
Proboscia inermis (Castracane) Jordan et Ligowski, in Jordan et al.
Pseudonitzschia turgidula Hustedt
Rhizosolenia antennata f. *antennata* Sundström
Rhizosolenia antennata f. *semispina* Sundström
Rhizosolenia simplex Karsten
Shionodiscus gracilis var. *expectus* (Van Landingham) Alverson, Kang et Theriot
Shionodiscus gracilis var. *gracilis* (Karsten) Alverson, Kang et Theriot
Stellarima microtrias (Ehrenberg) Hasle et P.A. Sims
Stellarima stellaris (Roper) Hasle et Sims
Thalassiosira antarctica Comber
Thalassiosira lentiginosa (Janisch) Fryxell
Thalassiosira oliverana (O'Meara) Sournia
Thalassiosira tumida (Janisch) Hasle in Hasle et al.
Thalassiothrix antarctica Schimper ex Karsten
Trichotoxon reinboldii (Van Heurck) Reid et Round